ABSTRACT

Title of Dissertation: TOWARDS FINE SCALE CHARACTERIZATION OF GLOBAL URBAN EXTENT, CHANGE AND STRUCTURE

Panshi Wang, Doctor of Philosophy, 2017

Dissertation directed by: Professor Chengquan Huang, Department of Geographical Sciences

Urbanization is a global phenomenon with far-reaching environmental impacts. Monitoring, understanding, and modeling its trends and impacts require accurate, spatially detailed and updatable information on urban extent, change, and structure. In this dissertation, new methods have been developed to map urban extent, sub-pixel impervious surface change (ISC), and vertical structure at national to global scales. First, an innovative multi-level object-based texture classification approach was adopted to overcome spectral confusion between urban and nonurban land cover types. It was designed to be robust and computationally affordable. This method was applied to the 2010 Global Land Survey Landsat data archive to produce a global urban extent map. An initial assessment of this product yielded over 90% overall accuracy and good agreement with other global urban products for the European continent. Second, for sub-pixel ISC mapping, the uncertainty caused by seasonal and phenological variations

is one of the greatest challenges. To solve this issue, I developed an iterative training and prediction (ITP) approach and used it to map the ISC of entire India between 2000 and 2010. At 95% confidence, the total ISC for India between 2000 and 2010 was estimated to be 2274.62±7.84 km^2. Finally, using an object-based feature extraction approach and the synergy of Landsat and freely available elevation datasets, I produced 30m building height and volume maps for England, which for the first time characterized urban vertical structure at the scale of a country. Overall, the height RMSE was only ±1.61 m for average building height at 30m resolution. And the building volume RMSE was ±1142.3 m^3. In summary, based on innovative data processing and information extraction methods, this dissertation seeks to fill in the knowledge gaps in urban science by advancing the fine scale characterization of global urban extent, change, and structure. The methods developed in this dissertation have great potentials for automated monitoring of global urbanization and have broad implications for assessing the environmental impact, disaster vulnerability, and long-term sustainability of urbanization.

TOWARDS FINE SCALE CHARACTERIZATION OF GLOBAL URBAN EXTENT, CHANGE AND STRUCTURE

By

Panshi Wang

Dissertation submitted to the Faculty of the Graduate School of the
University of Maryland, College Park, in partial fulfillment
of the requirements for the degree of
Doctor of Philosophy
2017

Advisory Committee:
Professor Shunlin Liang, Chair
Research Professor Chengquan Huang, co-chair
Associate Professor Giovanni Baiocchi
Dr. Eric C. Brown de Colstoun
Professor Gerrit Knaap, Dean's Representative

Dedication

Soli Deo Gloria

Acknowledgements

First, I would like to express my deep gratitude to my advisor Dr. Chengquan Huang for his guidance throughout my study. As the proverb says, "*Iron sharpens iron, and one man sharpens another*". Indeed, Dr. Huang has always been encouraging and helped me to achieve what I could not have imagined. Even at this moment, I still benefit from the advice he gave me when I first met him: "It's time to get your hands dirty". He is not only an excellent mentor, but also a great example to learn from. His deep knowledge and dedication to academic excellence have inspired me to keep working hard and digging deep.

I thank my co-adviser Dr. Shunlin Liang for his support and helpful suggestions when facing problems while developing this research. Special thanks go to Dr. Eric Brown de Colstoun, for his leadership as the principle investigator of the Global Man-made Impervious Surface (GMIS) project and his continuing support. I also wish to thank other members of my advisory committee Dr. Giovanni Baiocchi and Dr. Gerrit Knaap for providing their insights and valuable time to improve my research.

I was privileged to have the opportunity to work with many distinguished colleagues through the GMIS project: Dr. James Tilton, Dr. Bin Tan, Jacquiline Phillips, Sarah Niemczura and Dr. Pui-Yu Ling. I have learned enormously from each of them. Many thanks go to other friends and colleagues at Department of Geographical Sciences: Feng (Robin) Zhao, Rui Zhang, Min Feng, Feng (Aron) Zhao, Xiaopeng Song, Wenli Huang, Ben DeVries, Qing Ying, Dong Chen, Cheng Fu, and Lei Wang.

This dissertation was funded by NASA's Land Use and Land Cover Change program (NNX11AH67G) and the Dr. Jingli Yang Geographical Sciences Research Fellowship.

Last but not least, I would like to thank my family. Thank you for always being there for me, mom and dad. Thank you to my wife Wenlu for unconditional love, understanding, and support. Thank you to my son Enoch for bringing so much joy to the family.

Table of Contents

List of Tables

List of Figures

Chapter 1: Introduction

1.1 Background

Earth has become an urban planet (Wigginton et al. 2016), which is manifested by the following facts. More than half of the world's population now dwells in urban areas and the urban population is expected to reach two thirds of the world's population by 2050 (United Nations 2015). For the last three decades of the 20th century, the rate of urban land expansion has been even higher than the rate of urban population growth, a trend that is expected to continue in the future and projected to contribute additional 1,527,000 km^2 of urban land cover globally (an area roughly equal to the size of Mongolia) by 2030 (Seto et al. 2011). Far beyond the physical boundary of urban areas, urbanization impacts the Earth's environment profoundly. The ecological footprint of a city could be as large as 200 times the area of a city itself, as demands on food, energy, and materials grow as urban areas expand (Wigginton et al. 2016). The environmental pressure induced by these demands is also amplified by agricultural land loss due to urban expansion and teleconnections enabled by global trade networks (DeFries et al. 2010; Jiang et al. 2013; Pandey and Seto 2015; Satterthwaite et al. 2010; Seto and Ramankutty 2016). The reach of the environmental impact of urbanization is broadened through not only land-based or demand-driven teleconnections, but also pollutant pathways. Because global economic activities are concentrated within urban areas, ~70% of global greenhouse gas emissions could be attributed to urban areas (Seto et al. 2014). Urban areas are also major sources of air and water pollution (Brabec et al. 2002;

Duncan et al. 2016; Fichot et al. 2016; Lamsal et al. 2013). Finally, the modification of local to regional environment by urbanization, such as the urban heat island effect and increased stream flashiness, may also lead to consequences at larger spatial scales (Bounoua et al. 2015; Imhoff et al. 2010; McDonald et al. 2014; McGrane 2016). In summary, in the era of an urban planet, urbanization has become a planet-scale phenomenon with global environmental impacts.

The sheer scale and speed of urbanization present grand challenges to humanity. Facing global climate change, environmental change, and natural disasters, urban areas are particularly vulnerable (Cutter and Finch 2008; Mosquera-Machado and Dilley 2008; Tessler et al. 2015). The development of essential infrastructure and services (e.g., water supply, transportation, and waste management) may lag greatly behind the growth of urban population and urban land (Cotton and Franceys 1994; Larsen et al. 2016; McDonald et al. 2014; Zeug and Eckert 2010). Such lag is often more severe in developing countries and may disproportionately affect low-income population groups, leading to inequality and public health risks (Njoh 2016; Tatem and Hay 2004; Unger and Riley 2007). In addition, urbanization is often accompanied by economic, social, and cultural changes, threatening the stability of economic and societal structures (Chen et al. 2014; Cohen 2004), challenging established governance models and institutions (Pierre 1999; Stren 2009; United Nations 2011), and raising issues of stress and anxiety among urban inhabitants (Lederbogen et al. 2011). Among all the challenges, the biggest is probably the rising demand of water, food and energy, questioning if urbanization is a sustainable path of development (Bogardi et al. 2012; Cohen 1995; Cohen and Garrett 2009; Foley et al. 2005).

However, many people argue that urbanization also brings great opportunities towards solving pressing environmental and societal issues. Approximately 60% of the urban area estimated for 2050 will be newly built, particularly in developing countries (Ramaswami et al. 2016). With energy-efficient urban designs, urban areas have great potential for energy savings and emission reduction, especially in developing areas where the urban form and structure are still being shaped (Cheshmehzangi and Butters 2016; Creutzig et al. 2015; Kammen and Sunter 2016). With respect to sustainability in general, two arguments suggest possible scenarios of environment-friendly urbanization. The first argument follows the logic of the "environmental Kuznets curve hypothesis" (Grossman and Krueger 1991), linking the gain of economic efficiency through compact urban growth with environmental efficiency (Li and Ma 2014; Williams et al. 1996). The second one focuses on the concentration of human capital and thus innovation in urban areas, highlighting the importance of new technologies and ideas in achieving sustainable urbanization (Seto and Ramankutty 2016).

The environmental impacts of urban expansion, challenges and opportunities associated with urbanization have been central themes of urban studies and debate topics. In response to many open questions associated these topics, there has been a boom in urban studies since the 1990s (Wang et al. 2012). However, huge knowledge gaps still exist and continue to hinder our understanding of urbanization, particularly at continental to global scales. Several fundamental aspects of urbanization remain to be better characterized: (1) How to define the term "urban" and its spatial extent? (2) How fast do urban areas grow and how are these growths spatially distributed? (3) How to measure the form and structure of urban areas, particularly in the vertical dimension?

Addressing these issues are not only fundamental to understanding urbanization and its impacts, but also crucial to establishing scientific grounds for developing polices and strategies to meet the challenges of urbanization.

First, an accurate urban extent map is one of the prerequisites of further study on urbanization. Urban extent map from various data sources has been widely used to define urban-rural boundary for urban studies such as the environmental impacts of urbanization and socioeconomic drivers of urban development. (Bechle et al. 2015; Patino and Duque 2013; Samuel et al. 2016; Xu et al. 2016). Urban extent information is also an important input for modeling the response of the climatic system to urbanization (Bounoua et al. 2015). To model the spatiotemporal dynamics of urban expansion, historical urban extent is critical for model calibration (Jantz et al. 2004; Liu and Seto 2008; Seto et al. 2012). Also, compared to other information sources such as administrative boundaries, urban extent maps provide a basis to define urban population and urban economic activities consistently across spatial scales (Brockerhoff 1999; Cohen 2004; Hsieh 2014). Global urban extent maps has been produced using coarse- and moderate-resolution remote sensing data (Arino et al. 2007; Bartholomé and Belward 2005; Imhoff et al. 1997; Loveland and Belward 1997; Schneider et al. 2009). However, huge uncertainties exist in the global urban land area estimates given by these maps (**Table 1-1**). One way to improve global urban extent maps is using finer resolution satellite (e.g., Landsat) to map urban extent. Yet great technical challenges still exist for finer resolution urban extent mapping, including the amount of data processing needed and data quality issues such as insufficient spectral resolution, confusions between spectrally similar land cover types, and spectral variations (Gong et

al. 2013; Herold et al. 2003a; Herold et al. 2004), although 30 m data products have been recently made available (Chen et al. 2015b; Klotz et al. 2016).

Table 1-1: A partial list of percent urban land area estimations from existing global urban products.

Name of dataset	% of urban land in global land area	Time	Data Source	Resolution	Reference
GRUMP	2.38	1995	DMSP/ OLS	1km	(CIESIN (Center for International Earth Science Information Network) 2011)
Global Urban Extent in 2000	0.50	2000	DMSP/ OLS	1km	(Zhou et al. 2015)
MOD500	0.45	Circa 2001-2002	MODIS	500m	(Schneider et al. 2009; Schneider et al. 2010)
Global Impervious Surface	0.43	Circa 2000-2001	42.3%	1km	(Elvidge et al. 2007)

Second, the fast rate of global urbanization makes it necessary to map urban change and to update the global urban maps regularly. However, to map urban change effectively, very high resolution (VHR) data is often required (Jensen and Cowen 1999), particularly in low- to medium-density areas, where the majority of urban changes happen. For global scale urban change mapping, because of limitations in data availability, the best representation of urban area is a subpixel continuous field variable, commonly referred as impervious surface cover (Sexton et al. 2013b; Song et al. 2016). With impervious surface cover mapping techniques, it has been demonstrated that Landsat data could be used to construct a spatially and temporal detailed record of urban change (Xian and Homer 2010; Yang et al. 2003). However, because existing

impervious surface change mapping techniques are sensitive to spectral variations, great uncertainties many exist in the change derived from year-to-year difference (Li and Wu 2014; Walton 2008; Yuan et al. 2008). Although effective methods based on time series have been developed to address this issue (Sexton et al. 2013b; Song et al. 2016), impervious surface change estimation from bi-temporal images remains a technical challenge when time series data is not available.

Finally, three-dimensional (3D) structural information has been missing in global urban data products. Structural information, including building height and volume, are greatly needed for key applications such as disaster vulnerability assessment (Geiß et al. 2016), climate change adaption (Seto and Christensen 2013), and population distribution mapping (Lu et al. 2011; Qiu et al. 2010). Technologies such as light detection and ranging (Lidar) have enabled the mapping of urban structures at unprecedented levels of detail (Gonzalez-Aguilera et al. 2013; Zheng and Weng 2015). However, for most areas of the world, the vertical structures of urban landscape are yet to be mapped in most areas of the world due to data constraints.

For all the three urban attributes, data availability has been a major factor limiting the use remote sensing datasets. Recent development of Earth observation capabilities has brought the richness of remote sensing data to an unprecedented level. Global Land Survey (GLS) dataset, a series of global orthorectified cloud-free Landsat image archive at multiple epochs, greatly reduces the difficulty of global urban mapping (REF HERE). The first global 30 m impervious surface fraction product is being produced by the global man-made impervious surface (GMIS) project (PIs: Drs. Brown de Colstoun and Huang) using this dataset. Moreover, space-borne

interferometric synthetic aperture radar (InSAR) and orthophotography technologies have been used to produce global wall-to-wall observations of land surface heights. Global 30 m digital surface model (DSM) datasets have been made available, including the Shuttle Radar Topography Mission (SRTM), Advanced Spaceborne Thermal Emission and Reflection Radiometer (ASTER) Global Digital Elevation Model (GDEM), and Advanced Land Observing Satellite (ALOS) World 3D–30 m (AW3D30) datasets (Rodriguez et al. 2006; Tachikawa et al. 2011; Tadono et al. 2016; Van Zyl 2001). Finally, nightlights data has been made available from the Defense Meteorological Satellite Program (DMSP) satellites and the Visible Infrared Imaging Radiometer Suite (VIIRS) onboard the Suomi NPP satellite (Elvidge et al. 2017; Imhoff et al. 1997). Therefore, there is a timely opportunity to bring together multiple remote sensing datasets for better characterization of global urban land cover, change, and structure.

1.2 Research Objectives

One clear vision guided the development of the research objectives of this dissertation: advancing urban remote sensing to address the challenges of urbanization. As identified in the previous section, urban extent, change, and structure are three key areas where remote sensing information is urgently needed and where great knowledge gaps exist. Although greatly limited by data availability and quality, the characterization of these urban attributes at global scale may be greatly advanced based on innovative information extraction and machine learning techniques. The following research objectives were formulated as concrete steps towards achieving this vision:

1. Design and implement a method for global urban extent mapping using Landsat data.
2. Investigate effective methodology for mapping sub-pixel urban impervious surface change using bi-temporal Landsat imagery at global scale.
3. Establish and prototype a method for characterizing large-scale vertical structure of urban areas using free datasets.

As discussed in the review of the state-of-the-art methods for characterizing these urban attributes, there are many technical challenges to achieve each objective. Among these challenges, these three are highlighted and posed as the main research questions:

1. How to develop robust feature variables for mapping global urban extent consistently using Landsat datasets containing spectral and phenological inconsistency?
2. How to minimize biases and errors in impervious surface change estimated from bi-temporal Landsat imagery acquired during different seasons?
3. How to extract height information from global DSMs for building height and volume estimation?

1.3 Dissertation Outline

This dissertation is organized into five chapters. The following three chapters are the primary chapters, which address the research objectives listed above. These three chapters are self-contained and structured in the format of journal articles. A

review of literature relevant to each chapter is provided in the introduction section in each chapter. A flowchart of the research objective organization into the primary chapters of this dissertation is shown in **Figure 1-1**. As shown in the diagram, the following three chapters are closely related because (1) they aim to successively characterize urban areas in the two-dimensional, temporal, and vertical domains; (2) they all use Landsat data and are linked to the GMIS project; and (3) the urban extent maps from Chapter 2 are used in Chapters 3 and 4.

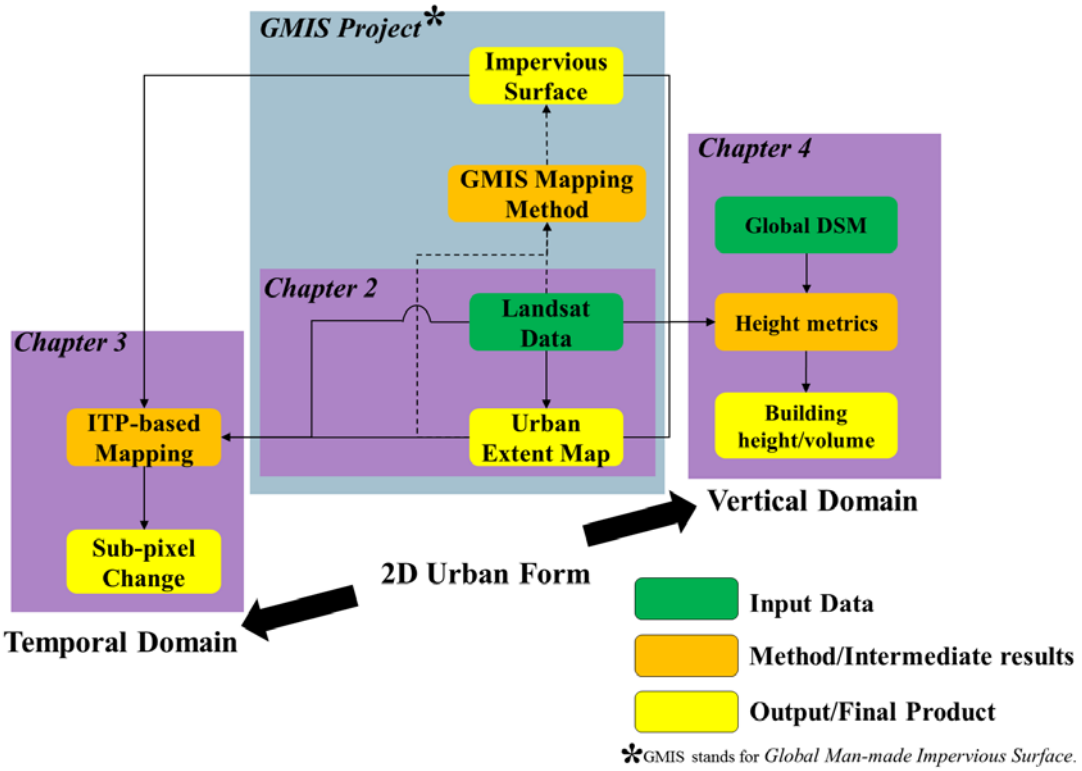

Figure 1-1: A schematic illustration of the overall structure of this dissertation.

Chapter 2 presents a method for the mapping of the global urban extent using the Global Land Survey Landsat dataset. An innovative hierarchical object-based texture (HOTex) classification approach was designed to overcome spectral confusion between urban and nonurban land cover types and to address the issue of inconsistent

phenology among global Landsat images. A new definition of urban extent was also developed to achieve a balance between the purely "physical" and "human" perspective of urban land. The method was successfully used globally to produce an urban extent map, which is integral to the GMIS project and is used as an urban mask (**Figure 1-1**). Initial assessments of the method and comparisons with other global urban datasets will be performed for the European continent. Moving to the temporal domain, Chapter 3 investigates sub-pixel impervious surface change mapping with bi-temporal Landsat data, which may be subject to seasonal and phenological variations. To this end, an iterative training and prediction (ITP) approach was developed to reduce the bias of impervious surface change caused by these variations. The method was applied to map the impervious surface change in India between 2000 and 2010. To characterize the urban vertical structure, Chapter 4 establishes an approach for mapping building height and volume using multiple datasets. Building height/volume mapping is estimated from global digital surface model (DSM) datasets by leveraging impervious surface and segmentation derived from Landsat data. Note that although the methods developed in all three chapters are intended for global applications, Chapter 2 focuses on Europe, while Chapters 3 and 4 focus on country-level case studies due to time constraints. India was chosen as the study area of Chapter 3 because of its fast rate of urbanization (Pandey et al. 2013). On the other hand, England, a country with relatively slow urban change, was chosen for Chapter 4 to minimize temporal discrepancy issues caused by different acquisition dates of the available datasets. The findings and contributions of these chapters are summarized in Chapter 5 together with discussions of their implications.

Chapter 2: Mapping Human Built-up and Settlement Extent (HBASE) at Global Scale Using Landsat-based Hierarchical Segmentation and Texture Information

2.1 Introduction

Urban land cover only accounts for a small percentage of the Earth's land surface (estimates range from 0.2% ~ 3% (Liu et al. 2014; Schneider et al. 2009; Small 2004)), whereas more than half of the world's population now dwells in urban areas. Urban population is continuing to grow rapidly and is expected to reach two thirds of the world's population by 2050 (United Nations 2015). This ongoing global urbanization process has broad impacts on the Earth's environmental systems including climatic systems (Arnfield 2003; Seto and Shepherd 2009), hydrologic systems (Arnold and Gibbons 1996), and ecosystems (Foley et al. 2005; Kaye et al. 2006). Such impacts can go far beyond the physical footprint of urban areas (Lambin et al. 2001). Understanding the drivers, impacts, and feedbacks of urban growth requires detailed and up-to-date information on the spatial extent of urban areas (Wentz et al. 2014).

Conventional data sources used for urban extent mapping include vector data and census population data based on administrative boundaries (Potere and Schneider 2007). As valuable as these data sources are, they are too coarse for many applications and can become outdated quickly due to long updating cycles. The rapid development of Earth observation technologies in recent decades made it possible to mitigate these problems. Global datasets acquired by coarse- to moderate-resolution satellites, such as the Defense Meteorological Satellite Program Operational Linescan System

(DMSP-OLS) (Imhoff et al. 1997; Zhou et al. 2015), Moderate Resolution Imaging Spectroradiometer (MODIS) (Schneider et al. 2009), Satellite Pour l'Observation de la Terre Vegetation (SPOT VEGETATION) (Bartholomé and Belward 2005) and Medium Resolution Imaging Spectrometer (MERIS) (Arino et al. 2007), have been used to map urban extent at the global scale (Potere et al. 2009). However, many urban features are much smaller than the large pixel sizes of these datasets and hence cannot be mapped reliably using these datasets (Jensen and Cowen 1999; Weng 2012). Ideally, meter or sub-meter resolution images should be used in order to map the fine scale urban features accurately (Small and Sousa 2016; Weng 2012), but such high-resolution images have yet to be acquired for many land areas worldwide. Landsat-class satellites provide a viable option that balances the need for global coverage and spatial detail for urban monitoring.

Since the launch of the first Landsat in 1972, the series of Landsat satellites have created and will continue to create global datasets with the level of spatial details (i.e., sub-hectare spatial resolutions) needed to reveal the unique textures of typical urban areas and to delineate the boundaries of most built-up areas (Patino and Duque 2013). Global Landsat datasets known as the Global Landsat Survey (GLS) have already been assembled using historical acquisitions (Gutman et al. 2008; Gutman et al. 2013; Tucker et al. 2004). Based on the global acquisition strategies that have been implemented since the launch of Landsat 7 (Arvidson et al. 2006; Irons et al. 2012), global coverage of Landsat data has been and will continue to be generated annually or sub-annually from 2000 onward.

Urban areas are among the most heterogeneous landscapes and thus are inherently difficult to map from remote-sensed observations. Most urban pixels are mixtures of buildings, pavements, trees, lawn/grass, and/or other nonpaved surfaces. Even pixels with a single type of surface cover often have spectral signatures similar to the same cover type in nonurban areas. For example, urban trees likely have nearly identical spectral values as trees in nonurban areas and therefore can be confused with each other when classified using spectral data. One solution for this problem is to use spatial image features such as edge density or local statistics (Gong and Howarth 1990; Herold et al. 2003b). Other spatial features useful for urban mapping include texture measures derived from the gray level co-occurrence matrix (GLCM) (Haralick et al. 1973; Shaban and Dikshit 2001), wavelets (Myint et al. 2004), fractal (Myint 2003), and spatial autocorrelation (Myint and Lam 2005). Improved urban mapping may also be achieved by using multi-temporal or dense time series of spectral data (Schneider 2012; Sexton et al. 2013b). Due to lack of a well-designed global acquisition strategy prior to 2000, however, it is difficult to obtain multiple cloud free Landsat observations during any given epoch before 2000 for all urban areas globally.

Another challenge in Landsat-based large-area urban mapping is the lack of a consistent vegetation phenology. Although images acquired during the peak growing season were preferred in developing the GLS dataset, more than 10% of the images of the GLS dataset were not acquired during the peak growing season (Gutman et al. 2013; Townshend et al. 2012). Similarly, a large number of images used to produce a global 30 m land cover classification were acquired in the winter months (Gong et al. 2013). These leaf-off images may yield low classification accuracies due to the low spectral

separability between deciduous vegetation and non-vegetated surfaces. Furthermore, the classification of adjacent images with different vegetation phenology using spectral-based methods can result in large discontinuities among those images. To mitigate these problems, composite algorithms are being developed for the creation of more consistent global datasets using Landsat or Landsat-class images (Hansen et al. 2013; Hermosilla et al. 2015; Roy et al. 2010). However, the usefulness of those composited images for urban mapping has yet to be assessed.

The main purpose of this study is to develop an approach suitable for continental- to global-scale mapping of the human built-up and settlement extent (HBASE) using existing global Landsat datasets, namely, the GLS images (Gutman et al. 2008; Gutman et al. 2013). Here, the term "HBASE" is introduced to avoid ambiguities and implied limitations of the term "urban" and some other commonly used terms. By definition, "urban" is the opposite of rural and therefore may imply the exclusion of villages and other built-up and settlement areas outside urban perimeters. Other terms such as "built-up" or "impervious surface" may imply the exclusion of non-built-up or non-impervious surfaces such as lawns, gardens, and other green spaces around houses, buildings, and pavements, which should be considered within the extent of human settlements. While the term "settlement" may be subject to different interpretations, to some it may imply the exclusion of roads and other built-up areas not developed for residential purposes. By considering both "built-up" and "settlement", HBASE includes all types of human built-up surfaces and the surrounding areas that were developed along with those surfaces to support their functionality. In an urban area, HBASE is similar to the urban extent class of the Global

Rural–Urban Mapping Project (GRUMP) dataset (CIESIN (Center for International Earth Science Information Network) 2011). It also includes most of the urban related classes as defined in the Urban Atlas (UA) (see **Table 2-1** and subsection 2.3.2.2 for more details), a European Union-wide dataset providing high-resolution land use maps for functional urban areas (FUAs) (European Environment Agency (EEA) 2016; Seifert 2009), and extends these classes beyond the traditional urban or city limit.

The HBASE mapping method is based on the observation that many HBASE areas have distinctive textural patterns. It uses texture measures derived from Landsat spectral bands instead of applying spectral data as direct input of a classification model to map urban areas. To overcome some of the limitations of traditional window-based texture calculation methods (Chen et al. 2004; Gong 1994; Guindon and Zhang 2009; Hodgson 1998), the following improvements were made: (1) generate image segments at multiple levels using the RHSeg hierarchical segmentation algorithm (Tilton 2007; Tilton et al. 2012b), (2) calculate textures using image objects instead of local windows, (3) use textures calculated at multiple object levels to represent texture information at different scales, and (4) include cross-band (color) textures in addition to single-band (grayscale) textures to better separate HBASE and non-HBASE areas. Furthermore, nightlight data from the Visible Infrared Imaging Radiometer Suite (VIIRS) Day/Night Band (DNB) were used to improve urban detection and vegetation phenology information from an annual MODIS vegetation index (VI) dataset was used to account for phenology differences among the Landsat images. Below, I first describe this hierarchical object-based texture (HOTex) method and its use to produce a circa-2010, global 30 m HBASE product using GLS 2010 data. Subsequently, the comprehensive

assessment of the mapping method and derived product over the European continent is presented, followed by discussions and a summary of the conclusions.

2.2 Methods

The HBASE mapping algorithm follows a typical supervised classification approach driven by training data. Given the many challenges with urban mapping using spectral-based methods that were discussed earlier and the fact that many urban areas have unique textures, the algorithm uses hierarchical textures instead of spectral data for the classification. This HOTex method consists of the following major components: derivation of hierarchical image segments, texture calculation, high-level feature extraction, training and classification, and post-classification processing (**Figure 2-1**). In this study, GLS 2010 images obtained over Europe were used to derive image segments and texture measures. Nightlight data obtained from the VIIRS DNB band and a MODIS VI dataset were used to derive high-level features to improve the classification performance. A road network dataset was used for post-classification processing to improve the representation of major roads in the derived HBASE product. I evaluated the mapping approach with different sets of input features. The feature set that yielded the best results was used to produce the final European-wide HBASE dataset, which was evaluated against several urban datasets existing for Europe following assessments through cross-validation and using an independent reference dataset. Finally, the method for mapping HBASE in Europe was applied to the entire GLS 2010 dataset to produce a global HBASE product.

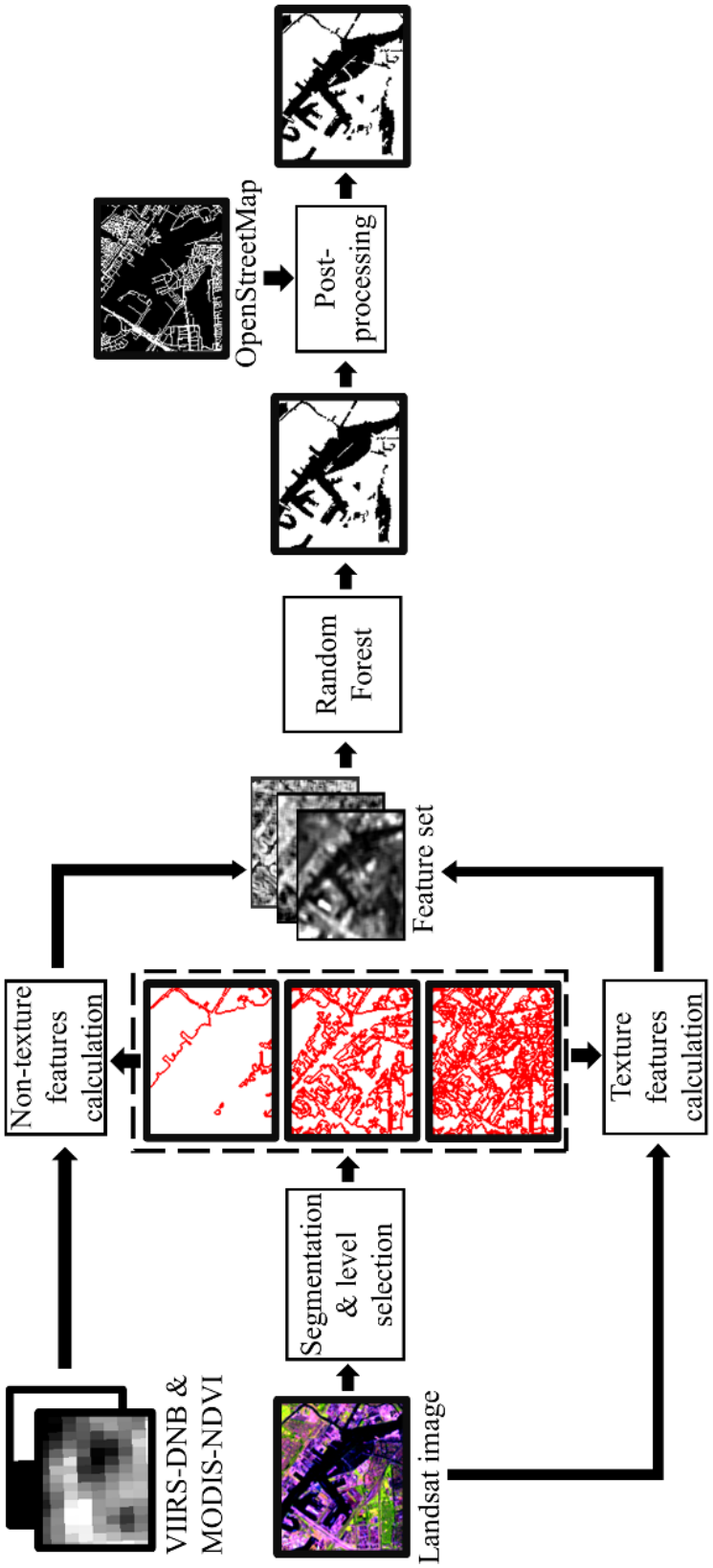

Figure 2-1: Overall workflow of the HBASE mapping methodology.

2.2.1 Derivation of Image Objects

2.2.1.1 GLS Data and Preprocessing

The GLS dataset was developed through a joint NASA–USGS collaboration to provide a convenient basis for developing global land cover and change products (Gutman et al. 2008; Gutman et al. 2013). The goal was to provide one cloud-free image acquired during the peak growing season per epoch per location, although suboptimal images were also used when a qualified image was not available (Gutman et al. 2013; Townshend et al. 2012). The GLS 2010 dataset used in this study consisted of ~53% Landsat 5 TM images, 42% gap-filled Landsat 7 ETM+ images, and 5% Earth Observer 1 (EO-1) Advanced Land Imaging (ALI) images (Gutman et al. 2013). Only the TM and gap-filled ETM+ images of Europe were used in this study because the ALI images were used to cover small islands only. The TM and ETM+ images have been atmospherically corrected and converted to surface reflectance (SR) using the Landsat Ecosystem Disturbance Adaptive Processing System (LEDAPS; (Masek et al. 2006) of the Global Land Cover Facility (GLCF). Global assessments revealed that the LEDAPS SR values were highly consistent with MODIS SR (Feng et al. 2012; Feng et al. 2013).

2.2.1.2 Image Segmentation

The GLS SR images were segmented using the Recursive Hierarchical Image Segmentation (RHSeg) software package (Tilton et al. 2012b), a recursive approximation of the Hierarchical Image Segmentation (HSeg) package. The HSeg combines the power of the best merge region growing to delineate the boundaries between spatially adjacent regions and spectral clustering to group spatially disjoint regions together. However, the computational cost is very high for Landsat-level

(~8000 by 8000 pixels) or larger images. Using a divide-and-conquer approach, RHSeg was designed to improve the speed of the HSeg algorithm on cluster- or cloud-computing systems, which greatly reduced the computing time in this study. The output of the RHSeg algorithm includes image objects at multiple levels, where finer-level objects are nested within coarser-level objects.

2.2.1.3 Object Level Selection

Depending on the image complexity, the processing of the Landsat images by RHSeg typically resulted in 20–80 levels. Although one could use textures calculated at all object levels, this would result in varying numbers of texture variables. In addition, textures calculated at adjacent levels might be highly correlated, leading to redundant features and high computing costs. Based on heuristic analyses of the RHSeg results, I used texture metrics calculated from objects at three representative levels for the classification. The objects at these three levels were determined by three levels of the maximum object size: 2,500 pixels (2.25 km^2), 250,000 pixels (225 km^2), and 25,000,000 pixels (22,500 km^2), which represent HBASE and non-HBASE features at local, intermediate, and macroscales, respectively. Following the hierarchical segmentation structure, a bottom-up merging process was applied: starting from the finest level, finer scale RHSeg objects were merged to coarser scale until the maximum object size at each level was reached. **Figure 2-2** provides a demonstration of how this bottom-up merging procedure works at level 1 using 2,500 as object size threshold. For example, fine level objects A and B were merged into object H. The merging stopped at object H because the higher-level object L exceeded the size threshold. Moreover,

the merging process followed the segmentation hierarchy (hence "bottom-up"). For example, object A was merged with B instead of E.

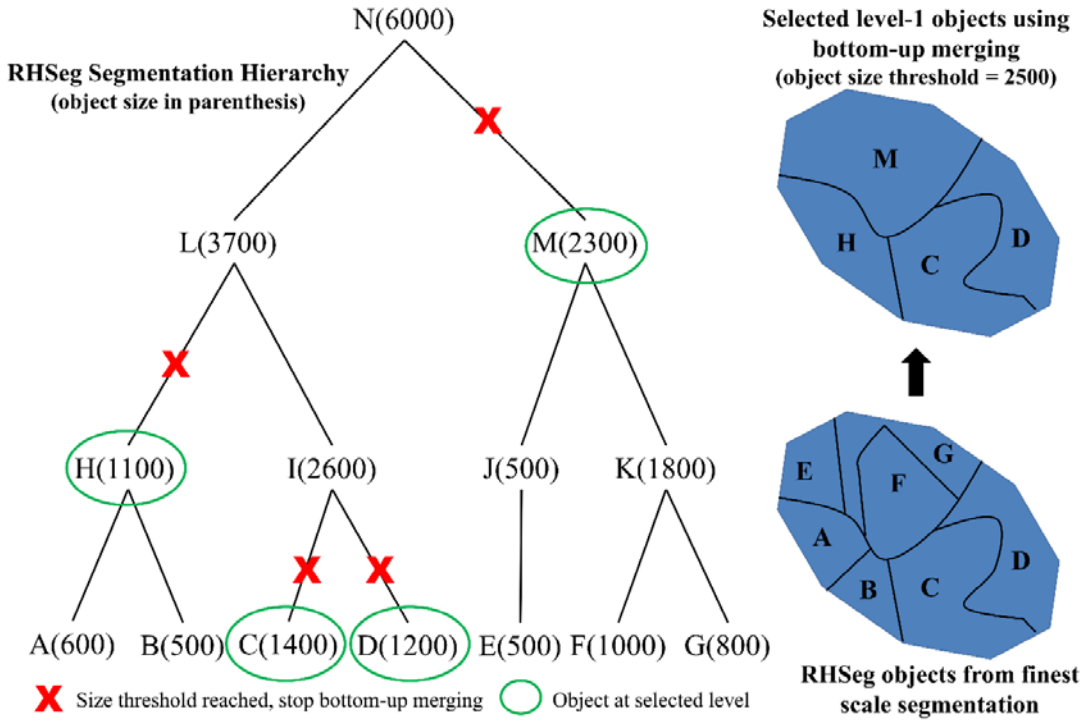

Figure 2-2: A conceptual diagram showing how finest-scale RHSeg objects are merged to create level-1 objects following the segmentation hierarchy using bottom-up merging: finer-scale RHSeg objects were merged to coarser scale until a threshold for objects size was reached.

2.2.2 Feature Extraction

2.2.2.1 Conventional GLCM Textures

For every object at each level, GLCM textures were calculated. Given an image I with G gray levels, an object O, and an offset vector $v = (\Delta x, \Delta y)$, the equation for calculating GLCM is:

$$GLCM(i, j, \Delta x, \Delta y) = \sum A(i, j, x, y, \Delta x, \Delta y), \qquad (2\text{-}1)$$

where

$$A(i, j, x, y, \Delta x, \Delta y) = \begin{cases} 1 & if \quad I(x, y) = i \,\&\, I(x + \Delta x, y + \Delta y) = j \\ 0 & elswhere \end{cases}. \quad (2\text{-}2)$$

GLCM was converted into a symmetrical matrix $P(i, j)$ described in (Haralick et al. 1973). Based on the resulting matrix $P(i, j)$, I calculated four of the Haralick texture features:

$$AngularSecondMoment = \sum_{i=0}^{G-1}\sum_{j=0}^{G-1} P^2(i, j), \quad (2\text{-}3)$$

$$Contrast = \sum_{i=0}^{G-1}\sum_{j=0}^{G-1} (i-j)^2 P(i, j), \quad (2\text{-}4)$$

$$Variance = \sum_{i=0}^{G-1}\sum_{j=0}^{G-1} (i-\mu)^2 P(i, j), \quad (2\text{-}5)$$

$$Correlation = \frac{1}{Variance}\sum_{i=0}^{G-1}\sum_{j=0}^{G-1} (i-\mu)(j-\mu)P(i, j), \quad (2\text{-}6)$$

where

$$\mu = \sum_{i=0}^{G-1}\sum_{j=0}^{G-1} iP(i, j), \quad (2\text{-}7)$$

and G is the number of grayscale levels. Based on preliminary tests of G values in published studies (Clausi 2002; Gong et al. 1992; Marceau et al. 1990), G was set to 32 in this study.

Another implementation issue to consider when calculating GLCM from Landsat bands is how to rescale the SR values into a limited number of grayscales without significant loss of information. Usually, this is done by setting the grayscale

value to $G-1$ when the band value is above a certain threshold and performing a linear stretch on the band values below the threshold:

$$SR_{scaled} = \begin{cases} (G-1) \times SR / threshold, & SR < threshold \\ G-1, & SR \geq threshold \end{cases}. \quad (2\text{-}8)$$

However, we found that no single threshold could preserve adequate image details across a large area. Therefore, when calculating textures, I used a set of high thresholds (0.8 for the SR of all bands used) to distinguish dark and bright areas and a set of low thresholds (band 5: 0.4, band 4: 0.5, band 3: 0.15) to focus on the details within the low- and medium-value range. This generated two sets of features that jointly provide a better representation of the textures.

2.2.2.2 Color Textures

The GLCM texture features were calculated for Landsat spectral bands 5 (mid-infrared), 4 (near-infrared), and 3 (red), a widely used band combination to distinguish urban land cover and other land cover types. Because traditional GLCM texture features only use one band for calculation, no spatial pattern of color appearance could be represented. In past studies, it has been tried to use a stacking approach to combine spectral features (e.g., band values, spectral indices, and spectral transforms) with texture features. However, because spectral values exhibit large within-class variation and between-class similarity, I argue that the introduction of spectral features provides little benefits to the goal of building a robust feature set for large-scale application. Studies on general purpose image classification also support that the joint use of color and texture features may actually lower the performance of the classifier (Mäenpää and Pietikäinen 2004). Therefore, I used a modified cross-band GLCM (Palm 2004) for

color texture representation. For a pair of spectral bands (m, n), the cross-band GLCM is calculated by:

$$GLCM^{m,n}(i, j, \Delta x, \Delta y) = \sum A^{m,n}(i, j, x, y, \Delta x, \Delta y), \tag{2-9}$$

where

$$A^{m,n}(i, j, x, y, \Delta x, \Delta y) = \begin{cases} 1 & if \quad I_m(x, y) = i \\ & I_n(x + \Delta x, y + \Delta y) = j, \\ 0 & elswhere \end{cases} \tag{2-10}$$

and I_m, I_n are the values of band m and n, respectively.

Color texture features were calculated by substituting the GLCM with the cross-band GLCM in Equations (1–7). Because I used a symmetrical GLCM, there were only three different combinations of spectral bands 5, 4, and 3, which are (5, 4), (4, 3), and (5, 3).

2.2.2.3 Non-texture Features

In addition to textures, three groups of variables were used to address some of the issues with the GLS dataset. The first was a flag indicating if an image was a Landsat 7 image. The Scan Line Corrector (SLC) of Landsat 7 failed in 2003, resulting in SLC-off images with ~22% data gaps (Roy et al. 2008). The gaps created artificial objects defined by gap boundaries; therefore, a flag was needed to separate Landsat 5 and 7 images.

The second variable group was designed to provide contextual information on local and regional vegetation phenology and other environmental conditions, which is similar to the ecoregion-based stratification idea described in Schneider et al. (2010).

Here, we used metrics derived from the MODIS-normalized difference vegetation index (NDVI) instead of ecoregions. Specifically, we used the MODIS 0.05 degree NDVI monthly composites (MOD13C2), a global cloud-free NDVI record derived from 16-day 1 km MODIS NDVI composites (MOD13A2; (Didan 2015), to calculate three values for each 0.05-degree MODIS pixel: annual maximum NDVI, annual median NDVI, and the NDVI value for the Landsat image acquisition date. The median value of these three layers was then calculated for every Landsat level-3 object and for the footprint of the entire Landsat image being analyzed. Considering the large pixel size of the MOD13C2 dataset, no aggregated NDVI value was derived for level-1 and level-2 objects.

The third variable group was designed to improve the separability between HBASE areas and some large non-HBASE areas such as large agriculture fields, deserts, and areas covered by snow/ice using nightlight data. Global nightlight data acquired by the DMSP-OLS and VIIRS/DNB have been provided by the Earth Observation Group (EOG) of the NOAA National Geophysical Data Center (NGDC) (Earth Observation Group 2016). At the time this study was conducted, a full−year DNB composite with gas flare detection was only available for 2015. To minimize the impact of lights unrelated to human built-up or settlement areas, including lights from auroras, air glow, gas flare, and fishing boats (Baugh et al. 2013), I first derived an annual median nightlight product from the 2015 DNB monthly composites and then applied a stable light mask to set the annual median product to 0 for areas in which the stable light was 0. The stable light product was derived based on 2010 DMSP-OLS data by the EOG. The use of the 2010 DMSP-based stable light product not only

provided an alternative approach for filtering DNB data in absence of a reliable VIIRS stable light product (Li et al. 2013) but also removed lights from new HBASE areas developed after the GLS 2010 acquisition time. Finally, I overlaid this hybrid VIIRS–DMSP stable light product on the Landsat-based segmentation results to calculate the minimum, average, and maximum DNB values for each of the objects at the three selected levels.

2.2.3 Classification and Product Generation

2.2.3.1 The Random Forest Classifier

The Random Forest (RF) machine learning algorithm has become one of the most widely used algorithms in remote sensing land cover studies. It uses random subsets of training data and explanatory variables to build an ensemble of decision trees, which reduces the generalization error due to overfitting (Breiman 2001). Its robust performance and capabilities to model nonlinear data and to handle the wide range of feature variables made it suitable for use in this study. Compared with other state-of-the-art algorithms (e.g., support vector machines, SVM), it also involves lower computational cost (Rodriguez-Galiano et al. 2012), which is particularly important for global-scale applications. Furthermore, another great advantage of RF is that it could generate an estimate the probabilities of a pixel belonging to different classes, which has been found to be a valuable information for mapping land cover change (Yin et al. 2014).

2.2.3.2 Training Data Collection

The required training data were delineated through visual interpretation of the Landsat images and high-resolution images available from Google Earth™ (GE). In addition to HBASE and non-HBASE samples, cloud/shadow samples were also selected because many GLS images had some level of cloud contamination. The training samples were selected based on the following rules: (1) an object was assigned as HBASE if it contained at least one HBASE pixel and no cloud/shadow pixels; (2) an object was assigned as non-HBASE if all pixels were non-HBASE pixels; (3) any object containing cloud/shadow pixels was assigned as cloud/shadow. This rule set was designed to produce an inclusive HBASE product that could capture low-density residential areas, which means the final product would be optimized to minimize the omission of HBASE areas. Note that this does not imply that the HBASE definition is intrinsically object-based. The training pixels were selected on a pixel-by-pixel basis and assessments including cross-validation were also conducted in a pixel-based manner. As a necessary step to provide training data for an object-based classification, converting per-pixel labels of HBASE/non-HBASE to object-based labels may introduce errors in the training data when the segmentation result is not accurate. However, these will be considered as mapping errors rather than natural outcome of the definition.

I adopted an iterative approach to derive training data. The initial set of training samples was selected to represent different urban types. This training dataset was then applied to train a RF model, which was used to produce an initial product. The derived product was then examined against the input Landsat images and high-resolution GE

images. Additional training samples were collected over areas with large classification errors. This was repeated until no large errors were detected; remaining errors were more likely due to the lack of separability than the lack of representative training samples. At the end, a total of 183,324 objects from 325 Landsat images distributed across Europe were collected as the final training dataset (**Figure 2-3**).

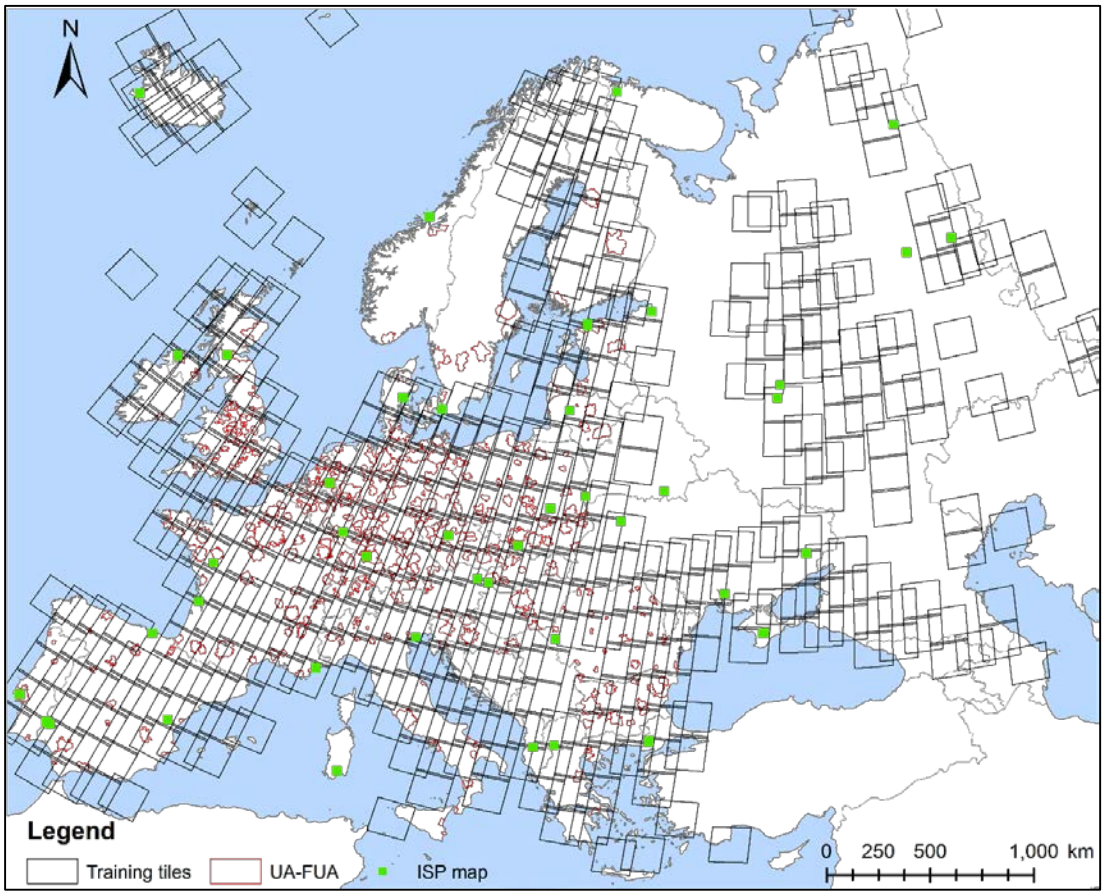

Figure 2-3: The distribution of Landsat tiles with training data, Urban Atlas functional urban areas (UA-FUA, (European Environment Agency (EEA) 2016)), and impervious surface percentage (ISP) maps used for product assessments.

2.2.3.3 Classification Experiments

Given the large number of features derived in Subsection 2.2.2 from different data sources, we conducted a series of experiments to determine the best feature set combination by progressively including more variables in the classification. First, only

the textures plus the Landsat 7 indicator variable were used. The MODIS NDVI-based feature set and nightlight-based feature set were then added, first separately and then together. Finally, these classification results were compared with a baseline classification experiment in which only the SR of six Landsat spectral bands and four widely used spectral indices were used as input variables. The four spectral indices were calculated as follows (Crist 1985; Kriegler et al. 1969) :

$$\begin{aligned} Brightness = {} & 0.2043\times\rho_1+0.4158\times\rho_2+0.5524\times\rho_3+ \\ & 0.5741\times\rho_4+0.3124\times\rho_5+0.2303\times\rho_7, \end{aligned} \tag{2-11}$$

$$\begin{aligned} Greeness = {} & -0.1603\times\rho_1-0.2819\times\rho_2-0.4934\times\rho_3+ \\ & 0.7940\times\rho_4-0.0002\times\rho_5-0.1446\times\rho_7, \end{aligned} \tag{2-12}$$

$$\begin{aligned} Wetness = {} & 0.0315\times\rho_1+0.2021\times\rho_2+0.3102\times\rho_3+ \\ & 0.1594\times\rho_4-0.6806\times\rho_5-0.6109\times\rho_7, \end{aligned} \tag{2-13}$$

$$NDVI = (\rho_4-\rho_3)/(\rho_4+\rho_3), \tag{2-14}$$

*w*here $\rho_1 \sim \rho_7$ are surface reflectance values of Landsat TM/ETM bands.

2.2.3.4 HBASE Product Generation and Post-processing

As will be shown in Subsection 2.3.1, the use of all feature variables derived in Section 2 yielded the best performance in terms of overall accuracy, user's and producer's accuracy, and kappa statistic. Therefore, the final HBASE classification was produced using all features. During the examination of the classification results, I noticed that most roads were not captured. To mitigate this omission error, I used the OpenStreetMap (OSM) to provide information on major roads. OSM is a publicly available dataset intended to provide up-to-date information on the global road network

by incorporating open government data and user-contributed data (OpenStreetMap contributors 2016). Knowing that some of the OSM users contributed datasets of local roads and their quality could be difficult to assess, only major roads (motorways and primary and trunk roads, according to the OSM nomenclature), secondary roads, and airport runways from the OSM were included. These roads were rasterized and added to the final HBASE classification generated by the RF classifier.

Global HBASE maps were produced by applying the HOTex approach to all 8,689 Landsat TM and ETM scenes in the GLS2010 archive. Following the approach described in Subsection 2.2.3.2, a total of 1,658,805 training objects were collected worldwide (**Table 2-1**), which were used to train a global random forest model. The global model input features the same as the ones used by the European model.

Table 2-1: The number of HBASE training objects by continent.

Continent	Number of Training Objects
Asian	583,592
Africa	509,412
Europe	183,324
North America	325,958
South America	44,574
Oceania	11,945
Total	1,658,805

2.2.4 Algorithm and Product Assessment

2.2.4.1 Scene Level Cross Validation

The classification experiments described in Subsection 2.2.3.3 were evaluated through scene-level cross-validation (SLCV) as follows. First, the 325 Landsat images over Europe from which training samples were selected were divided into ten random groups. For each feature set to be evaluated, training samples from nine of the ten scene groups were used together to train the RF algorithm, which was then evaluated using reference samples in the set-aside image group. This was repeated ten times such that each time samples from a different image group were used to evaluate the RF model derived using samples from the other nine image groups. The results from the ten assessments were pooled together to produce cross-validation accuracy estimates. The overall accuracy, kappa coefficient, and producer's and user's accuracies for the HBASE class were calculated using standard accuracy assessment equations (Congalton 1991; Stehman and Czaplewski 1998). Note that although the classification was done using an object-based method, the cross-validation was performed at the pixel level because the final HBASE product will be provided to users as a pixel-by-pixel map and the definition of HBASE does not intrinsically rely on object segmentation, as discussed in Subsection 2.2.3.2. When performed at the pixel level, the cross-validation may produce inflated accuracy estimates because spatially adjacent pixels could be divided into training and testing samples in each fold of cross-validation, resulting in spatial autocorrelations between some training and testing samples (Friedl et al. 1999). Because there is no overlap of training data of adjacent scenes, by splitting the training and testing samples by Landsat images, this SLCV method was designed

to eliminate spatial autocorrelations between training and testing samples in each fold of cross-validation and hence should produce reasonably unbiased accuracy estimates.

2.2.4.2 Independent Assessments

Two independent reference datasets were used to evaluate the final HBASE product. The first dataset consisted of 93 image windows with a size of ~ 6 by 6 km. Based on commercial high-resolution satellite imagery from the National Geospatial-Intelligence Agency (NGA)'s unclassified commercial satellite data archive, the image windows were made available to NASA under the NGA's NextView license agreement. These image windows were selected along the rural to urban center gradient of many cities distributed across Europe (**Figure 2-3**). These images were processed through a NASA-funded sister project to map Global Man-made Impervious Surfaces (GMIS) from Landsat (PIs: E. Brown de Colstoun and C. Huang). Typically used images have four spectral bands (blue, green, red, and near-infrared) and a spatial resolution between one to two meters. Within the queried images, visual assessment was made to identify a cloud-free image acquired around 2010. The selected image was orthorectified with the GLS images used in this study to achieve a satisfactory co-registration accuracy (i.e., < 30 m). It was then classified by an image analyst to create a highly reliable, high-resolution impervious surface map using computer-assisted image interpretation software, where impervious surfaces included buildings, pavements, and other manmade impervious surface materials (Tilton et al. 2012a). This map was overlaid on top of the 30 m grids of the GLS images to calculate the impervious surface percentage (ISP) at 30 m resolution. Imperviousness threshold values of 0%, 25%, 50%, and 75% were used to classify the 30 m pixels into four imperviousness classes. This dataset was

used to evaluate the HBASE product based on imperviousness, a key factor considered in defining urban areas in most studies (Potere and Schneider 2007).

The second dataset was the Urban Atlas (UA), a European Union-wide dataset providing high-resolution land use maps for functional urban areas [FUAs;(European Environment Agency (EEA) 2016; Seifert 2009). This dataset was produced by classifying high-resolution satellite imagery (e.g., 2.5 m SPOT 5) and integrating multiple ancillary datasets including a navigation database. It uses a hierarchical classification system to define FUAs (Seifert 2009). At the most detailed level, the classification system had 17 urban-related classes and 10 nonurban classes. The urban and nonurban classes had minimum mapping units of 0.25 and 1 ha, respectively. The preliminary accuracy assessment revealed that the classes had an overall accuracy of 99% and 91%, respectively (Copernicus Land Monitoring Services 2015).

At the time of this study, UA data were available for 2006 and 2012. The 2012 dataset was used in this study. It consisted of 437 FUAs distributed mostly in western and central Europe (**Figure 2-3**). To evaluate how different FUAs were represented by the derived HBASE product, we kept all 17 urban-related classes but aggregated the ten nonurban classes into four classes: agriculture, natural and semi-natural area, wetland, and water (see **Table 2-6** for a detailed list of urban and nonurban classes). For each class, we calculated the proportion classified as HBASE and non-HBASE in the derived HBASE product.

2.2.4.3 Comparison with Other Urban/settlement Data Products

Several existing data products provided information on the distribution of urban and human settlement areas in Europe around 2010 including: 1) GlobeLand30, a 30

m land cover map for 2010 (Chen et al. 2015b); 2) Global Urban Footprint (GUF), a 12 m urban footprint map for year 2012 from TanDEM-X (Esch et al. 2013; Esch et al. 2012); 3) Global Human Settlement Layer (GHSL), which includes a 38 m built-up layer based on Landsat (Pesaresi et al. 2013); 4) GlobCover, a 300 m land cover map for 2009 (Arino et al. 2007); 5) MODIS Collection 5.1 land cover product (MCD12Q1), a 500 m global land cover map for 2010 (Friedl et al. 2010); and 6) GRUMP, a 1 km (30 arcseconds) urban/rural map (CIESIN (Center for International Earth Science Information Network) 2011)]. A summary of these datasets is provided in **Table 2-2**. The derived HBASE product was compared with these products at five levels. First, spatial characteristics of the products with 30 m or higher resolution were examined through visual assessment at selected sites. Second, the independent imperviousness dataset was used to compare the HBASE and other urban datasets at different levels of urban density. Third, the UA dataset was used to evaluate HBASE/urban areas calculated from each dataset at the FUA level. Fourth, agreement matrices were used to calculate agreement metrics between the HBASE product and other datasets. Finally, country-level HBASE/urban area estimates were calculated using each product and the differences among those estimates were examined. Because the GlobCover, MODIS, and GRUMP datasets have a much lower resolution than the rest of the datasets, they were only used for comparison at the country level. Note that all these datasets have different degrees of differences with the HBASE product in terms of definition. For example, the MCD12Q1 and GlobCover products define urban as built-up land with >50% density, while the GRUMP dataset defines urban based on threshold of

nightlight. Disagreements introduced by these definition differences need to be carefully interpreted.

Table 2-2: List of datasets used for comparison with the HBASE product.

Name	Year	Spatial Extent	Resolution	Data Source	Definition of "urban"
GRUMP	2000	Global	30 arc-seconds	DMSP-OLS	A combination of areas with nightlight above a threshold and polygons with > 5000 population.
MCD12Q1	2010	Global	500 m	MODIS	Areas dominated by built environment (>50%), including non-vegetated, human-constructed elements, with minimum mapping unit > 1km.
GlobCover	2009	Global	300 m	MERIS	Artificial surfaces and associated areas (urban areas >50%).
GHSL	2013-2014	Global	38 m	Landsat	The area occupied by buildings and its surrounding.
GlobeLand 30	2010	Global	30 m	Landsat	Artificial surfaces mainly consist of urban areas, roads, rural cottages and mines, which are primarily based on asphalts, concrete, sand and stone, bricks, glasses, and other materials.
Urban Atlas	2012	EU-28	100 m (rural), 50 m (urban)	SPOT 5 /ALOS	17 urban land use classes
GUF	2011-2012	Global	12 m	TerraSAR-X/ TanDEM-X	Man-made structures with a vertical component, including all kind of buildings and constructions.

2.3 Results

2.3.1 Effectiveness of Input Features for HBASE Classification

The scene-level cross-validation (SLCV) accuracies revealed large differences among HBASE classifications derived using different input feature sets (**Table 2-3**). Because HBASE only accounted for a small portion of the total area, the overall accuracies differed by less than 5% among the different input feature sets. However, use of texture resulted in near 10% or more improvements in kappa as well as user's

and producer's accuracies than the spectral based classification. Adding MODIS NDVI based features resulted in further improvements in the user's accuracy and kappa, while the VIIRS DNB based features helped to improve the producer's accuracy and kappa. Combining both feature sets with the texture features led to improvements in both user's and producer's accuracies as well as further improvement in kappa (**Table 2-3**). The visual examination of HBASE products derived using different input feature sets revealed that initial texture-based classifications had noticeable commission or omission errors. Many of those errors were removed when additional feature sets derived based on MODIS NDVI and VIIRS DNB were used (**Figure 2-4**).

Table 2-3: Scene-level cross-validation (SLCV) scores of HBASE classifications using different input feature sets (OA: overall accuracy, UA: user's accuracy, PA: producer's accuracy).

	Number of Features	**Cross-validation Scores**			
		OA	**UA**	**PA**	**Kappa**
Spectral	9	94.0%	76.5%	78.1%	0.74
GLCM	145	96.8%	86.2%	89.9%	0.83
GLCM+VI	151	97.1%	91.1%	86.3%	0.87
GLCM+DNB	154	97.1%	86.6%	92.3%	0.88
GLCM+DNB+VI	160	**97.9%**	**91.4%**	**92.8%**	**0.91**

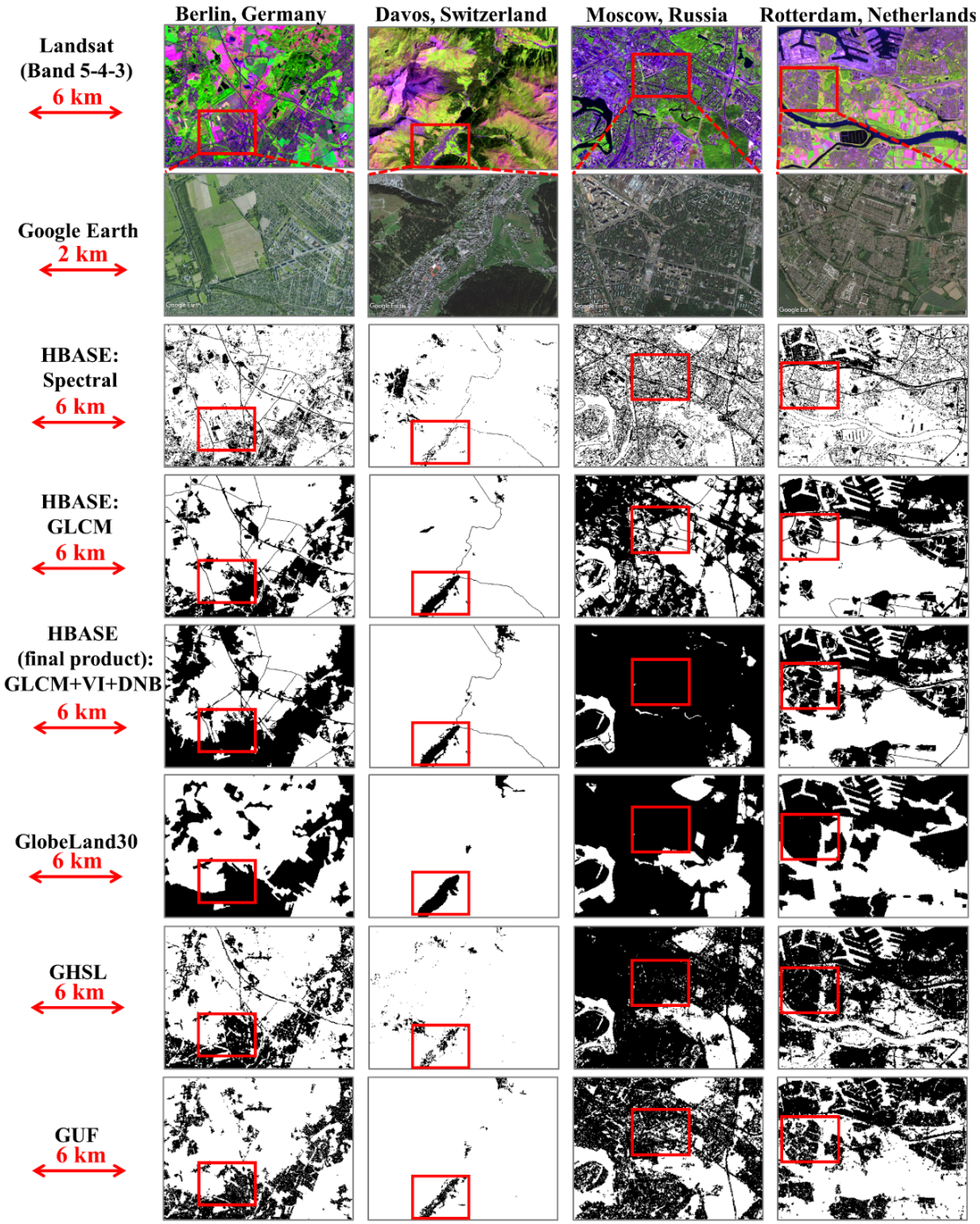

Figure 2-4: Comparison of HBASE products (derived using spectral features, texture features, and the combination of texture, MODIS NDVI, and DNB features) and other urban datasets including GlobeLand30, GHSL, and GUF (black: HBASE/urban, white: non-HBASE/nonurban). Google Earth™ images for the smaller window (shown as red boxes) are provided for each site to better show the details.

2.3.2 European HBASE Product Assessment

Because the use of MODIS NDVI and VIIRS DNB together with object-based textures yielded the best accuracies, the final HBASE product was produced using this feature group. This product was assessed in three ways including scene-level cross-validation (SLCV) and assessments based on imperviousness and functional areas. The SLCV accuracies were discussed in Section 2.3.1 (**Table 2-3**). The derived European HBASE product had a kappa coefficient value of 0.91 and overall, user's, and producer's accuracies over 90%. Because the SLCV was carefully designed to avoid spatial autocorrelations between training and testing samples during each fold cross-validation, these accuracy estimates were not necessarily overestimated, although they were not derived using a probability-based accuracy assessment method.

2.3.2.1 Imperviousness-based Assessment

Although HBASE was not defined based on specific imperviousness threshold values, the most important feature of an HBASE area is the presence of man-made impervious surfaces or proximity to such surfaces. A comparison of the HBASE product with the percent imperviousness reference data derived based on high-resolution satellite images revealed that ~95%, 90%, and 80% of the areas with percent imperviousness values in the ranges of > 75%, 51%–75%, and 26%–50% were classified as HBASE (**Table 2-4**). Pixels with percent imperviousness values between 1% and 25% were highly confused with non-HBASE pixels. Only slightly more than 50% were classified as HBASE. Approximately 10% of the pixels without impervious cover were classified as HBASE. These were not necessarily commission errors

according to the definition of HBASE because non-impervious surfaces such as lawns, gardens, and other urban green spaces should be included in the product.

When the HBASE product was evaluated against reference data derived using percent imperviousness as a sole criterion, its user's accuracy decreased, while the producer's accuracy increased as the imperviousness threshold value increased (**Figure 2-5**). A balance of ~75% was achieved when the imperviousness threshold was ~ 5%.

Table 2-4: Proportion of pixels classified as HBASE/urban/settlements by HBASE, GlobeLand30, GHSL, and GUF datasets for different imperviousness intervals.

Percent Imperviousness	Proportion classified as HBASE	Proportion classified as urban by GlobeLand30	Proportion classified as urban by GHSL	Proportion classified as urban by GUF
>75%	95.63%	92.18%	91.71%	79.23%
51%-75%	89.63%	87.42%	82.06%	75.48%
26%-50%	78.84%	77.82%	65.16%	62.32%
1%-25%	56.94%	56.97%	35.62%	34.54%
0%	9.87%	6.78	1.48%	1.48%

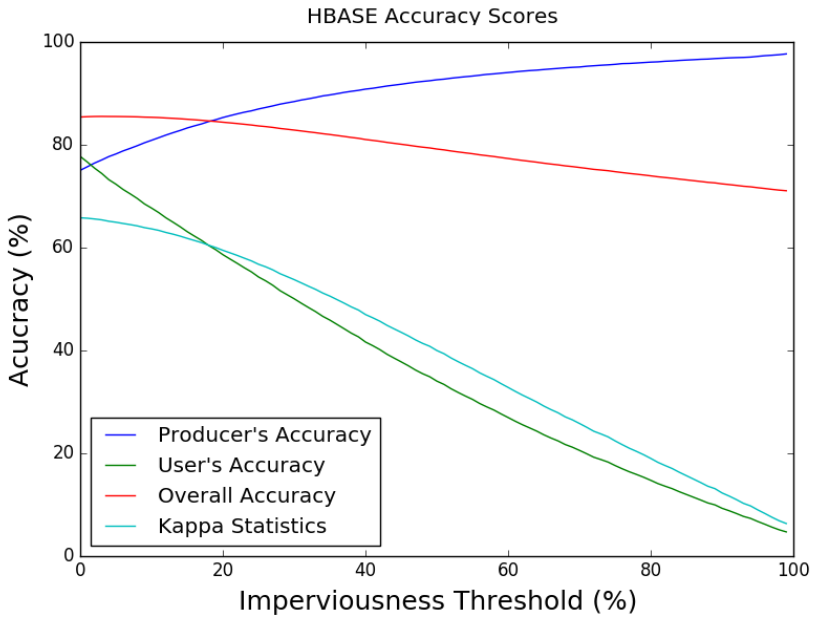

Figure 2-5: HBASE accuracy scores using different imperviousness thresholds.

2.3.2.2 Functional Urban Area-based Assessment

If HBASE was defined to include all functional urban classes and non-HBASE nonurban classes of the UA dataset (**Table 2-5**), the derived HBASE product showed an overall agreement of 89.7% with the UA dataset. Less than 3% of nonurban areas were classified as HBASE. However, only 51.5% of the pixels classified as urban by UA were classified as HBASE (49.3% if three classes not in the HBASE definition were excluded). This could be attributed to a number of factors. More than 95% of areas classified as isolated structures in UAs were not classified as HBASE. This class had a maximum size of 2 ha (~22 Landsat pixels), and hence might not be identified as a separate object, even at the finest object level. Although the segmentation approach allows the identification of objects as small as one Landsat pixel, isolated structures are likely to be merged with surrounding non-HBASE objects due to spectral mixing. Also, two transportation classes, including other roads and associated land and railways and associated land, had less than 50% of the areas classified as HBASE. As discussed earlier, due to consistency issues with the OpenStreetMap (OSM) dataset at more detailed levels, only major roads were included in the final HBASE product. Other UA classes with low agreement with the HBASE product included discontinuous very low-density urban fabric and sports and leisure facilities, which have a low percentage of built-up surfaces and are more likely to be merged with other non-HBASE objects.

Table 2-5: Areal proportion of UA classes classified as HBASE/urban by HBASE product and other urban datasets including GlobeLand30, GHSL, and GUF.

Urban Atlas land use class	Percent classified as HBASE	Percent classified as urban by GlobeLand30	Percent classified as urban by GHSL	Percent classified as urban by GUF
"Urban" classes				
Continuous urban fabric	91.4%	88.9%	88.0%	88.0%
Discontinuous dense urban fabric	85.4%	71.3%	73.1%	78.2%
Discontinuous Medium density urban	75.3%	55.3%	54.0%	62.9%
Discontinuous low density urban fabric	60.5%	37.3%	33.2%	45.1%
Discontinuous very low density urban	40.5%	25.4%	18.7%	29.5%
Isolated structures	4.9%	3.2%	9.5%	13.5%
Industrial, commercial, public,	67.6%	71.5%	71.9%	64.5%
Fast transit roads and associated land	71.6%	26.5%	55.4%	16.0%
Other roads and associated land	43.0%	41.4%	38.4%	36.4%
Railways and associated land	47.5%	43.7%	42.3%	29.0%
Port areas	83.0%	87.8%	85.8%	74.8%
Airports	68.0%	84.3%	34.5%	11.8%
Construction sites	61.4%	57.4%	35.0%	11.1%
Mineral extraction and dump sites	27.2%	36.3%	48.7%	28.8%
Land without current use	68.3%	73.0%	40.1%	30.2%
Green urban areas	60.3%	60.9%	27.0%	19.1%
Sports and leisure facilities	42.8%	45.5%	26.7%	21.8%
All "urban" classes in Urban Atlas (excluding construction, mines, and land without current use)	**49.3%**	**50.5%**	**44.4%**	**41.6%**
All "urban" classes in Urban Atlas	**51.5%**	**48.5%**	**44.2%**	**41.0%**
"Non-urban" classes				
Agricultural classes	2.8%	4.4%	1.8%	0.9%
Natural and semi-natural areas	1.5%	1.7%	0.6%	0.3%
Wetlands	1.0%	4.6%	1.4%	0.2%
Water	0.4%	3.4%	4.1%	2.1%
All "non-urban" classes	**2.7%**	**3.4%**	**1.4%**	**0.7%**

2.3.2.3 Comparison with Other 30m-grade Products

First, four of the urban products with 30 m or higher spatial resolution were compared visually (**Figure 2-4**). Because of differences in the definition and

methodology, there were apparent differences in the spatial characteristics among them. First, the final HBASE product and GlobeLand30 tended to include more pixels in the HBASE/urban boundary, especially in low-density areas, as demonstrated by the Berlin and Davos test sites. Second, the GHSL and GUF datasets contained more small patches than HBASE and GlobeLand30. Third, the HBSE dataset showed more commission errors in areas with agricultural land use, while the GHSL dataset showed more commission errors in bare areas. Finally, the GUF dataset captured only buildings, a result expected based on its definition and SAR-based methodology.

Table 2-6: Agreement matrix between HBASE and other datasets including GlobeLand30, GHSL, and GUF over the entire Europe, with values normalized by the total number of valid pixels Europe.

	Non-HBASE	HBASE	Total	Producer's Agreement
GlobeLand30 non-urban	95.57%	1.45%	97.02 %	98.50%
GlobeLand30 urban	1.25%	1.73%	2.98%	58.05%
Total	96.82%	3.18%	100%	/
User's Agreement	98.71%	54.40%	/	97.30% (overall agreement)
GHSL non-urban	96.88%	1.24%	98.12%	98.74%
GHSL urban	0.71%	1.17%	1.88%	62.23%
Total	97.59%	2.41%	100%	/
User's Agreement	99.27%	48.55%	/	98.05% (overall agreement)
GUF non-urban	96.44%	1.46%	97.90%	98.51%
GUF urban	0.80%	1.30%	2.10%	61.9%
Total	97.24%	2.76%	100%	/
User's Agreement	99.18%	47.1%	/	98.74% (overall agreement)

The overall agreement between the derived HBASE product and GlobeLand30, GHSL, and GUF datasets was > 97% when all nonurban classes in the compared datasets were considered as non-HBASE and their urban classes as HBASE. However,

the agreement matrices between these products (**Table 2-6**) showed that areas in which the HBASE and other datasets agree were dominated by nonurban/non-HBASE pixels. Considerable disagreements were found based on the user and producer metrics. Approximately 50% of the HBASE pixels were classified as urban by other datasets, while ~60% of the urban pixels in other datasets were classified as HBASE.

Using metrics calculated from the impervious surface based and functional urban area based assessments, I further analyzed these disagreements. First, from the impervious surface based assessments (**Table 2-4**), the HBASE and GlobeLand30 products clearly included more pixels with no impervious surface cover (0%) than other datasets, especially compared with the GHSL and GUF datasets. This does not necessarily imply that HBASE and GlobeLand30 had higher commission errors because the HBASE and GlobeLand30 products included more urban green space than GHSL and GUF, as shown by FUA-based assessments (**Table 2-5**). However, the HBASE and GlobeLand30 products included more agricultural and natural and semi-natural areas (**Table 2-4**). Second, HBASE consistently mapped more urban areas for all impervious surface percentage intervals (**Table 2-4**) and mapped more FUAs (**Table 2-5**), as defined by the UA dataset. Third, HBASE, GlobeLand30 and GHSL mapped over 90% of the pixels with high impervious cover (>75%), while the GUF product only mapped ~80% of these pixels, likely because of the exclusion of flat-built surfaces (e.g., parking spaces and roads) in the definition of GUF. Finally, GlobeLand30 had similar characteristics with HBASE but appeared to have slightly higher omission errors than the HBASE product in areas with 50% or higher impervious surface cover. However, it mapped less areas with no impervious cover as urban land (**Table 2-4**). In

terms of functional types, the HBASE product had better accuracies in mapping all five urban fabric classes and fast transit roads and associated land, railroads and associated land, and construction sites, while the GlobeLand30 mapped more areas as ports, airports, mineral extraction and dump sites, and land without current use (**Table 2-5**).

2.3.3 European HBASE Area Estimation

According to the derived HBASE product, the total human built-up and settlement area in Europe was 308,564 km^2 in 2010, which is ~ 3.18% of the total land area of Europe. This estimate is comparable to the total urban area calculated based on the GlobeLand30 product (2.98% of total land area), ~60% more than the GHSL and GUF products (less than 2% of total land area), approximately twice as much as that calculated using the MODIS land cover product (less than 1.5% of total land area), three times the GlobCover product (less than 1% of total land area), and 40% of the total settlement area based on the GRUMP product (7.85% of total land area) (**Table 2-7**). The differences in the total urban land area estimates were consistent with the differences in their definitions. Furthermore, the percentage of HBASE area per country varied substantially among European countries, ranging from 1.41% in Norway to ~14% in Belgium. Again, these estimates were in general agreement with the percentage of urban areas calculated using the GlobeLand30 product but differed substantially from those derived using the other three coarse-resolution global products (**Figure 2-6**). Finally, there was modest disagreement between HBASE and GHSL/GUF products, which is expected based on the differences in the definition.

Table 2-7: Estimated urban area from HBASE and other urban products for European countries/regions (countries/regions smaller than 2000 km^2 are listed together as "all other countries/regions").

Country/ Region	Land Area (km^2)	Urban Area (km^2)						
		HBASE	Globe Land30	GHSL	GUF	Glob Cover	MODIS	GRUMP
Albania	28738	443	565	467	406	321	198	1525
Austria	83852	3895	3683	2930	2432	861	1984	11102
Belarus	206845	5319	6970	1086	2366	1315	1335	7897
Belgium	30707	4334	4344	4713	3568	1416	3241	12578
Bosnia and Herzegovina	51065	1051	898	413	547	77	369	1317
Bulgaria	111585	3422	5117	1926	2137	2221	2513	6075
Croatia	57085	2065	1799	1129	1229	187	689	4765
Czech	78768	4327	5074	3463	3417	1065	3415	11388
Denmark	43140	3286	3036	2123	1912	921	796	9584
Estonia	45484	666	966	201	269	187	181	2646
Finland	336917	5414	5863	854	1182	1567	472	19802
France	549494	28072	28281	23414	21165	7488	12179	75294
Germany	357538	29575	26867	27082	23275	10019	24636	60434
Greece	132559	4999	3984	2321	3053	2802	1952	18285
Hungary	93022	3771	5669	3356	3552	1277	3506	11068
Ireland	70374	2062	1236	1140	1036	471	282	5746
Italy	300753	28398	16786	16362	15533	12568	13556	73179
Latvia	64713	1178	1050	211	391	230	224	3420
Lithuania	65012	1150	2165	369	877	326	333	4967
Luxembourg	2580	328	217	211	161	58	146	796
Macedonia	24825	582	413	372	344	342	372	2685
Moldova	33906	755	2619	1248	932	227	1050	2085
Montenegro	13337	285	198	103	106	18	100	963
Netherlands	37670	4549	4973	5905	4112	2574	4458	12415
Norway	325097	4589	3462	1916	1133	237	362	19315
Poland	312060	15991	13136	8288	9300	3824	7950	26490
Portugal	91877	6594	4236	4097	3669	2479	759	12476
Romania	238326	4921	13571	5951	5071	1441	5341	14389
European Russia	3935012	60894	42872	18681	31160	10646	15274	118063
Serbia	78225	2378	2123	1019	1876	304	1789	5913
Slovakia	49068	1649	2616	2079	1597	356	1691	6866
Slovenia	19979	582	711	673	462	119	332	2662
Spain	506014	23014	12557	9257	10146	8123	4544	69326
Sweden	450019	6249	6111	2067	2451	1555	1242	36453
Switzerland	41248	2499	2007	2321	1673	450	1274	8055
Ukraine	601189	8566	36467	14876	11130	4846	10300	27214
UK	245446	19550	16622	14370	13214	10244	8620	54262
All other countries	4753	347	293	241	205	121	162	1452
European Total	9718278	308564	289556	187235	187086	93284	137625	762950

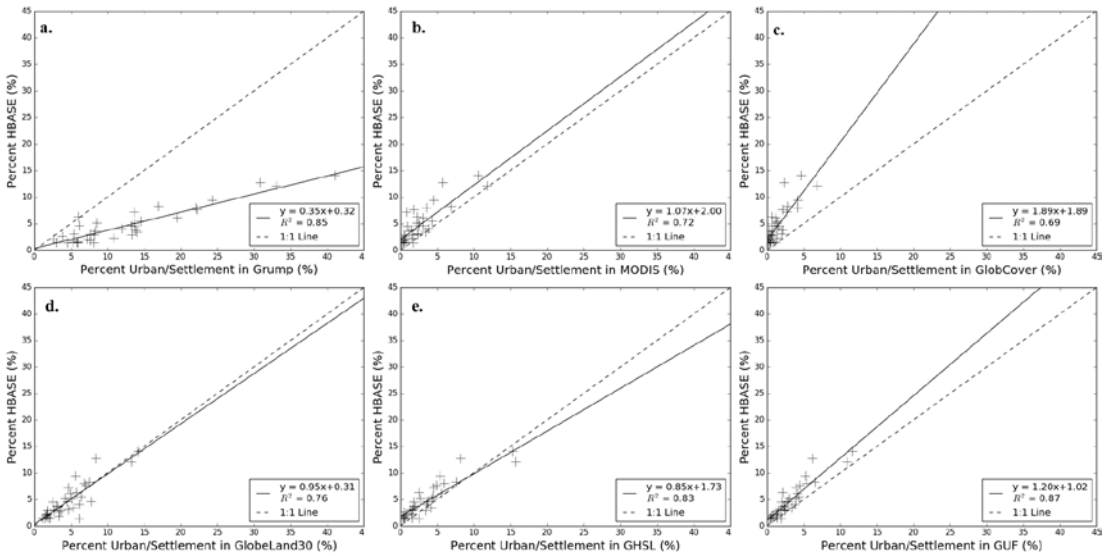

Figure 2-6: Scatterplots between country-level percentages of HBASE areas and percentages of urban areas estimated from (a) GRUMP, (b) MODIS, (c) GlobCover, (d) GlobeLand30, (e) GHSL, and (f) GUF products.

2.3.4 Global HBASE Product

A global random forest classification model was trained using global training dataset, based on the same HOTex method used for producing the European HBASE product. Applying this model and post-processing steps defined in Subsection 2.2.3.4 to the entire GLS 2010 dataset, global HBASE maps were produced. A global HBASE mosaic was created based on the produced HBASE maps (see **Figure 2-7**). In areas where Landsat scenes overlap, the random forest output class with maximum probability was selected for the mosaicked product. Although the accuracy of the global HBASE product is yet to be assessed, it was found to be a good representation of the overall spatial pattern of global urban areas. Large clusters of urban areas in the world, including those in Northern America, Western Europe, and Eastern Asia, were well characterized in the global product. Beside, no wide-spreading errors of commission

were found, particularly in arid and semi-arid regions, where HBASE could be confused with other non-urban land cover types.

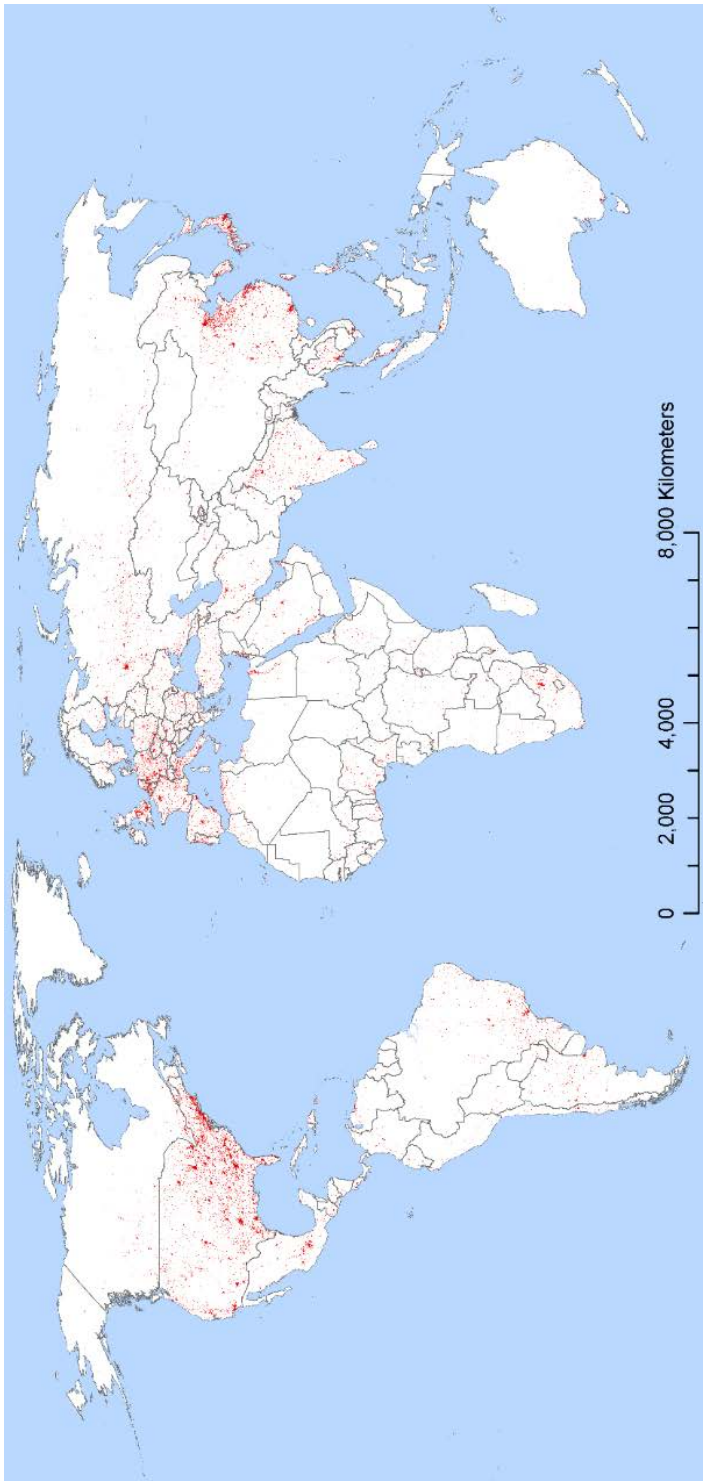

Figure 2-7: Circa-2010 global HBASE map (red: HBASE, white: non-HBASE, projection: Robinson).

2.5 Discussion

Human built-up and settlement areas, or HBASE as defined in this study, are inherently difficult to map using only spectral-based methods. Consisting of buildings, pavements, and vegetated and non-vegetated surfaces surrounding them, these areas typically have a large within-class spectral variability and low spectral separability between some of the surface materials within and outside of HBASE areas. The close proximity of built-up and adjacent surfaces and the way they are arranged, however, create textures that are often unique to HBASE areas and hence can be used to characterize those areas. Designed based on this phenomenon, the HOTex has several features that makes it possible to provide a robust approach for Landsat-based mapping of HBASE at continental to global scales.

First, due to differences in the acquisition date, location, vegetation phenology, illumination geometry, and other factors, the spectral data of Landsat images needed to cover large areas typically have substantial within-image variations not related to surface characterization, which can lead to inconsistent classification results derived using spectral-based methods. To minimize the potential negative impacts of inconsistent spectral data among Landsat images, the HOTex algorithm relied heavily on texture variables. No Landsat band or spectral index was used as a predictor variable in deriving the HBASE classification. To increase the class separability in different seasons over different areas, I explored several ways to expand the information contents of the selected texture variables. For each texture variable, I used two rescaling threshold values to increase its sensitivity at different brightness levels. In addition to conventional single band textures, I explored cross-band information by using “color”

textures. In addition, spatial information at different scales was considered by calculating textures at three object levels.

In addition to using the Landsat-based texture variables, the HOTex algorithm appeared to be effective in leveraging the consistency and additional information provided by MODIS and VIIRS-DMSP composites. By providing information on local and regional vegetation phenology and environmental conditions, the MODIS data contributed to a 4.9% increase in the user's accuracy (**Table 2-4**). While the initial intention of using the VIIRS–DMSP nightlight data was to improve the separability between HBASE and some large non-HBASE areas, such as bare fields, desert, and other non-vegetated surfaces, this dataset also contributed to a 2.4% increase in the producer's accuracy . Together, these two datasets contributed to 5.2%, 2.9%, and 8% increases in the user and producer accuracies and kappa value, respectively.

The hierarchical segments produced by the RHSeg algorithm provided a good framework for integrating Landsat-based fine-scale textures with coarser-resolution MODIS and VIIRS–DMSP data. The use of image objects instead of moving windows with predetermined sizes to calculate textures eliminated a major problem of the latter approach, which typically produces abnormal texture values along the edges between image objects and hence often results in large classification errors in those areas (Gong 1994; Hodgson 1998). The object level variables calculated by overlaying MODIS and VIIRS–DMSP data on the Landsat-based image objects provided an effective way to minimize the impact of the larger footprints of MODIS and VIIRS–DMSP data, which often results in a blocky appearance of the derived fine-resolution data products. Such a blocky appearance was not observed for the final HBASE product (e.g., **Figure 2-4**).

Overall, the use of multi-level objects and expanded texture measures together with globally consistent MODIS and VIIRS–DMSP data provided a consistently better separability between HBASE and non-HBASE areas than the use of Landsat spectral data alone. Due to substantial within-image differences present in the GLS 2010 dataset (Gutman et al. 2013), an HBASE classification derived using a spectral-based approach would have substantial errors and obvious seamlines between adjacent images (**Figure 2-8**). No visible seamlines were found in the final HBASE product derived using the HOTex approach and most of the errors in the spectral-based product were eliminated (**Figure 2-8**).

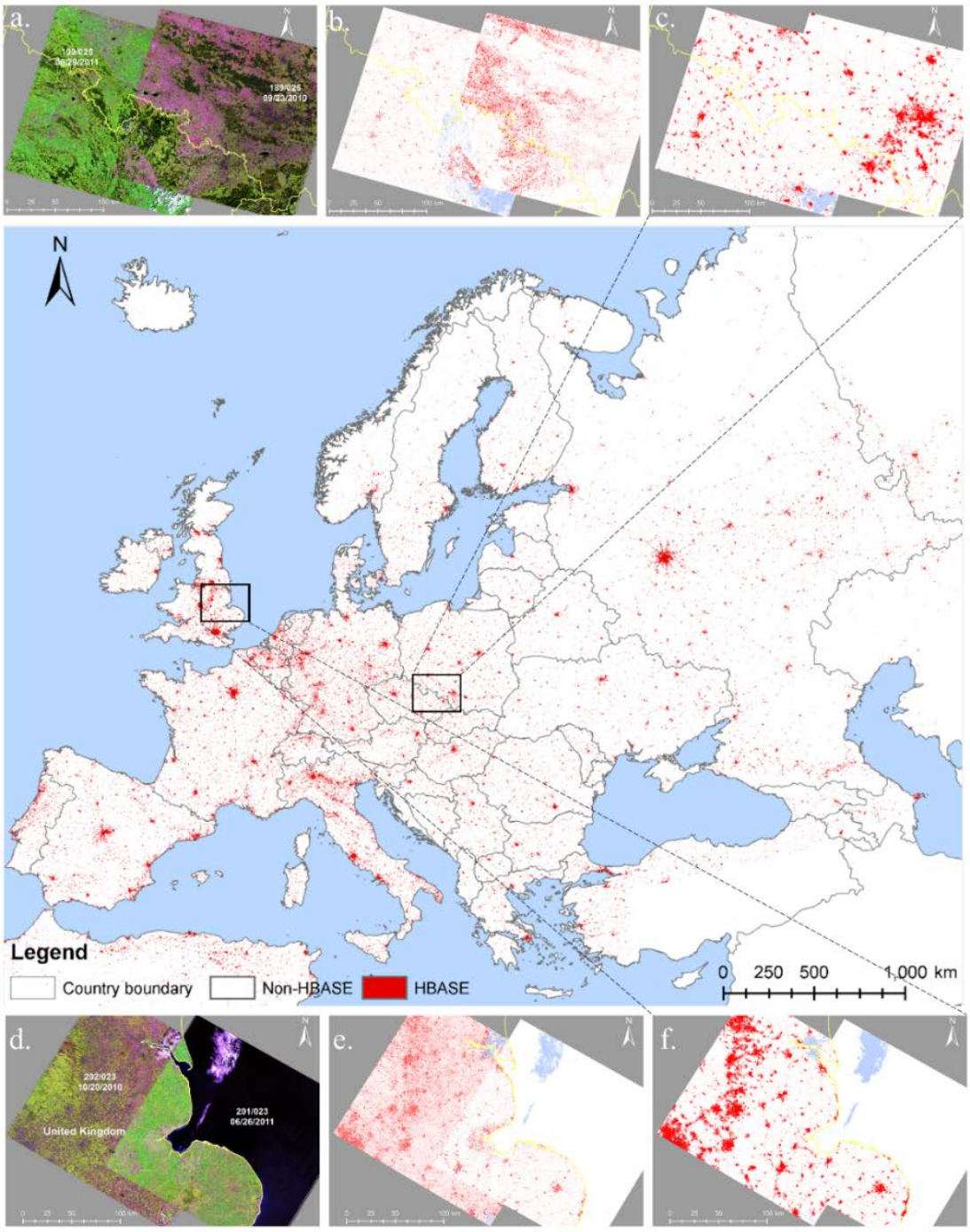

Figure 2-8: Continental mosaic of HBASE products over Europe and regional mosaics for two sets of overlapping Landsat tiles: (a) Landsat images p190r025 and p189r025; (b) spectral-based classification for (a); (c) classification for (a) using the HOTex method; (d) Landsat images p202r023 and p201r023; (e) spectral-based classification for (d); (f) classification for (d) using the HOTex method.

Because of the vital roles of image objects in the HOTex algorithm, the quality of the products derived using this algorithm depends on the quality of the image segmentation. For the Landsat 7 images in the GLS 2010 dataset that had residual SLC-off gaps (Gutman et al. 2013), contiguous image objects that formed by individual land cover patches were broken into multiple pieces in arbitrary ways. While we mapped the HBASE using those Landsat 7 images by including training samples selected to represent the "broken" objects, negative impacts of the SLC-off gaps on the derived HBASE product were notable. **Figure 2-9** shows two examples of HBASE products in areas with SLC-off gaps. The HBASE/non-HBASE boundaries were mapped reasonably well for the London test site, although there were breaks introduced by the gaps. However, the mapped boundaries for the test site in Vasteras, Sweden, exhibited discontinuities, where SLC-off gaps were present. Because the 2010 GLS collection only includes 26.8% of the Landsat 7 images and the percentage of total European land area covered by SLC-off gaps is less than 0.4%, the overall impact of this issue on the data quality is limited. For future studies, two approaches might be useful for removing artifacts and data gaps associated with the SLC-off problem. First, by fusion with the GUF product, which is not affected by the SLC-off problem, the data quality in affected areas could be significantly improved. Second, great efforts have been made to develop synthetic or composited Landsat datasets and improve the spatial and temporal consistencies at continental to global scales (Roy et al. 2010; White et al. 2014; Zhu et al. 2015). Based on the assessment of the quality of image objects derived using such synthetic or composited datasets, they might be a valuable alternative data source for large-scale HBASE mapping.

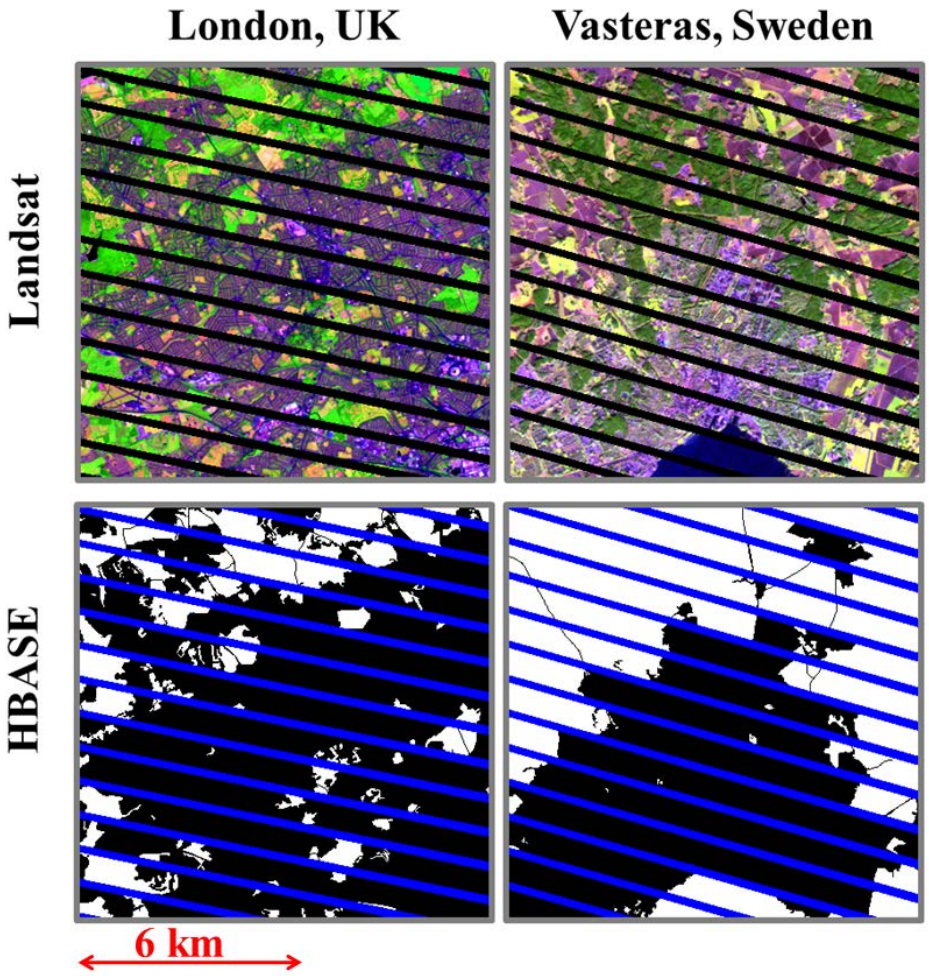

Figure 2-9: Examples of the effect of SLC-off gaps on the HBASE products for London, UK, and Vasteras, Sweden (black: HBASE, white: non-HBASE).

Statistically, the HBASE products derived in this study were comparable to the GlobeLand30 product associated with an urban/nonurban classification. The country-level percentage of HBASE/urban areas derived using these two datasets was comparable (**Figure 2-6**). When assessed according to imperviousness and urban functional areas, they produced similar results, with those derived using the HBASE product being slightly better since HBASE maps more impervious surface or urban related classes. At the pixel level, however, the overall agreement between the two products was 97.3%. While some of the disagreements could be contributed to

commission and omission errors of each product, others were due to differences in the local boundaries between HBASE and non-HBASE in the HBASE product and those between urban and nonurban in the GlobeLand30 product. In particular, many urban areas in the GlobeLand30 product had boundaries that appeared to be the result of "manual interaction," which was part of the pixel–object–knowledge (POK) approach used to produce that product (Chen et al. 2015a). While it was not clear how much human effort was required to meet the needs of "manual interaction" in producing the GlobeLand30 product as the direct output of the RF algorithm superimposed with major roads from the OpenStreetMap, the HBASE product did not require any human editing during post-classification processing and hence had more "natural" boundaries resembling those of the input Landsat images (**Figure 2-4**).

I acknowledge that the use of the OpenStreetMap to address the limitations of Landsat data in mapping roads may introduce uncertainties, especially in developing countries, where both government and user-generated data are relatively scarce. To the best of my knowledge, no global- or continental-scale assessment of the quality of OpenStreetMap has been published. Therefore, I only included major roads, as listed in Section 2.2.3.4. I also used a separate label for roads in the final product, which enables the end user to exclude these road pixels or choose to use a different data source for roads.

The comparison with GHSL and GUF datasets showed that, in general, HBASE mapped more urban areas and is more likely to contain commission error. Although these disagreements need to be interpreted carefully because (a) there are differences in the definitions and (b) the UA dataset does not necessarily reflect the ground truth

and cannot be used as a basis for calculating the accuracy, the HBASE and these two datasets may have complimentary advantages. The fusion of HBASE and these datasets may have potential for producing a harmonized urban extent map with higher quality.

By comparing 30m grade urban products with coarser resolution datasets, this study demonstrated the need for 30 m or finer-resolution datasets for mapping human built-up and settlement areas. Although two of the 30 m products considered in this study, including the HBASE product from this study and the GlobeLand30 product, were produced independently using two different methods and had a relatively low overall agreement, they produced country-level and Europe-wide estimates of HBASE and urban proportions that differed by less than 10%. The estimates from the other three coarser-resolution products ranged from ~30% to ~250% of those derived from the 30 m products. While definition and methodological differences were likely the main reasons for the large discrepancies among the three products, this likely was exacerbated by the inability to differentiate fine-scale HBASE features at coarse spatial resolutions. With an increasing amount of 30 m or finer-resolution satellite datasets becoming available, including those acquired by Landsat 8 and Sentinel-2, the highly automated HOTex algorithm makes it possible to routinely map HBASE and its change at continental to global scales.

2.6 Conclusion

A HOTex approach was developed to map the HBASE at continental and global scales. This approach used a segmentation algorithm to produce hierarchical image objects, which provided a framework for calculating multi-level textures and integrating coarser-resolution VIIRS–DMSP night light data and MODIS-based

phenology information in a Landsat-resolution classification. In Europe, the HBASE classifications derived using this algorithm had kappa values and user and producer accuracies of over 90% when evaluated using the SLCV approach designed to minimize potential biases in accuracy estimates due to spatial autocorrelations between training and testing data. Similar products derived using a traditional spectral-based classification method had SLCV accuracies below 80%.

The HOTex method was applied to GLS 2010 Landsat images to produce a circa-2010 global HBASE product. Based on an initial inter-product comparison for Europe, this product had a low commission error of 2.7% when evaluated using an European Urban Atlas dataset derived using high-resolution images. Omission errors varied substantially among different FUA types, but 80% or more of the areas with > 25% impervious cover were correctly mapped as HBASE. After being aggregated into an urban/nonurban classification, the GlobeLand30 product had comparable but slightly higher errors when evaluated using the same reference datasets. These two 30 m products provided comparable estimates of the total HBASE/urban areas for Europe and individual countries. The estimates of total urban land area derived from coarser-resolution products, such as the 500 m MODIS land cover product and the 300 m GlobCover, were half to one third of those derived from HBASE, but those from the 1 km GRUMP dataset were approximately three times that of the 30 m estimates. Although GHSL and GUF have modest disagreements with the HBASE because of differences in the definition, they agree with HBASE reasonably well in areas for which their definitions agree.

This study demonstrated the effectiveness of the HOTex approach in consistently mapping HBASE areas at continental to global scales with a dataset exhibiting spectral inconsistency. Such spectral inconsistencies may arise from differences in the acquisition dates, illumination and viewing geometry, and vegetation phenology, among others, and are common for imagery products acquired by mid-resolution satellites such as Landsat and Sentinel-2. The use of multi-level objects and expanded texture measures together with globally consistent MODIS and VIIRS–DMSP data not only greatly reduced the negative impacts of such within-image inconsistencies but also provided a consistently better separability between HBASE and non-HBASE areas than the use of Landsat spectral data alone. In addition, given the ability to handle spectral inconsistencies, the HOTex approach may be useful for the mapping of urbanization using multitemporal images. Moreover, with minor adjustments, this approach likely will be effective for the mapping of other land cover types, especially those with clear patch boundaries. Future algorithm refinements and application to global scales are ongoing in conjunction with the GMIS sister project and final results will be provided through NASA's SocioEconomic Data and Applications Center (SEDAC, http://sedac.ciesin.columbia.edu).

Chapter 3: Mapping 2000-2010 Impervious Surface Change in India using Landsat Data

3.1 Introduction

The first decade of the 21st century witnessed rapid urbanization. More than half of the world's population now dwells in urban areas and the urban population is expected to reach two thirds of the world's population by 2050 (United Nations 2015). The physical manifestation of this global urbanization process on the Earth's surface includes the conversion of forests, grasslands, and croplands to impervious surface (IS) cover. The IS cover may alter the Earth's environmental systems in many ways: areas covered by IS may have a distinctive local climate, commonly known as the "urban heat island effect" (Arnfield 2003; Seto and Shepherd 2009). Hydrologic systems may be severely impacted as a result of increased runoff and degradation of the water quality (Arnold and Gibbons 1996). Urbanization is often associated with the loss of natural land, which may have adverse implications for biodiversity and other ecosystem services (Foley et al. 2005; Kaye et al. 2006) at local to regional scales. Moreover, recent studies on the linkages between urbanization and global environmental change have demonstrated that urbanization could have impacts well beyond the physical footprint of urban areas (Lambin et al. 2001).

However, monitoring urbanization as a process of impervious surface change (ISC) is an inherently difficult task. The IS only covers a small percentage of the Earth's land surface (estimates range from 0.2%–3%; (Liu et al. 2014; Schneider et al. 2009; Small 2004). In addition, urban areas are complex system in terms of both spatial

variability of the IS cover density within the urban extent and temporal dynamics throughout the urbanization cycle (Lambin et al. 2003; Lambin and Meyfroidt 2010; Lambin et al. 2001).

Much effort has been made towards representing IS or urban land cover in remote sensing-based global maps. Such datasets include global land cover datasets with urban class (Friedl et al. 2010; Hansen et al. 2000; Loveland and Belward 1997), binary urban/nonurban maps (CIESIN (Center for International Earth Science Information Network) 2011; Schneider et al. 2009; Zhou et al. 2015)], and continuous field IS cover maps (Elvidge et al. 2007). These datasets are produced using medium to coarse resolution data such as from the Moderate Resolution Imaging Spectroradiometer (MODIS) and the Defense Meteorological Satellite Program Operational Linescan System (DMSP-OLS). Only recently, 30 m resolution Landsat data are being used for mapping urban areas globally (Chen et al. 2015b; Gong et al. 2013). As valuable as these datasets are, monitoring urbanization requires much more detailed data than the available global products. The complexity of urban landscapes in the spatial domain requires very high-resolution (VHR) data to map (Jensen and Cowen 1999). Even at 30 m resolution, much of the IS cover is mixed with other non-impervious land cover types (Small 2003). To better map the spatial distribution of IS cover, Landsat spectral data have been used to produce continuous field IS cover products such as the United States National Land Cover Dataset (NLCD) percent IS (Yang et al. 2003). Similarly, at 30 m resolution, most non-impervious to impervious cover conversion is best characterized as a continuous field variable instead of discrete classes because continuous field variables better represent urban mosaics and

boundaries. Therefore, under the constraint of using publicly available datasets, mapping continuous field impervious surface change (ISC) at 30 m provides the best characterization of the spatiotemporal dynamics of urbanization.

Landsat-based IS has been mapped using spectral mixture analysis (Lu et al. 2014; Weng et al. 2008) and machine learning algorithms such as regression trees (Walton 2008; Xian and Homer 2010; Yang et al. 2003). Both methods are sensitive to seasonal and phenological variations within Landsat images (Wu and Yuan 2007; Yuan et al. 2008). As a result, seasonal phenology changes could lead to fluctuations of the estimated IS and thus biases and errors in the estimated ISC when images for the two dates are acquired from different seasons. Landsat time series could be used to produce more stable IS estimates and thus a more accurate ISC (Sexton et al. 2013b; Song et al. 2016). However, the data requirements for Landsat time series analysis may not be satisfied in many areas of the world, especially in areas with chronic cloud cover.

This study mainly aims to produce the ISC between 2000 and 2010 for India, a country with one of the fastest urbanization rates around the world (Pandey et al. 2013). India contributes currently ~10% of the world's urban population (Swerts et al. 2014). This number is expected to grow because its economic development drives future urbanization and more of its vast rural population migrate to urban areas (United Nations 2015). India also has a very diverse landscape, climate, and biome, making it an ideal place to test large-scale IS mapping. In addition to the primary goal, I also aim to produce quantitative assessments of the accuracies of the mapped ISC and state/country-level statistics of ISC for the entire country of India. Finally, the correlation between ISC and socioeconomic drivers of ISC, including population

growth and the growth of gross domestic production (GDP), are examined to validate the overall quality of the derived ISC product.

3.2 Study Area and Datasets

3.2.1 Study Area

The study area of this chapter is India, the country with the seventh largest area (near 3.3 million km^2) and second largest population (more than 1.2 billion as of 2016). India has experienced rapid urbanization in the first decade of the 21st century. From 2001 to 2011, the urban population has increased by 31.8%, at a much higher rate than the rural population growth (12.2%; (Office of the Registrar General & Census Commissioner of Inida 2011; Pandey et al. 2013). With this significant rate of urbanization, India faces many challenges. In a previous study, it was found that ~24% of the districts in India experienced significant agricultural land loss (> 1000 hectare), which is mainly explained by urbanization (Pandey and Seto 2015). Urbanization in India also has adverse impacts on the biodiversity because important habitats are being converted to IS (Nagendra et al. 2013).

The impact of seasonal phenology change on remotely sensed IS is particularly severe in India. Because of the effect of the monsoon and spatial distribution of rainfall, different vegetation dynamics spread across the country (Tian et al. 2014). In addition, shaped by meteorological cycles, the spectral signatures of agricultural land in India change seasonally. For example, during dry months, fallow fields are often confused with ISs, which are difficult to separate with single temporal data (Haack et al. 2002).

3.2.2 Global Land Survey Surface Reflectance Datasets

As described in Subsection 2.2.1.1, Global Land Survey (GLS) datasets are global, mostly cloud-free, collections of orthorectified Landsat images. Up to now, GLS datasets for the nominal years of 1975, 1990, 2000, 2005, and 2010 have been made available (Gutman et al. 2013). In this chapter, I used 2000 and 2010 GLS surface reflectance (SR) datasets processed using the Landsat Ecosystem Disturbance Adaptive Processing System (LEDAPS; Masek et al. 2006) by the Global Land Cover Facility (GLCF) at University of Maryland. To cover all land areas of India, 195 GLS Landsat scenes were used for each epoch.

3.3 Methods

3.3.1 Impervious Surface Mapping for 2010

A regression tree-based method was developed to map the IS for 2010 by the GMIS project (Brown de Colstoun et al. 2017). The GMIS project adopted a method similar to the NLCD IS product using Landsat spectral bands as input variables and IS percentages interpreted from high-resolution images as training data. In addition to the six Landsat spectral bands, the inputs to the regression tree model also included four spectral indices. These spectral indices were calculated as described in Subsection 2.2.3.3.

The regression tree model was generated by the Cubist™ software by Rulequest (Rulequest Research 2016), a machine learning algorithm widely used in mapping the IS and other continuous field land cover variables (Sexton et al. 2013a; Sexton et al. 2013b; Song et al. 2016; Walton 2008). In addition to the predicted variable, Cubist™

also generates mean absolute error (MAE) estimations, which I modified into root-mean-square error (RMSE) using a public version of the Cubist™ code.

Due to the spectral similarity between IS and other non-impervious land cover types, such as agricultural fields and bare land, regression trees tend to overestimate the IS cover in these areas. Therefore, an urban mask is needed to mask the IS predictions outside of the urban extent. Compared with the NLCD IS product, which uses a nighttime lights dataset derived from DMSP-OLS (Xian et al. 2011), the binary masks of human built-up and settlement extent (HBASE) developed in Chapter 2 were used by GMIS. Based on object-based texture information, HBASE includes both IS and non-IS covers within the urban boundary and smaller settlements such as towns and villages. The HBASE classification was performed using the Random Forest algorithm, an ensemble machine learning algorithm based on decision trees (Breiman 2001). With Random Forest, I generated not only the categorical classes for every pixel but also the probability of a pixel belonging to each class, which will be used later in this study (Section 3.3.2.3).

Training data for IS and HBASE machine learning models were collected worldwide for a global IS mapping project. In this study, I used models based on training datasets developed for the Asian continent to map the IS and HBASE in 2010. Initial assessments using cross-validation estimated the RMSE of IS to be 12.3% for the Asian IS model. Based on the results of the cross-validation for the Asian HBASE classification model, the user's accuracy , producer's accuracy , overall accuracy, and kappa statistic were 91.5%, 90.3%, 97.9%, and 90.0%, respectively.

3.3.2 Impervious Surface Mapping for 2000

3.3.2.1 Overall Algorithm Design

Based on the processing chain developed for the mapping of the 2010 IS, the task of estimating the ISC between 2000 and 2010 could be reduced to porting the 2010 IS model to map the 2000 IS. Due to differences in acquisition dates and imaging geometries between corresponding 2000 and 2010 GLS images, there are considerable spectral and phenological differences between images for these two epochs. As a result, the 2010 IS model could not be directly applied to GLS 2000. To produce more realistic and higher quality 2000 IS, the regression tree algorithm must be supplied with training data for the 2000 epoch. Instead of collecting training data for 2000, which cannot be achieved for many areas due to the lack of necessary high-resolution images, my approach for estimating the 2000 IS cover is featured by an iterative process designed to identify pixels with unchanged IS values between 2000 and 2010. Using the 2010 IS prediction for these pixels as training data, a regression tree was then developed to map the 2000 IS. The major steps of the overall methodology are shown as gray boxes in **Figure 3-1**. The following subsections will provide details on each of these steps.

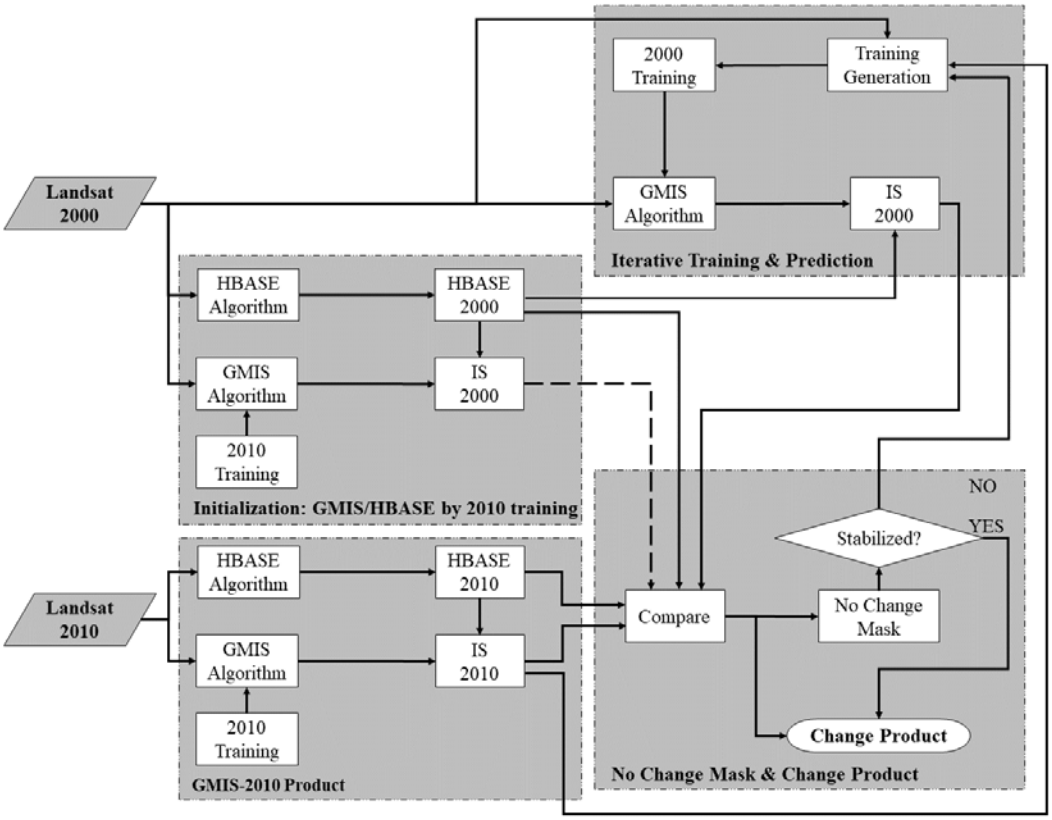

Figure 3-1: Overall schematic diagram for the impervious surface change mapping algorithm.

3.3.2.2 Algorithm Initialization

The initial estimation of IS-2000 was produced by simply applying the Cubist™ regression tree model used for the 2010 IS mapping to the 2000 Landsat images. I also applied the 2010 HBASE classification model to 2000 Landsat data to produce 2000 HBASE maps. Because the HBASE algorithm is based on the classification of texture features, which are not sensitive to spectral and phenological variations, I used this HBASE mapping result for all the subsequent analyses.

3.3.2.3 No Change Mask Generation

The goal of generating a “No Change” (NC) mask is to provide a set of pixels in which IS-2000 could be considered equal to IS-2010 with great confidence. Because the IS-2010 of these pixels will be used as training data to estimate IS-2000, I used the best information available and heuristics to obtain a conservative NC mask (this means that the NC mask is designed to include a minimum amount of change pixels). **Figure 3-2** shows the criteria for determining if a pixel is in the NC mask.

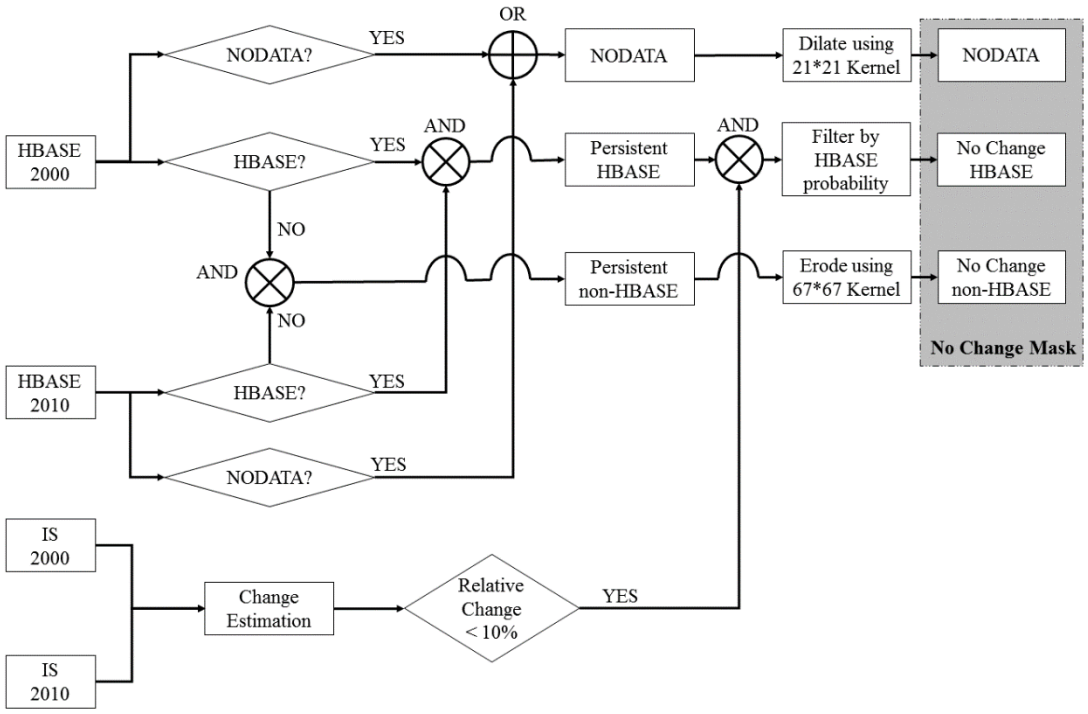

Figure 3-2: Schematic diagram for the “No Change” (NC) mask generation algorithm.

First, I considered pixels that were mapped as non-HBASE by the HBASE algorithm for both 2000 and 2010 as 0% impervious for both epochs. To further reduce the commission error, I applied an erosion morphological operator using a 67 by 67 kernel, which generated a set of pixels with at least 1 km (33 Landsat pixels) distance

to any HBASE pixel. The resulting pixels were labeled as “No Change non-HBASE” (NC-non-HBASE) in the NC mask.

Second, I considered pixels that were mapped as HBASE for both 2000 and 2010 by the HBASE algorithm. For these pixels, I calculated the relative impervious surface change between 2000 and 2010 as $2 \times (IS_{2010} - IS_{2000}) / (IS_{2010} + IS_{2000})$. I considered the pixels with less than 10% relative change to be “No Change HBASE” (NC-HBASE). Because the HBASE classification contains commission errors, the NC-HBASE category may also contain non-HBASE pixels. The use of such pixels to train the 2000 model may lead to systematic bias in the estimated 2000 IS. To filter out remaining non-HBASE pixels, I leveraged the class probability output of the HBASE classification model and removed from the NC-HBASE category pixels where the HBASE probability for either date is below a threshold. In this study, I used 60% as the threshold for HBASE probability. This threshold and the 10% threshold for relative change were empirically determined based on accuracy assessments of the ISC.

Finally, the HBASE product contains “NODATA” pixels when clouds/shadows or data gaps exist as a result of the failure of the Scan Line Corrector (SLC) of Landsat 7 (Gutman et al. 2013). I applied a dilation morphological operator using a 21 by 21 kernel to the “NODATA” pixels. This large buffer was designed to minimize the potential impact of pixels adjacent to bad observations during the identification of NC pixels.

3.3.2.4 Iterative Training and Prediction (ITP)

Based on the NC mask, I created for each GLS-2000 image a training dataset: pixels within the NC-HBASE class were assumed to have impervious surface cover as

predicted by the GMIS-2010 product; and pixels within the NC-non-HBASE class were given 0% IS cover. Using these training datasets, I trained Cubist™ regression tree models for each GLS 2000 image to predict the 2000 IS cover from Landsat data.

While I assumed that the IS values of all NC-HBASE pixels did not change between 2000 and 2010, some of those pixels could have changes in their IS values. For example, the redevelopment of an urban block could completely change the IS value of that block. Increasing the building density in a low density urban area will result in a substantial IS value increase. Such pixels should not be used as training pixels in developing the 2000 IS Cubist™ model. To identify such pixels, I adopted an iterative training and prediction (ITP) approach: the initial estimation of IS-2000 from the regression tree model based on 2010 training data was denoted as 0-th iteration; for the $k-th$ iteration, I generated a NC mask using IS-2000 from the $(k-1)-th$ iteration; the ITP process continued and generated a new IS-2000 based on the $k-th$ NC mask until the $k-th$ NC mask satisfied a stabilization criterion:

$$\frac{T_0 + T_1}{T_0 + T_1 + T_2} \times 100\% < 10\%, \qquad (3\text{-}1)$$

where T_0 is the number of pixels labeled as NC-HBASE for the $(k-1)-th$ NC mask but not the $k-th$ NC mask, T_1 is the number of pixels labeled NC-HBASE for the $k-th$ NC mask but not the $(k-1)-th$ NC mask, and T_2 is the number of pixels labeled NC-HBASE for both the $k-th$ and the $(k-1)-th$ NC mask.

When the stabilization criterion was met, I considered the NC mask to be accurate enough and used it to generate the final IS-2000. The HBASE-2000 from the

algorithm initialization stage was used to filter out overestimates of the IS in non-HBASE areas.

3.3.3 Quantification of 2000-2010 Impervious Surface Change

A simple subtraction of the final IS-2000 from the IS-2010 product was used to map the ISC between 2000 and 2010. In rapidly developing countries such as India, most urban changes increase the imperviousness. A predicted IS-2010 smaller than the predicted IS-2000 is much more likely due to natural factors such as changes in the vegetation phenology instead of real imperviousness decrease. Therefore, I set all pixels with negative ISC to 0.

To further reduce random errors in the ISC product, I utilized the RMSE output using the modified Cubist™ code. Under the assumption that IS2000 and IS2010 are independent, the standard error of an ISC prediction was estimated using:

$$\sigma_{ISC} \approx \sqrt{RMSE_{IS\,2000}^2 + RMSE_{IS\,2010}^2}, \qquad (3\text{-}2)$$

where $RMSE_{IS\,2000}$ and $RMSE_{IS\,2010}$ are the RMSE of the 2000 and 2010 IS predictions estimated by the Cubist™ regression tree algorithm. I applied a threshold of one standard error to the ISC predictions, which was determined empirically to minimize the RMSE of the estimated ISC. The ISC predictions below one standard error were set to zero.

3.3.4 Validation of 2000-2010 Impervious Surface Change

To assess the accuracy of the produced ISC dataset, I developed an ISC validation dataset using Google Earth™ imagery, which uses pan-sharpened QuickBird imagery with 61 cm resolution and pan-sharpened Worldview-2 imagery with 46 cm resolution as sources for the high-resolution image for the study period. The selection of validation points followed a three-step stratified sampling approach:

1. The 500 most populous Indian cities were classified into seven groups: more than 5 million, 1–5 million, 500000–1000000, 250000–500000, 100000–250000, 50000–100000, and less than 50000. From each group, I selected two cities. In total, I selected 14 cities that distribute across different regions of India.
2. A total of 18 Landsat scenes covering these 14 cities were identified.
3. For every Landsat scene, I randomly select 50 pixels from each of these four groups: $ISC = 0$, $0 < ISC \leq 25\%$, $25\% < ISC \leq 50\%$, and $ISC > 50\%$.

I then searched the historical Google Earth™ imagery archive to find two images closest to the 2000 and 2010 GLS image acquisitions dates for each of the 3600 sample points. For the use as ISC validation points, the following rules had to be satisfied:

1. The difference between the Google Earth™ and Landsat image acquisition dates is within two years (730 days) for both 2000 and 2010. This constraint could be relaxed if multiple Google Earth™ images with the same ISC were found before, during, and after the date range between GLS-2000 and GLS-2010.
2. There are no clouds/shadows in the Google Earth™ image for both dates.

3. There are no apparent misregistration errors between the two Google Earth™ images.

A Google Earth™ imagery interpretation tool was developed to estimate the ISC (Figure 3-3). Using the rules listed above, I determined that 1322 points were interpretable, which accounts for approximately 1/3 of the randomly sampled validation points. Among the 2278 dropped points, 1835 points were uninterpretable because of the first rule and the rest were dropped because substantial misregistration was identified between the Google Earth™ images for two dates. Although the randomness of the samples may be compromised after filtering out the uninterpretable points, the validation datasets are still spatially distributed across all of India and represent the entire range of ISC (Figure 3-4). For each of the usable validation points, the extent of the Landsat pixel was overlaid on 2000 and 2010 Google Earth™ images. The Landsat pixel to be validated was divided into 10 by 10 grids. By counting the number of grids with IS cover, I estimated the IS for 2000 and 2010. For example, 87 out of 100 grids were covered by IS in 2010 and no grid was covered by IS in 2000 (Figure 3-3). Therefore, I estimated that IS 2010, IS 2000, and ISC were 87%, 0%, and 87%, respectively.

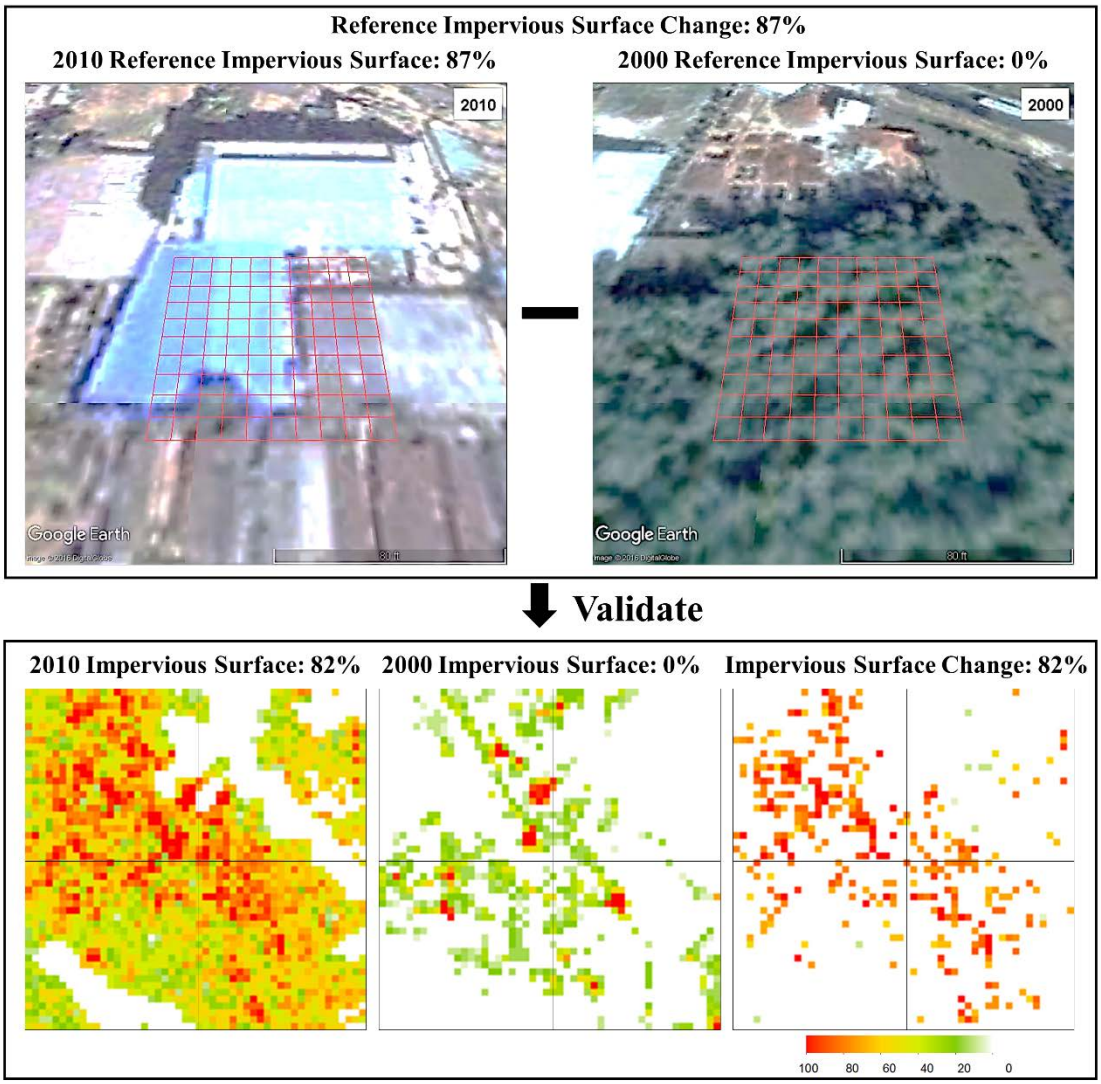

Figure 3-3: The impervious surface change validation tool based on Google Earth™: the red square in the upper panels, which is further divided into 10×10 grids, shows how the extent of the validated pixel overlays with Google Earth™ high-resolution data at two dates; the difference between impervious surface estimations for two dates is shown in the lower panels and is used as reference impervious surface change and to validate the impervious surface change product.

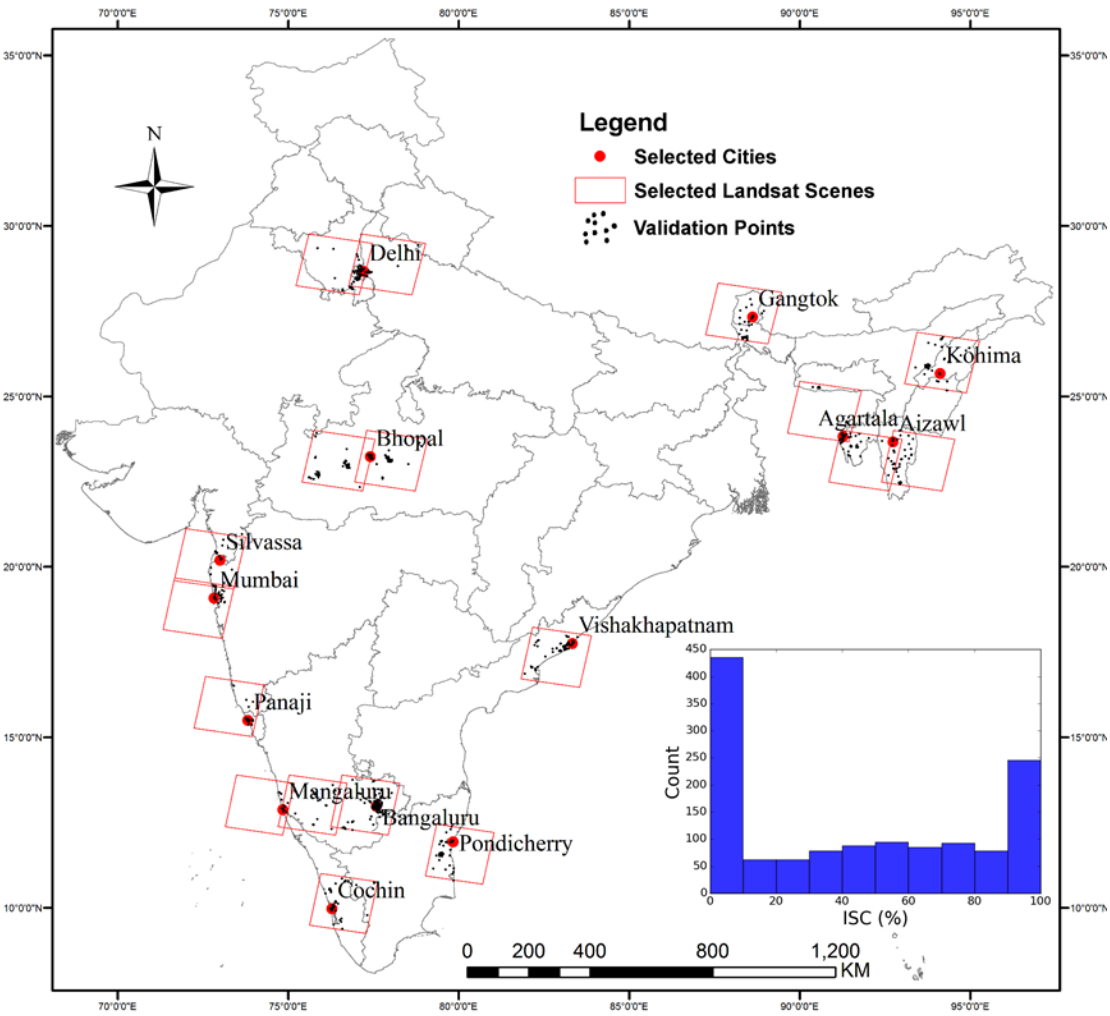

Figure 3-4: Distribution of selected cities, Landsat scenes, and validation points from the sampling. The histogram shows the distribution of the reference impervious surface change (ISC) used for validation.

3.4 Results

3.4.1 Visual Assessments of the IS and ISC products

I first assessed the quality of the bias-corrected ISC product by visual comparison against Google Earth™ images. I found that the ISC mapping method performs well in different areas with a wide range of landscape characteristics and urban densities. In **Figure 3-5**, site (a) is an area that was converted from an agricultural

field to a high-density IS. The 2000 IS correctly mapped the center pixel as 0% and the 2010 IS mapped it as 95% impervious. **Figure 3-5**b shows an agricultural area converted to low- to medium-density IS cover. The ISC product predicted a 44% increase of the IS cover. **Figure 3-5**c shows a bare area that was started to be developed prior 2000 and was continued to be converted to a low- to medium-density IS cover. The mapped ISC is 90%. **Figure 3-5**d shows a medium-density area expanded with new high-rise residential buildings. The proposed method mapped newly built areas as > 90% ISC. **Figure 3-5**e shows that a new airport was mapped correctly.

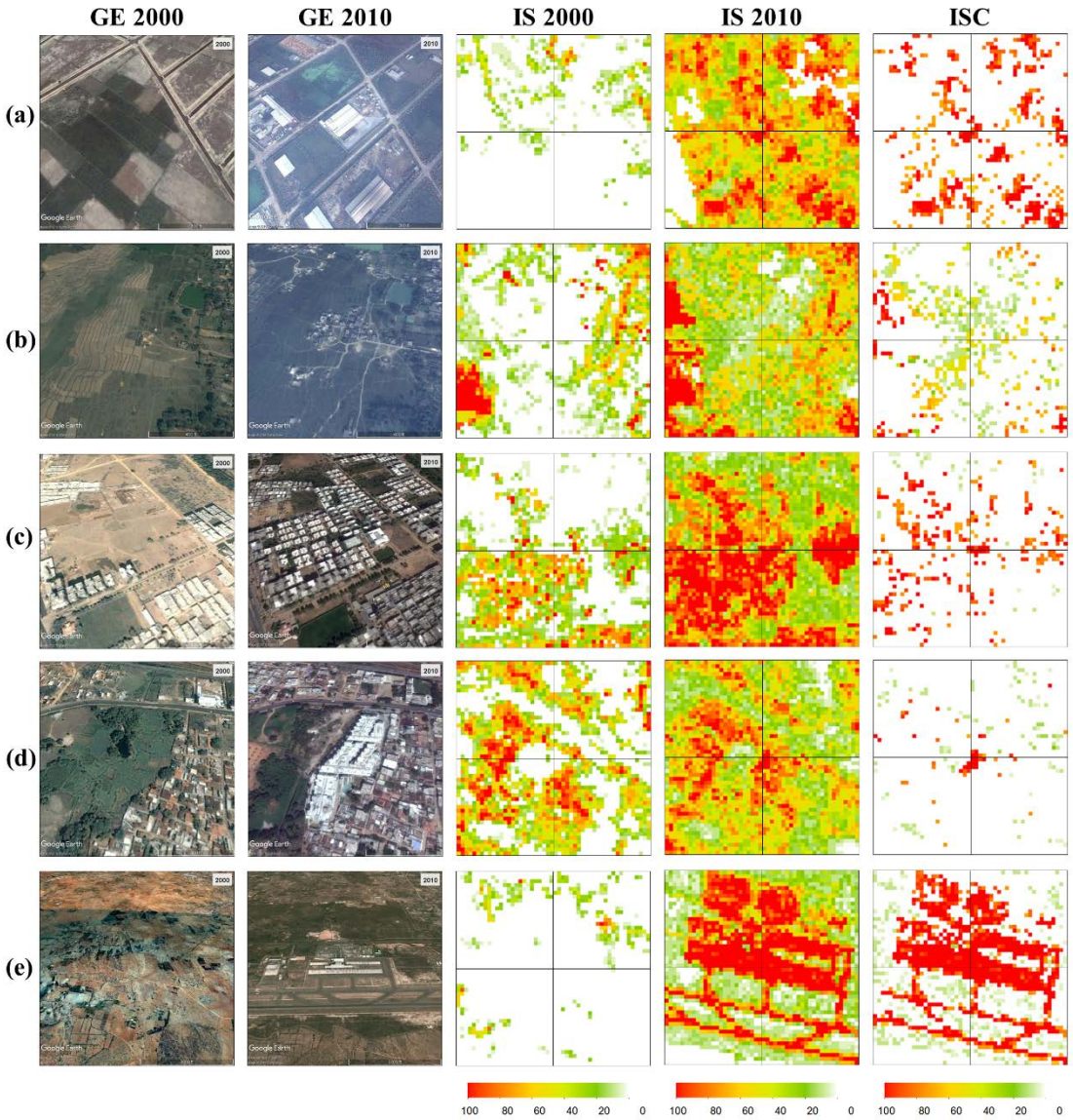

Figure 3-5: Examples of impervious surface change products for (a) an area converted from an agricultural field to a high-density impervious surface, (b) an agricultural area converted to low- to medium-density impervious surface cover, (c) a bare area that was started to be developed prior 2000 and was continued to be converted to low- to medium-density impervious surface cover, (d) a medium-density area expanded with new high-rise residential buildings, and (e) a newly built airport in a non-impervious area.

Although the visual representations of ISC indicated a good overall performance, I identified several types of errors in the IS and ISC products. In **Figure 3-6**a, an area remaining agriculture land during the 2000–2010 period was mapped as low- to medium-density IS cover for 2010, which resulted in a predicted ISC of 20%–40%. Mining areas are a major source of error as shown in **Figure 3-6**b. Both 2000 and 2010 versions overestimated the IS in this area. The expansion of mining caused an ISC prediction of > 90%. Turbulent water bodies were found to be confused with IS. In **Figure 3-6**c, the river was correctly mapped as 0% impervious in 2000 but showed ~20% IS retrievals in 2010. There were also cases in which the ISC was underestimated. **Figure 3-6**d shows a low-density town undergoing intensification. However, the IS products mapped only a few road pixels for both dates. This is caused by the omission error of the HBASE maps. **Figure 3-6**e shows an area in which fallow agricultural fields were converted for industrial use. The 2010 IS product mapped the high impervious cover correctly. However, because the IS 2000 product predicted medium IS with high standard error, the predicted change did not exceed one standard error and was set to zero.

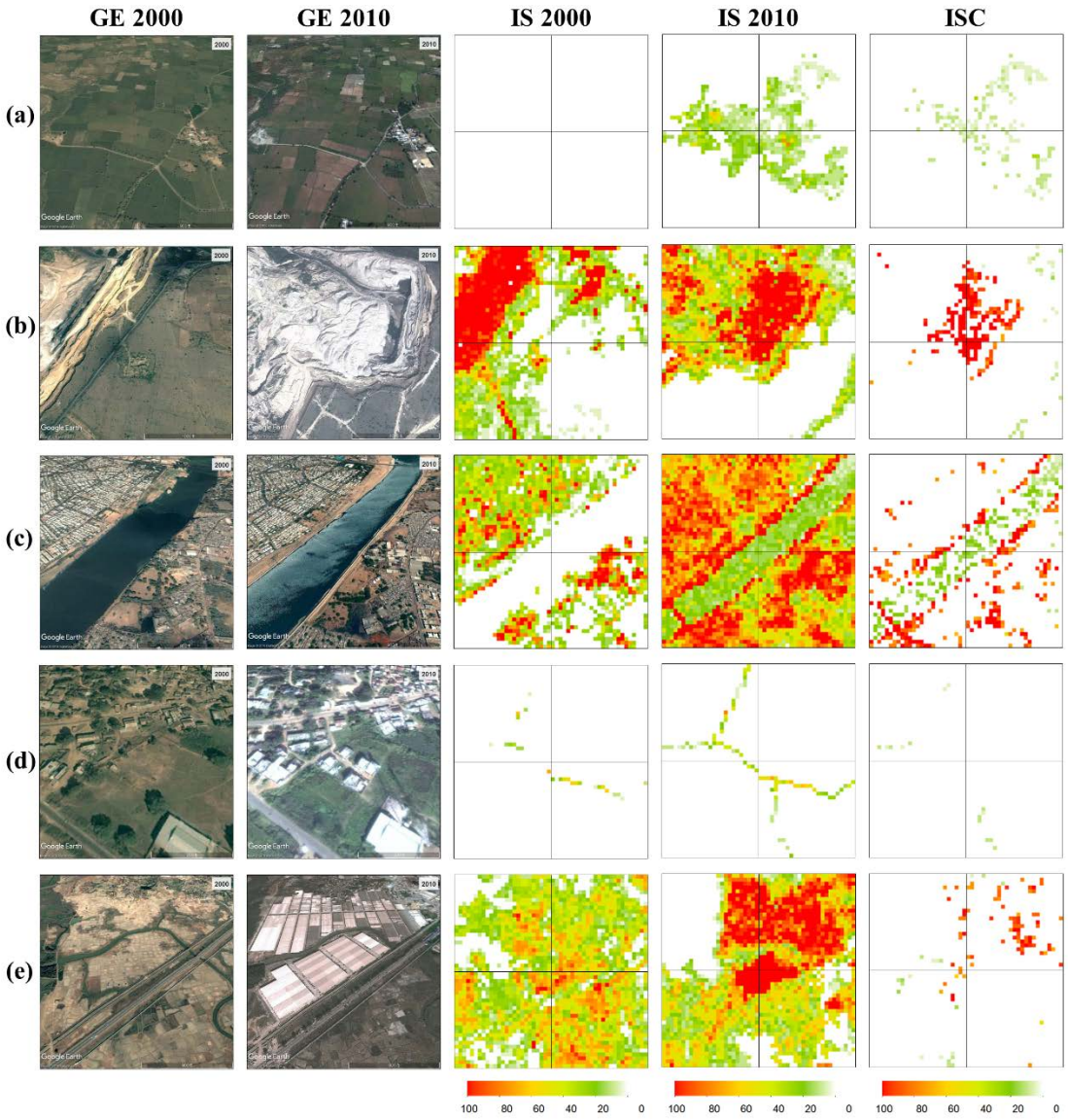

Figure 3-6: Examples of impervious surface change products for (a) an area that remained agriculture land during the 2000–2010 period with overestimated impervious surface change, (b) a mining area, (c) a river with ~20% ISC predictions, (d) a low-density town undergoing intensification, and (e) an area converted from an agricultural field to a high-density impervious surface.

A mosaic of the ISC product for the entire country of India was created to examine its overall spatial distribution pattern (**Figure 3-7**). First, the ISC changes are mainly distributed near larger urban centers (e.g., New Delhi, Mumbai, and Bengaluru), which have experienced strong population and economic growth during the 2000–2010

period. Second, Uttar Pradesh, Maharashtra, Gujarat, and Tamil Nadu are among the states with the highest ISC, which agrees with a MODIS-based analysis of agricultural land to urban land conversion in India (Pandey and Seto 2015). Finally, as shown by the zoom-in views for New Delhi and Bengaluru, most of the IS changes occurred in the urban fringe areas, which is an accurate representation of the urban development patterns of these two cities.

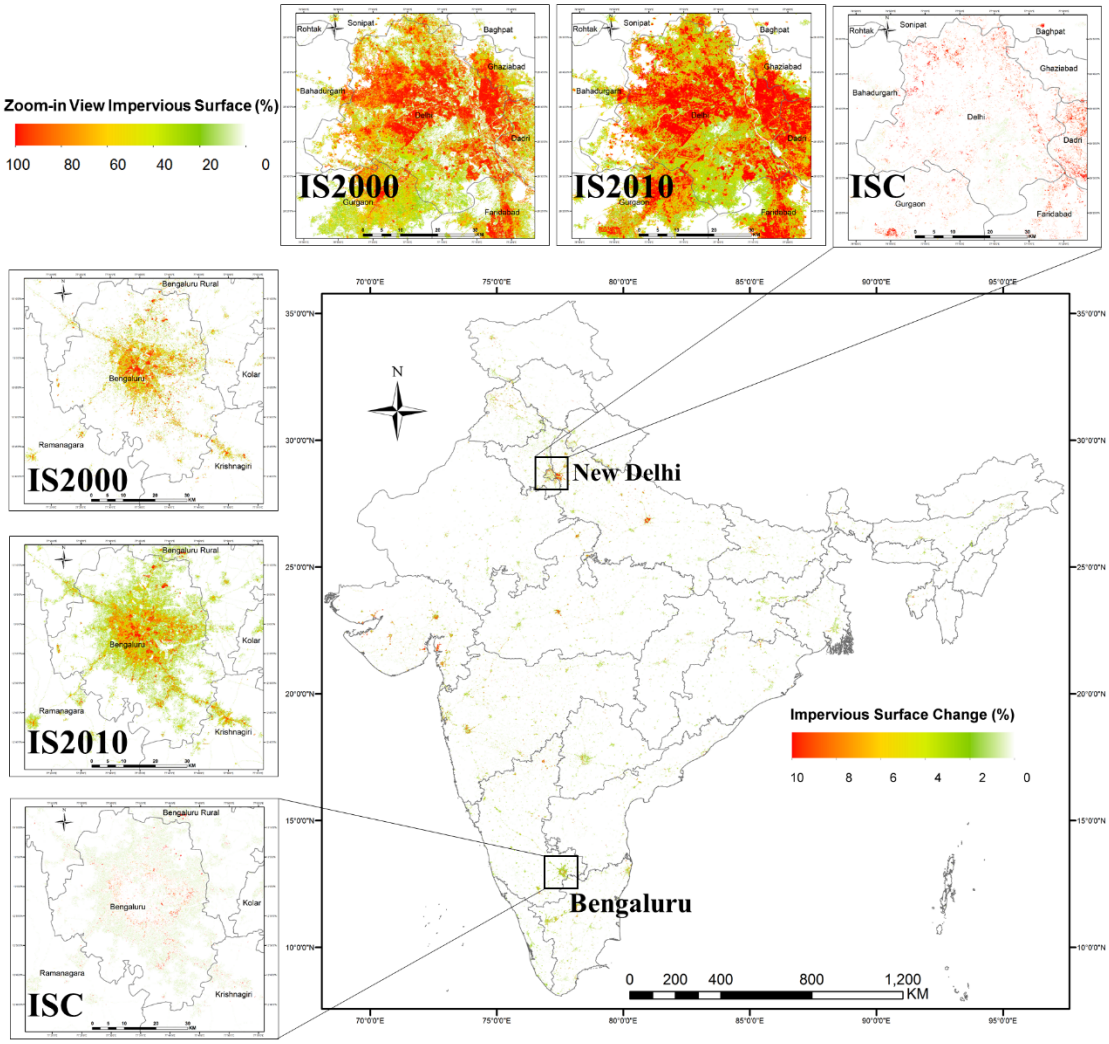

Figure 3-7: The 300 m mosaic of India's impervious surface change product (Lambert Azimuthal Equal Area projection). The zoom-in views of the 2000 impervious surface (IS2000), 2010 impervious surface (IS2010), and impervious surface change (ISC) are provided for New Delhi and Bengaluru at 30 m resolution.

3.4.2 Accuracies of IS and ISC products

The validation dataset developed in Subsection 3.3.4 was used for the additional assessment of the IS and ISC products. **Figure 3-8** shows the scatter plots between reference data and predicted IS for 2000 and 2010. I assigned colors to the scatterplot using numbers of points for each 10% by 10% grid. The RMSE of the IS 2000 is 15.4%, while the RMSE of IS 2010 is 19.7%. **Figure 3-9** shows the scatter plots between reference and predicted ISC for the ISC result using IS-2000 from the algorithm initialization in Subsection 3.3.2.2, the ISC result after iterative training and prediction (ITP) in Subsection 3.3.2.4, and the final ISC product after applying the threshold of one standard error. **Figure 3-9**a illustrates the magnitude of errors in the ISC when estimating the IS using the same regression tree model for two dates. Without the ITP process, the RMSE of the ISC was higher than the RMSE of the IS for both epochs. After the ITP process, the agreement between reference and predicted ISC improved significantly, which is demonstrated by the increase of R^2 from 0.59 to 0.78 and decrease of RMSE from 25.4% to 20.4% in **Figure 3-9**b. **Figure 3-9**c shows that further improvement of accuracy was obtained by applying the threshold of one standard error. In addition, the bias of ISC was reduced from 20.61% to 8.41% after ITP and postprocessing.

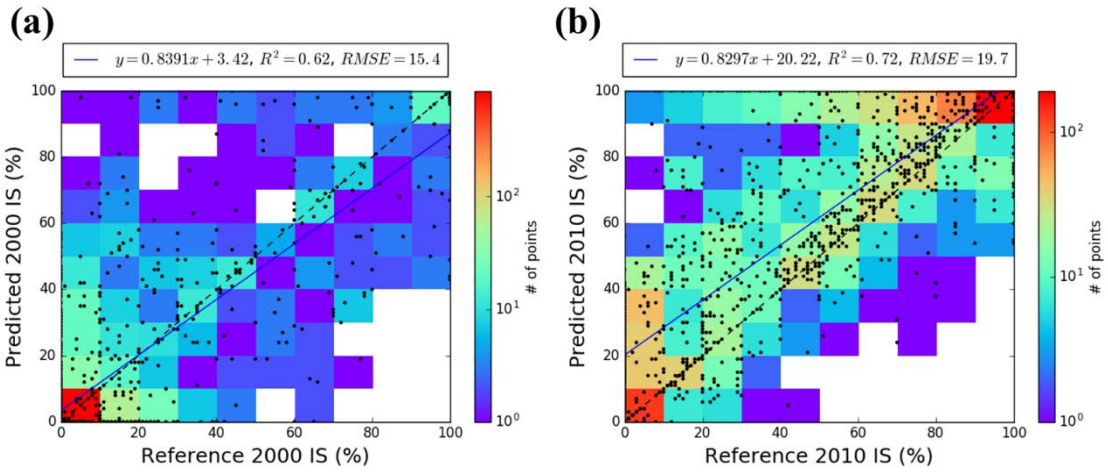

Figure 3-8: Scatterplots of reference vs. predicted impervious surface change (IS) for (a) 2000 and (b) 2010. The number of points for each 10% by 10% grid was used to assign colors to the scatterplot. The blue lines are fitted functions between reference IS (x) and predicted IS (y).

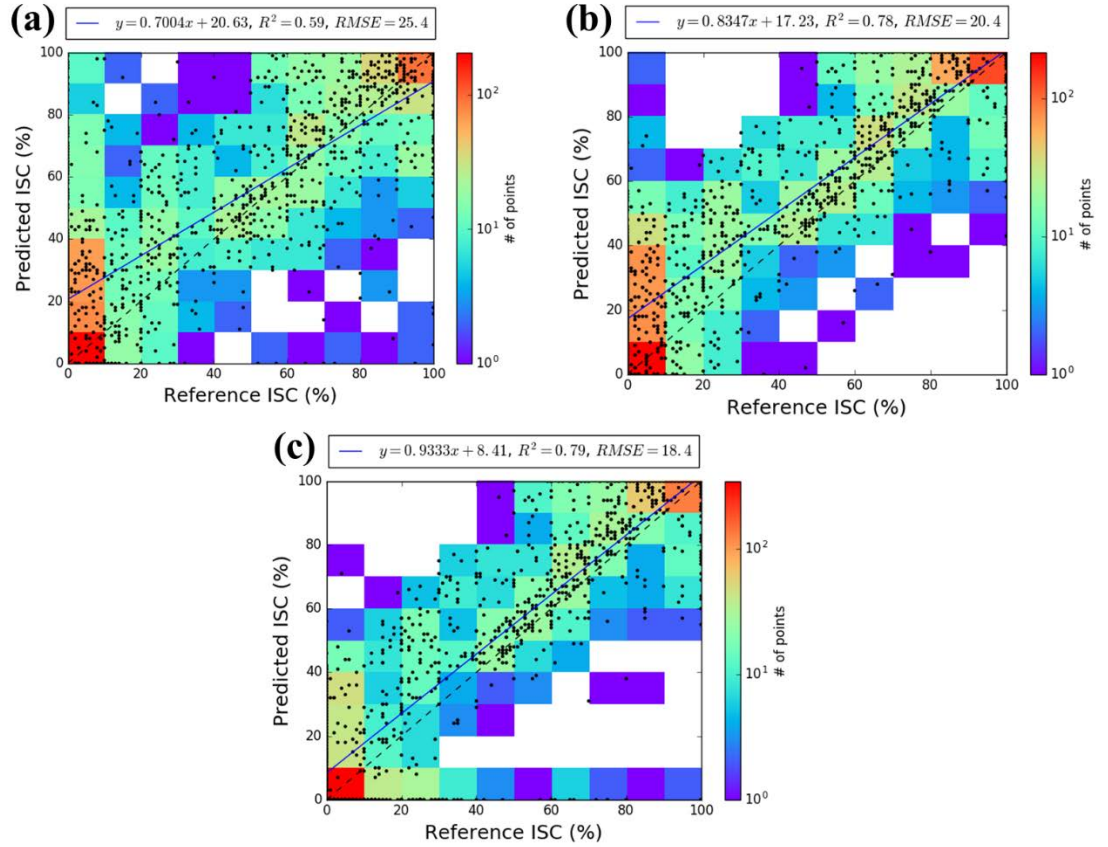

Figure 3-9: Scatterplots of reference vs. predicted impervious surface change (ISC) for (a) the initial result, (b) the result after iterative training and prediction (ITP) and (c) result after ITP and thresholding. The number of points for each 10% by 10% grid was used to assign colors to the scatterplot. The blue lines are fitted functions between reference ISC (x) and predicted ISC (y).

Because a significant portion of the randomly selected reference points could not be used, the statistical distribution of ISC values in the actual dataset is likely to be different from the histogram of the reference ISC, as shown in **Figure 3-4**. To better assess the errors of the ISC product, I estimated the RMSE for each 10% predicted ISC interval using the validation dataset (**Figure 3-10**), which enabled us to establish a lookup table between an ISC prediction and its corresponding RMSE estimation. I used this lookup table to assign a RMSE estimation to each pixel as the approximate standard deviation for the ISC prediction.

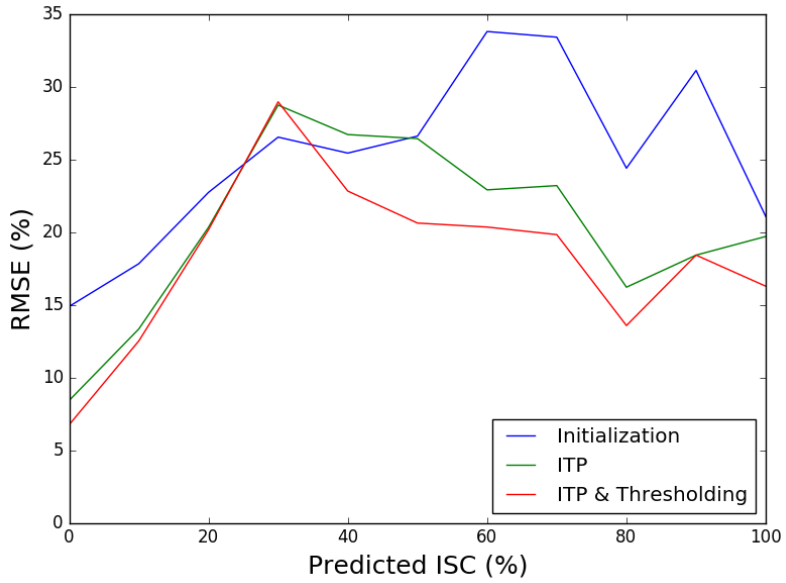

Figure 3-10: Root-mean-square error (RMSE) of the predicted impervious surface change (ISC) for the initial result, result after iterative training and prediction (ITP), and result after ITP and thresholding. The RMSE was estimated for each 10% interval of the predicted ISC.

3.4.3 ISC in India and Relationships between ISC and Socioeconomic Change

In this section, I assess the overall performance of ISC mapping using state-level statistics of the impervious surface change area (ISCA) and its correlation with socioeconomic change. For every state and union territory of India, I calculated the ISCA and its standard deviation (STD) by:

$$ISCA = 0.0009 \times \sum_{i=1}^{N} ISC_i, \tag{3-3}$$

$$\sigma_{ISCA} \approx 0.0009 \times \sqrt{\sum_{i=1}^{N} \sigma_i^2} \approx 0.0009 \times \sqrt{\sum_{i=1}^{N} RMSE_{ISC_i}^2}, \tag{3-4}$$

where ISC_i is the predicted ISC for the $i-th$ pixel; N is the number of pixels within the state boundary; 0.0009 is the size of a Landsat pixel in km^2; σ_{ISCA} is the standard deviation of ISCA for the state; and σ_i the standard deviation of ISC for the $i-th$ pixel, which is approximated using the estimated RMSE for the ISC under the assumption that there is no spatial autocorrelation in the estimated ISC. The ISCA calculation was based on state boundaries defined by the Global Administrative Areas (GADM) dataset (GADM 2015).

Population growth and economic development are known to be two major drivers of urbanization. To examine the relationship between the mapped ISC and socioeconomic change in India, I calculated state-wise change statistics for the gross state domestic product (GSDP) and population between 2001 and 2011. The GSDP data were produced by the Planning Commission of India (Planning Commission of India 2014) and the population data were retrieved from the India Census 2001 and

2011 (Office of the Registrar General & Census Commissioner of Inida 2011). These statistics are listed in **Table 3-1**. The GSDP and population data for three small union territories (Dadra and Nagar Haveli, Daman and Diu, and Lakshadweep) were not available. In addition, the GADM state boundaries list Andhra Pradesh and Telangana as two different states, which were separated from the state of Andhra in 2014. At the time when GSDP and population data were collected, these two states were not separated; therefore, we did not calculate the GSDP and population change for them.

I plotted the state-level total ISCA (y-axis) against the (a) gross state domestic product (GSDP) change and (b) population change (x-axis) from **Table 3-1** in **Figure 3-11**. Both the GSDP and population have good correlations with the ISC product, which are indicators of good overall performance of the ISC mapping method.

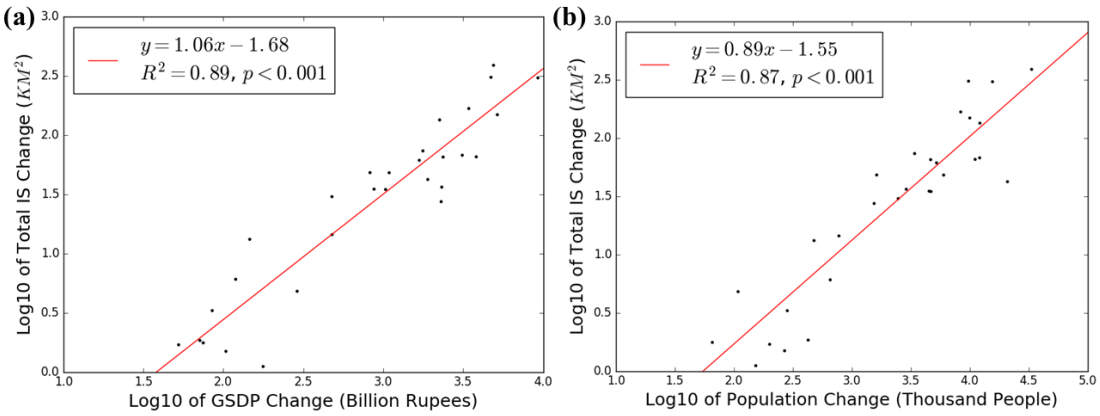

Figure 3-11: Scatterplots between the state-wise total impervious surface (IS) change area (y-axis) and (a) gross state domestic product (GSDP) change and (b) population change (x-axis).

Table 3-1: Statistics of the gross state domestic product (GSDP) change (billion rupees), population change (million people), and impervious surface change area (ISCA; km^2) and the standard deviation (STD) of the ISCA (km^2).

State/Union Territory	GSDP Change	Population Change	ISCA	STD
Andaman and Nicobar	36.64	0.02	0.77	0.18
Andhra Pradesh	N/A	N/A	55.32	0.81
Arunachal Pradesh	85.15	0.28	3.29	0.58
Assam	875.07	4.53	34.97	0.57
Bihar	1896.61	20.93	42.17	0.62
Chandigarh	177.21	0.15	1.11	0.02
Chhattisgarh	1033.33	4.71	34.71	0.75
Dadra and Nagar Haveli	N/A	N/A	2.80	0.05
Daman and Diu	N/A	N/A	1.09	0.02
Goa	289.28	0.11	4.79	0.12
Gujarat	4709.9	9.79	307.72	0.88
Haryana	2364.54	4.67	65.23	0.43
Himachal Pradesh	478.09	0.78	14.44	0.48
Jammu and Kashmir	477.2	2.48	30.18	0.66
Jharkhand	1088.22	6.02	48.09	0.57
Karnataka	3423.65	8.40	167.59	0.89
Kerala	2299.82	1.55	27.40	0.39
Lakshadweep	N/A	N/A	0.02	0.01
Madhya Pradesh	2249.25	12.21	134.25	1.13
Maharashtra	9263.6	15.62	304.42	1.23
Manipur	71.35	0.43	1.84	0.30
Meghalaya	119.34	0.66	6.05	0.30
Mizoram	52.51	0.20	1.69	0.29
Nagaland	92.31	-0.01	4.97	0.26
NCT of Delhi	2319.3	2.90	36.37	0.08
Odisha	1678.27	5.24	61.23	0.80
Puducherry	103.71	0.27	1.49	0.05
Punjab	1768.19	3.42	73.52	0.46
Rajasthan	3116.51	12.15	67.60	1.18
Sikkim	74.8	0.07	1.76	0.17
Tamil Nadu	5164.51	10.03	148.64	0.73
Telangana	N/A	N/A	73.43	0.69
Tripura	146.12	0.48	13.17	0.21
Uttar Pradesh	4887.38	33.53	388.78	1.09
Uttarakhand	825.52	1.63	48.18	0.47
West Bengal	3810.65	11.13	65.56	0.59
Total India	62939.65	181.99	2274.62	3.92

3.5 Discussion

The proposed approach for ISC mapping is designed to solve the fundamental problem of estimating the ISC from bi-temporal images using spectral information, which is the sensitivity of estimated IS to spectral and phenological differences between bi-temporal images. Instead of applying an existing year-2010 regression tree to GLS-2000 images, we designed an ITP process to automatically generate training data for a year-2000 regression tree model, estimated IS-2000, and mapped ISC as the difference between IS-2010 and IS-2000.

Based on visual assessments, quantitative assessments using an independent validation dataset, and the correlation between ISC and changes in population and GDP, the ISC mapping algorithm achieved a low level of error. However, the final ISC products still show a bias towards overestimation as a result of an underestimated 2000 IS (see **Figure 3-8**a) and overestimated 2010 IS (see **Figure 3-8**b). Several methodological limitations and sources of errors remain to be better addressed in future studies.

First, the generation of the NC mask and training datasets for 2000 relies on HBASE masks. If an impervious pixel is classified as non-HBASE for both 2000 and 2010, it might be included in the 2000 training as 0% impervious. The inclusion of such pixels in 2000 training could lead to an underestimation of IS-2000 and therefore overestimation of ISC. To better identify pixels without ISC, unsupervised change detection methods and spectral mixture analysis may yield better results than the heuristic method used in this study (Sexton et al. 2015).

Second, regression trees are known to have a tendency to over-estimate IS for non-impervious areas spectrally similar to IS (Lu et al. 2014; Yuan et al. 2008). I used HBASE masks to remove retrievals of IS in these areas. Yet, there are commission errors in the HBASE masks, as shown in **Figure 3-6**a, where the ISC might be overestimated. In addition, HBASE masks have omissions in low- to medium-density villages/towns, where the ISC might be underestimated. These issues highlight the importance of an accurate HBASE/urban mask for ISC estimation. Other currently available global urban maps may be used in addition to or as an alternative to the HBASE product used in this study. These maps include the GlobeLand30 product (30 m;(Chen et al. 2015b), MODIS Land Cover product (500 m; (Friedl et al. 2010; Schneider et al. 2010), and map from the Global Rural Urban Mapping Project (GRUMP; (CIESIN (Center for International Earth Science Information Network) 2011). More studies on better representation of HBASE/urban in global maps could lead to better estimations of the ISC within the presented framework.

Third, by applying the threshold of one standard error to ISC predictions, I reduced the overestimation of the ISC in areas in which the IS was overestimated. The RMSE of the final ISC product is lower than the RMSE of 2000 IS or 2010 IS. However, this also led to the omission of the real ISC in areas in which the uncertainty of the Cubist™ prediction was high. Bias correction methods, as described in (Huang et al. 2014), might be a better way to remove bias when a high-quality reference dataset is available.

Finally, the ITP process requires many iterations to generate a stable NC mask and corresponding IS-2000. During the processing of the 195 Landsat scenes covering

India, 152 scenes (78%) required more than 100 iterations to converge to a final product. More studies are also needed to improve the computational efficiency of the proposed algorithm for large-scale applications.

Addressing the problems mentioned above requires major methodological improvements. On the other hand, Landsat time series have been demonstrated to be able to deal with ISC errors associated with spectral and phenological differences in bi-temporal datasets (Song et al. 2016). Given the increasing availability of 30 m or finer-resolution satellite datasets, including those acquired by Landsat 8 and Sentinel-2, ISC mapping using dense time series Landsat-like data could be performed at large scales in the near future.

Nevertheless, the proposed method shows great potential for large-scale ISC mapping. It could be particularly useful when mapping the change between a recent date with good coverage of a high-resolution image and a much earlier date when high-resolution data was scarce.

3.6 Conclusion

An ITP approach was developed for mapping the ISC for all of India. The 2010 IS was mapped using a well-established regression tree-based method. Without additional training data collected for the 2000 epoch, the 2000 IS was mapped by automatically generated 2000 training data based on an NC mask. The estimated 2000 IS was in turn used to generate a better NC mask in an iterative fashion.

The ITP method was applied to GLS Landsat images to produce a 2000–2010 ISC product for India. This product had a RMSE of 18.4% and a bias of 8.41% when evaluated using a validation dataset derived from Google Earth™ images. By

calculating the RMSE for every 10% interval of the predicted ISC, I also found that the RMSEs for all predicted ISC intervals were within the 5%–30% range. The performance of the ITP method was further validated by the high correlation between the mapped ISC and socioeconomic changes. Based on statistical analyses of the mapped ISC, I estimated that, if there is no spatial autocorrelation in the estimated ISC, at 95% confidence, the total ISC for India between 2000 and 2010 is 2274.62 ± 7.84 km^2.

It has been demonstrated that the ITP approach is effective for consistently mapping the ISC at national scales with a dataset that exhibited spectral differences between two dates. Such spectral differences may be attributed to differences in acquisition dates, illumination and viewing geometry, and vegetation phenology. With the ability to handle spectral inconsistency, the ITP approach may have a potential for global-scale impervious surface change mapping even when Landsat time series data is not available, leading to fully automated long-term urbanization monitoring and urbanization record from the multi-decadal Landsat historic archive. The implications of this capability are enormous, including the modeling of urbanization induced climate and environmental change, projecting of future urban growth rate and pattern, and making policies to limit unsustainable urban growth.

Chapter 4: Characterizing Urban Structure using the Synergy of Landsat and Global Elevation Datasets: A Case Study of England

4.1 Introduction

Recently, within the urban remote sensing community, a growing amount of interest has shifted from two-dimensional (2D) properties of urban landscape to the vertical dimension (Frolking et al. 2013; Gamba et al. 2000; Geiss et al. 2015; Gong et al. 2011). Indeed, the three-dimensional (3D) structure of an urban area are closely linked to the spatial distribution of its population and human activities as well as its physical properties (Gong et al. 2011; Masson 2006; Souch and Grimmond 2006). Therefore, without proper characterization of urbanization in the 3D space, it is impossible to fully understand the functions and mechanisms of the urban system, its interactions with the environment, and the opportunities and challenges it will present to humanity. A reliable, spatially detailed, updatable, and consistent-across-scales database of urban structural information is needed for key applications such as disaster vulnerability assessment (Geiß et al. 2016) and population distribution mapping (Lu et al. 2011; Qiu et al. 2010). Structural information is also vital to answering many open questions in urban science, from finding the most efficient and sustainable urban layout to optimizing the urban structure to understand local climatic impacts of urbanization (e.g., the urban heat island effect, changes in urban effects precipitation patterns) (Arnfield 2003; Masson 2006; Seto and Christensen 2013; Souch and Grimmond 2006). Earth

observation, empowered by its far-reaching capabilities across spatial and temporal scales, represents the best opportunity to fulfill this need.

To date, studies based on light detection and ranging (Lidar) technology have dominated the literature on urban three-dimensional structures (Cheng et al. 2011; Gong et al. 2011; Gonzalez-Aguilera et al. 2013; Zheng and Weng 2015). Optical image stereography (Sirmacek et al. 2012; Wurm et al. 2014) and synthetic aperture radar interferometry (InSAR; (Gamba et al. 2000; Thiele et al. 2010) have also been proven to be effective technologies to map urban structural parameters such as building height and volume. While Lidar provides an unmatched vertical accuracy, its applications are often limited by incomplete spatial coverage due to its sampling nature. Although to a lesser extent, spatial limitations also apply to high-resolution stereo optical images and sometimes also InSAR images (Lu et al. 2007; Wurm et al. 2014). Besides, there are two additional major technical challenges of urban 3D structure mapping, even for areas with satisfactory data coverage. First, all three technological approaches typically measure the height of buildings on top of bare ground, that is, digital surface models (DSMs). To extract the building height and volume, either direct approaches that separate the ground and top of building signals or indirect approaches that remove the ground height from DSM products have been adopted (Gamba et al. 2000; Geiss et al. 2015; Meng et al. 2010). Second, buildings are not the only vertical structures on the ground surface. Trees, for example, must be removed from height measurements for urban applications. To address this issue, there are also direct and indirect approaches (Gamba et al. 2000; Zheng and Weng 2015). In addition to these direct and indirect approaches, building boundaries derived from classifying optical

images or vector data layers have also been used as ancillary information to address these two technical issue (Thiele et al. 2010; Wegner et al. 2014).

Since the success of the Shuttle Radar Topography Mission (SRTM), several satellite missions have provided global seamless measurements of surface elevation including the DSM dataset from the recent TanDEM-X mission (Krieger et al. 2007; Tachikawa et al. 2011; Tadono et al. 2016; Van Zyl 2001). Some of these global DSM datasets have been made freely available, raising the question if they could be used for large-scale urban structure characterization, a possibility first envisioned by Nghiem et al. (2001).

In this study, the synergy of Landsat data and global elevation datasets is investigated to address technical challenges of urban structure mapping discussed above. The objective of this chapter is to develop methods for mapping building height and volume at 30 m resolution and to demonstrate the effectiveness of the developed method on a large scale. By leveraging the spatial information from Landsat-based segmentation of urban land patches as demonstrated in the previous chapters, this study explores multiple object-based height metrics derived from global DSMs and machine learning estimation of building height/volume from these metrics, which are used to produce 30 m building height and volume products for the entire country of England. To the best of the author's knowledge, this study is the first attempt to produce wall-to-wall maps of the building height/volume at the scale of a country the size of England.

4.2 Study Area and Datasets

The study area of this chapter is the entire country of England, covering 130,279 km^2 of land area and with a population of 53,012,456 people (according to the 2011 census). Based on two land cover maps (LCM) for 2000 and 2015, the total urban area of England is 13,788 km^2 and 14,194 km^2, respectively, representing a 2.94% increase between the two years (Fuller et al. 2002; Rowland et al. 2017). According to the United Nations (United Nations 2015), the average annual rate of population growth for the United Kingdom (UK) is 0.45%, 0.98%, and 0.65% for the time periods 2000–2005, 2005–2010, and 2010–2015, respectively, which is much lower than that of mid-income and low-income countries. From 2000 to 2012, the total business floor space of England moderately increased from 527,058 m^2 to 544,414 m^2, with a growth rate of 3.29% (Valuation Office Agency 2012), compared with a growth of 29.34% of the total commercial floor space in the United States from 1999 to 2012 (U.S. Energy Infromation Administration 2016). Therefore, it was assumed that both the overall growth rate of 2D urban expansion and overall urban growth rate in the vertical dimension were relatively slow during the 1998–2016 period, although much faster urban growth might exist in certain areas including the suburban areas of large metropolises such as London.

The relative slow urban growth of England was an important factor in the selection of the study area. Limited by how frequently data are updated, the datasets used in this study to map the building height/volume and for regression model training/validation were collected over a wide time span between 1998 and 2016, which will be further discussed in the following subsections. This would lead to potential

discrepancies among (a) training/validation data and datasets used for mapping and (b) different datasets used for mapping. Such discrepancies could be greatly reduced by choosing England as the study area. Because year 2010 is approximately the mid-point of the temporal range of the best available datasets, 2010 was picked as the nominal mapping year.

4.2.1 Lidar-based Building Height Dataset

The UK Environment Agency (EA) has been collecting airborne Lidar data since 1998. By 2016, ~75% of England has been mapped at least once with accurate elevation measurements. The 1 m resolution DSM and DTM datasets have been made freely available (UK Environment Agency 2016). As shown in **Figure 4-1**, most of the 1 m Lidar data were acquired during the 2006–2014 period. According to the EA, the absolute height error of the dataset is within ±15 cm, while the relative height error is less than ±5 cm (UK Environment Agency 2016), making it an excellent source of accurate training and validation data for building height/volume estimation.

As described in the introduction, building height mapping with Lidar data requires either accurate auxiliary building boundary information or the automatic separation of buildings and other vertical structures, such as trees. Here, I used an open dataset provided by Emu Analytics (Emu Analytics 2016). Based on the EA Lidar data, the Emu DataPacks used building boundaries from the ordnance survey of Britain to separate buildings and non-buildings. While the quality of this dataset has not been fully assessed, it is expected to be among the highest-quality building height datasets freely available, based on its data source and methodology.

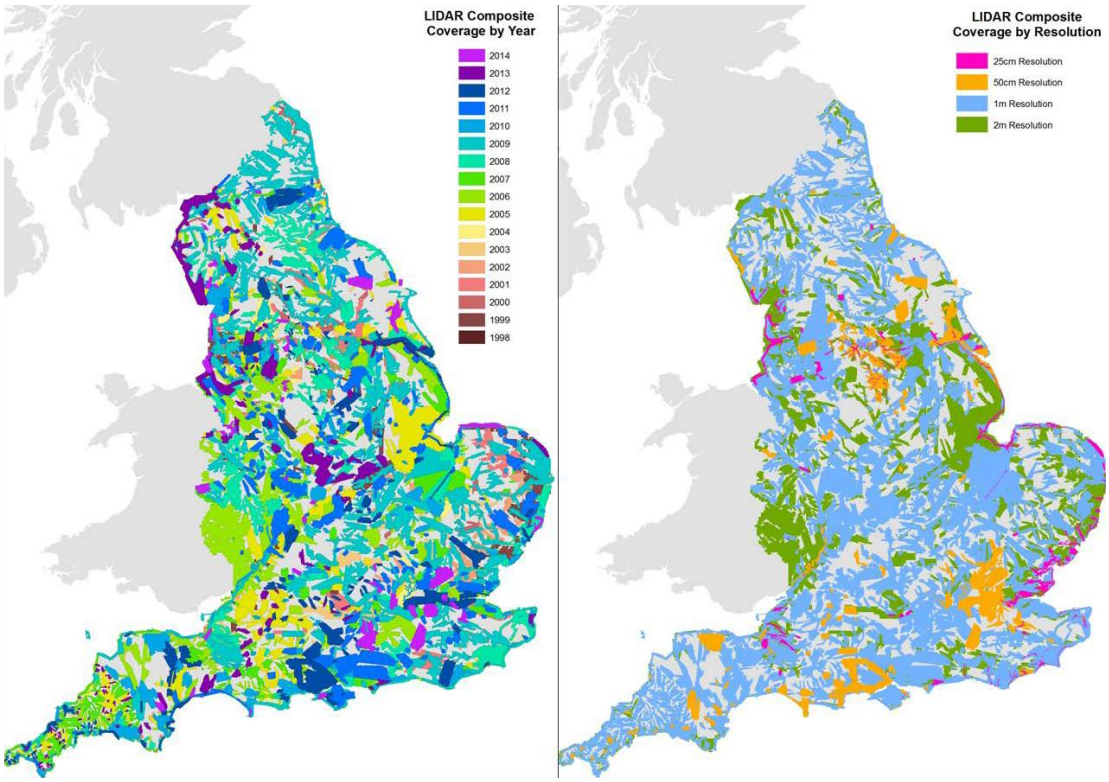

Figure 4-1: England lidar data coverage maps by year and resolution. The maps are provided by (UK Environment Agency 2016).

4.2.2 Global Elevation Datasets

Three global elevation datasets were used in this study including the Shuttle Radar Topography Mission (SRTM), Advanced Spaceborne Thermal Emission and Reflection Radiometer (ASTER) Global Digital Elevation Model (GDEM), and Advanced Land Observing Satellite (ALOS) World 3D–30 m (AW3D30) datasets. **Table 4-1** lists the main characteristics of these datasets. All three datasets are posted at ~ 30 m spatial resolution and provide DSM measurements. Yet, these datasets perform differently in terms of vertical accuracy due to the use of different sensors and technological approaches. Although less well characterized given its recent release date, it is expected that AW3D30 has a better vertical accuracy than the other two datasets

because its data source, the Panchromatic Remote-sensing Instrument for Stereo Mapping (PRISM) sensor, has superior spatial resolution (2.5 m, (Tadono et al. 2016)). This is particularly important for urban applications because most urban features can be best resolved at high spatial resolution. However, as a result of cloud cover and gaps between satellite orbits, AW3D30 has a considerable amount of data gaps in many parts of the world (Tadono et al. 2016). On the other hand, the SRTM and ASTER GDEM have been widely utilized in different applications and assessed in different areas of the world (Mukherjee et al. 2013; Satge et al. 2016; Small and Sohn 2015). Based on selected studies on the accuracy of these two datasets, none of them consistently outperforms the other. The vertical accuracy varies among different terrain types. In urban areas, both the SRTM and ASTER GDEM demonstrate an overestimation of the ground height and underestimation of the building top height (Small and Sohn 2015). However, the ASTER GDEM may have a higher error in urban areas because stereography in heterogeneous urban environments may require higher spatial resolution than what ASTER provides. In summary, there is no clear best choice among these three datasets considering both spatial coverage and vertical accuracy. Therefore, I included all three datasets in the mapping of building height and volume assuming they have complimentary advantages. For further processing, these elevation datasets were projected and resampled using a nearest neighbor resampling technique to match them with Landsat images.

Table 4-1: Characteristics of the global elevation datasets used to map building height/volume.

Name	Collection Year	Resolution	Sensor/ Data Source	Version	Vertical Accuracy (RMSE)
SRTM	2000 (11 days)	1 arc-second (30m)	C/X band InSAR	SRTMGL1 v3	6.6 m (Satge et al. 2016), 5.53 – 12.77 m (Rodriguez et al. 2006), 17.76m (Mukherjee et al. 2013)
ASTER GDEM	2000-2011	1 arc-second (30m)	ASTER stereo imagery	v2	8.68 m (Tachikawa et al. 2011), 9 m (Satge et al. 2016), 12.62 m (Mukherjee et al. 2013)
AW3D30	2006-2011	1 arc-second (30m)	PRISM stereo imagery	v1	4.4 m (Tadono et al. 2016)

4.2.3 Landsat Datasets

Due to extensive cloud cover and the SLC-off gap issue with Landsat 7 ETM+ images in different parts of the study area, I manually selected 24 Landsat 5 and Landsat 8 scenes covering the entire land mass of England instead of using the GLS Landsat dataset. Among them, 16 images were within the 2009–2011 temporal window, 5 were acquired during 2003–2006, and 3 were Landsat 8 images acquired between 2013 and 2014. In the selection of Landsat images, if no SLC-off gap or cloud was present, acquisitions close to the temporal range of DSM datasets (2000-2011) were preferred, because Landsat images need to be overlaid with DSM datasets for height information extraction.

4.3 Methods

4.3.1 Training Data Derivation

Based on the 1m lidar-derived building height, building volume for a 30m pixels was calculated as

$$V = \sum_{i=1}^{N} h_i \times A = A \times \sum_{i=1}^{N} h_i, \quad (4\text{-}1)$$

where $h_1 \sim h_N$ are the above ground height of 1m building pixels within the 30 m pixel and $A = 1m^2$ is the area of a 1 m pixel. Consequently, the average building height for the target 30 m pixel was defined as

$$\bar{h} = \frac{V}{\sum_{i=1}^{N} A} = \frac{1}{N} \sum_{i=1}^{N} h_i. \quad (4\text{-}2)$$

Note that only building pixels within the 30 m pixels were used to calculate the average building height.

4.3.2 Input Features for Machine Learning Algorithms

Using the training data derived above, machine learning regression models based on features derived from Landsat and DSM datasets were trained to predict average building height and volume. A total of 88 feature variables was used as input for the machine learning algorithms. They include pixel-level metrics, which were calculated on a pixel-by-pixel basis, and object-level metrics, which were calculated

based on multi-level Landsat image objects. **Table 4-2** lists all features used by the feature calculation spatial scale and data source. The following subsections describe how these features were calculated in detail.

Table 4-2: List of input features used for machine learning regression models including features derived from AW3D30, GDEM, SRTM, and Landsat-based impervious surface (IS). The right column shows the count of features at different levels.

Level	Features				#
	AW3D30	GDEM	SRTM	IS	
Pixel	Height, slope	Same as AW3D30	Same as AW3D30	IS value	7
Level-1 object	Mean, max, min and STD of height IS-weighted mean of height Mean height for pixel with max IS Mean height for pixel with min IS Object-level average slope	Same as AW3D30	Same as AW3D30	Mean, max, and min of IS value	27
Level-2 object	Same as above				27
Level-3 object	Same as above				27
Stacked	-	-	-	-	88

4.3.2.1 Pixel-level Metrics

The first set of pixel-level metrics used as input features are height values from the three elevation datasets described in Subsection 4.2.2. Conceptually, it is notable that slope is also an important factor to consider. For example, slope information is key

to many morphology-based filters for separating the ground height (DTM) from surface height (DSM) and the filtered results are generally less reliable in areas with steep terrains if the slope information is not properly considered (Geiss et al. 2015; Maguya et al. 2013; Meng et al. 2010; Zhang et al. 2003). Therefore, for each of the DSM datasets used, I also included its slope information using a calculation method proposed by (Horn 1981):

$$S_{i,j}^{x} = [(Z_{i+1,j+1} + 2Z_{i+1,j} + Z_{i+1,j-1}) - (Z_{i-1,j+1} + 2Z_{i-1,j} + Z_{i-1,j-1})]/8\Delta X, \quad (4\text{-}3)$$

$$S_{i,j}^{y} = [(Z_{i+1,j+1} + 2Z_{i,j+1} + Z_{i-1,j+1}) - (Z_{i+1,j-1} + 2Z_{i,j-1} + Z_{i-1,j-1})]/8\Delta Y, \quad (4\text{-}4)$$

$$S_{i,j} = \sqrt{S_{i,j}^{x} \times S_{i,j}^{x} + S_{i,j}^{y} \times S_{i,j}^{y}}, \quad (4\text{-}5)$$

where $S_{i,j}^{x}$ and $S_{i,j}^{y}$ are the slope in the X and Y directions, respectively; $Z_{i,j}$ is the DSM height value for the pixel (i, j); ΔX and ΔY are the distances between pixels in the X and Y directions, respectively (30 m in this case); and $S_{i,j}$ is the estimated slope of the pixel (i, j).

As described in Subsection 3.3.1, the GMIS project produced a 30 m percent IS product. By applying the same Cubist™ regression model to the Landsat images used in this study, the percent IS was produced for the study area. I used this variable as another pixel-level metric to incorporate density information into the modeling of building height/volume.

4.3.2.2 Object-based Height and Imperviousness Metrics

The segmentation of Landsat images at three levels of detail was obtained using the RHSeg software package and a bottom-up merging procedure, as described in Subsections 2.2.1.2 and 2.2.1.3. However, the size thresholds of objects defined in Chapter 2 was not suitable for height and volume mapping. In this chapter, a different set of thresholds, 100, 1000, and 10000, was used for object derivation to better resolve fine-scale height variations within urban areas.

The first group of features calculated at the object level was the mean, maximum, minimum, and standard deviation of the height, which included features derived at all three object levels using all three elevation datasets. The rationale for including these features was that the maximum and minimum of the height are related to the roof-top and ground heights within an object, while the mean and standard deviation describe the general pattern of the height distribution in an object.

The second group of features included the mean, maximum, and minimum IS percentages within the objects. These features were included to help separating areas with different urban densities. On a conceptual level, when deriving the building height from DSM data, different ground and roof-top height estimation strategies should be adopted in areas with different urban densities. For example, for low density urban areas, minimum value of DSM may be a good estimation of ground height, while minimum value of DSM may overestimate ground height in dense urban areas because of the absence of pure ground pixels. Therefore, this 2D urban information is also expected to be useful for the height and volume estimation.

Based on the combination of the IS and height from elevation datasets, I derived the third group of features. First, for an object O containing N pixels, the IS-weighted mean of height was calculated as:

$$\overline{h}_{IS} = \frac{\sum_{i=1}^{N} h_i IS_i}{\sum_{i=1}^{N} IS_i}, \quad (4\text{-}6)$$

where h_i and IS_i were the height value and IS percentage of a pixel within the object, respectively. The rationale for including this feature was to use impervious surface to separate the height of non-building vertical structures such as trees from building height at sub-pixel level. Similarly, two other features were also included:

$$\overline{h}_{ISMIN} = \frac{\sum_{i \in O_0} h_i}{|O_0|}, \quad (4\text{-}7)$$

$$\overline{h}_{ISMAX} = \frac{\sum_{i \in O_1} h_i}{|O_1|}, \quad (4\text{-}8)$$

where O_0 and O_1 were subsets of the object O where impervious surface percentages of pixels were minimum and maximum within the object, respectively.

Finally, for an object O containing N pixels, average slope was estimated by calculating the average of slope in the X and Y directions first:

$$S_O^x = \frac{1}{N} \sum_{(i,j) \in O} S_{i,j}^x, \tag{4-9}$$

$$S_O^y = \frac{1}{N} \sum_{(i,j) \in O} S_{i,j}^y, \tag{4-10}$$

$$S_O = \sqrt{(S_O^x)^2 + (S_O^y)^2}. \tag{4-11}$$

4.3.4 Machine Learning Regression Experiments

Using the features derived in Subsection 4.3.2 and the Lidar-based training data, I tested different machine learning regression techniques to estimate the building height and volume. Note that although most of the features were derived at the object level, the machine learning modeling and prediction was performed at the pixel level because pixel-level features were also used. Moreover, using the urban extent map developed in Chapter 2, all non-HBASE pixels were excluded from the prediction of the building height and volume. Finally, because this study focuses on the buildings and their height/volume, major roads pixels included from the OpenStreetMap vector layer into the HBASE products were also excluded.

Two sets of experiments were designed to test (1) the usefulness of input features derived from different elevation datasets, and (2) the efficacy of different machine learning algorithms in predicting the building height and volume. For the first group of experiments, I performed random forest (RF) regression of the building height based on features derived from AW3D30, GDEM, SRTM only, and a combination of all features. The IS-based features were used in all four tests. For the second experiment, two most widely used regression algorithms in remote sensing, RF (Breiman 2001) and

Cubist™ (Rulequest Research 2016), were selected for the height and volume estimation. The results of these two experiments were used as a basis for the selection of the feature set and learning algorithm used to produce the final height and volume products.

4.3.5 Validation of Estimated Height/Volume

The validation of building height and volume measurements is difficult. In the case of this study, the Lidar-based training data are the most accurate source of references available. Therefore, to interpret the machine learning experiments designed in Subsection 4.3.4., 10-fold cross-validation was adopted, which was also used to validate the final height and volume product. Following an approach similar to the scene-level cross-validation (SLCV) used in Subsection 2.2.4.1, the partition of training data into blocks was performed based on the scene they belong to. The rationale for this approach is to avoid inflated accuracy estimates produced by spatial autocorrelation between training and testing samples when spatially adjacent pixels are divided into training and testing samples in each fold of cross-validation (Friedl et al. 1999). Using SLCV, cross-validation accuracy estimates were produced, including the root-mean-square error (RMSE) and correlation coefficient (R^2). These accuracy estimates, as explained above, should be considered as reasonably unbiased because spatial autocorrelations between training and testing samples have been minimized by the SLCV approach.

Additional validation was done based on correlation between the estimated building volume and socioeconomic variables. I used here a dataset containing series of socioeconomic variables (e.g., population, GDP, and CO_2 emission) for 12

metropolitan areas defined by the Organization for Economic Co-operation and Development (OECD; (Brezzi 2012)). Regression analyses were performed between these variables and estimated building volume. Because these variables have been found to be correlated with building volume (Cheng et al. 2011; Qiu et al. 2010; Resch et al. 2016), strong correlations with these variables are indicators of the performance of the building volume mapping method.

4.4 Results

4.4.1 Comparison of Input Features Based on Different Elevation Datasets

The comparisons of the effectiveness of different features focused on the height estimation accuracy using RF. Surprisingly, AW3D30 produced the worst result in terms of both R^2 and RMSE (**Figure 4-2**). As expected, the SRTM-based result was slightly better than the result using GDEM, while the best result was achieved using input features derived from all three elevation datasets together. These results confirmed the hypothesis mentioned in Subsection 4.2.2 that these elevation datasets complement each other. Thus, the final height and volume maps will be produced using the combination of all features.

The relatively higher RMSE (1.86 m) of the height estimation using AW3D30 compared to using ASTER GDEM (1.79 m) and SRTM (1.76 m) contradicts the fact that the AW3D30 is expected to have a higher vertical accuracy, particularly in urban areas. This is may be driven by the relatively high amount of data gaps in the AW3D30 product. **Figure 4-3** shows that a large portion of the study area lacks data or has low-reliability data. In these areas, the error of the estimated height was clearly higher than

in areas with valid AW3D30 data, as shown by the zoom-in views of **Figure 4-3**, where a boundary is present between East and West London in terms of overall error, which coincided with the boundary of missing data.

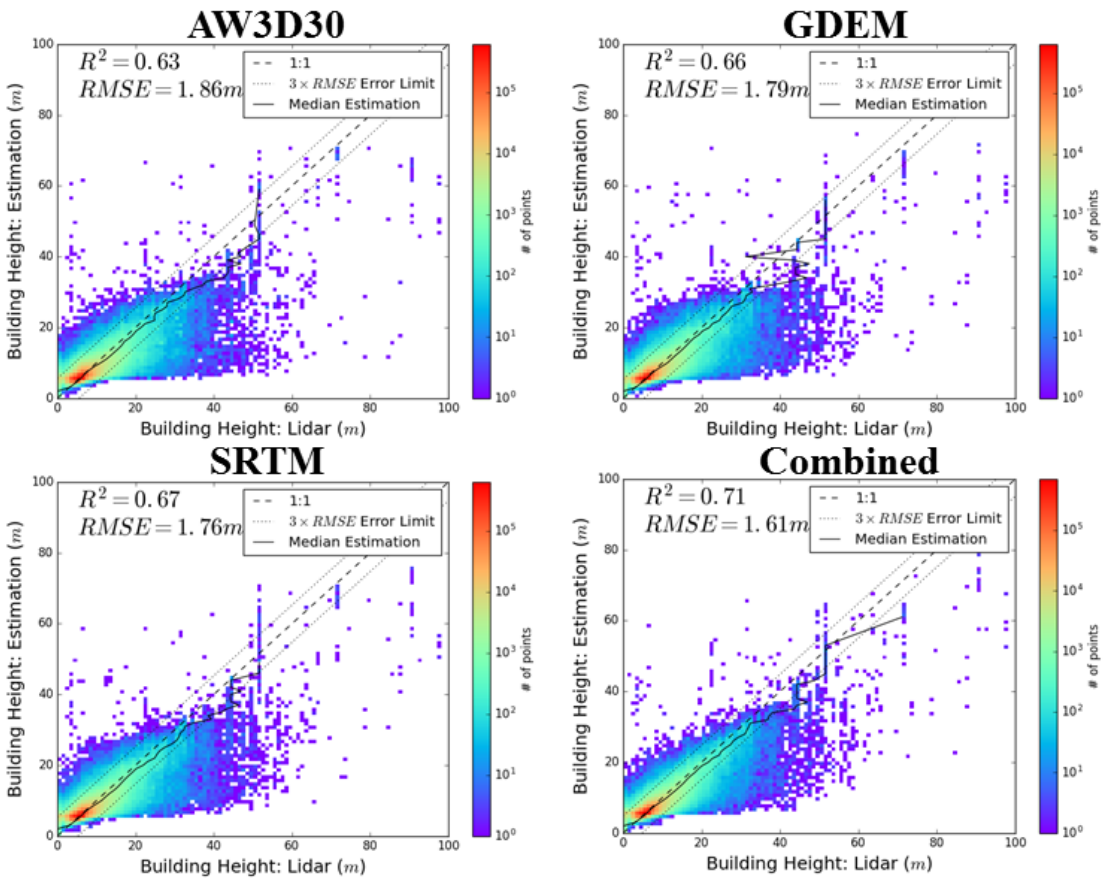

Figure 4-2: Scatterplot-based comparison of the accuracies of the building height using random forest and input features from different elevation datasets. The points in the scatterplots were derived from the 10-fold cross-validation.

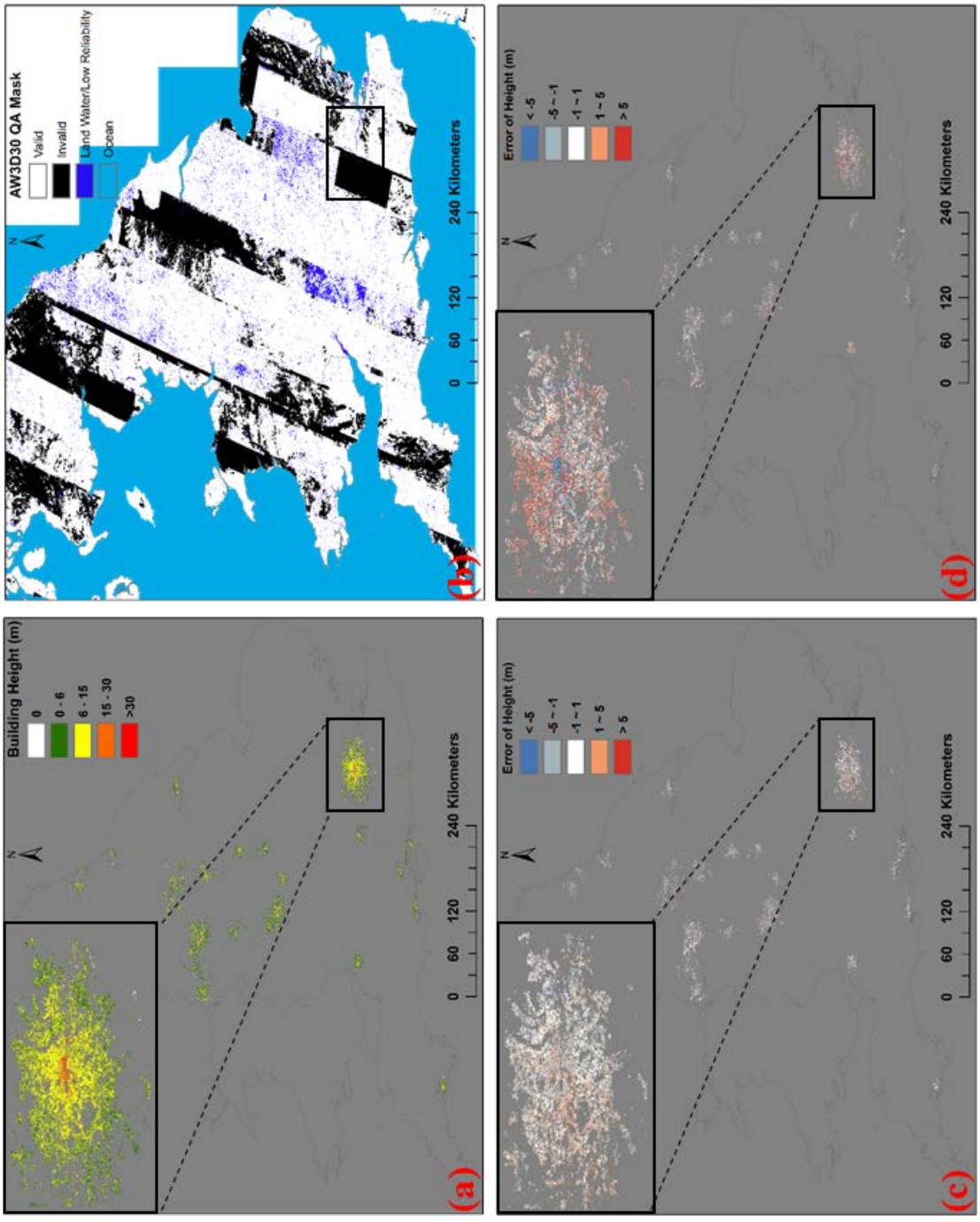

Figure 4-3: The spatial distribution of (a) Lidar-based training data, (b) quality flag of the AW3D30 elevation dataset, where black and blue mark no-data- and low data-reliability areas, respectively, (c) error of height estimation using random forest, and (d) error of height estimation using the Cubist™ regression tree. The zoom-in window shows the distributions for the city of London.

4.4.2 Comparison of Results using Random Forest and Cubist™

Based on the comparison of the spatial distribution of errors of RF and Cubist™, as shown in **Figure 4-3**, it is clear that missing data plays an important role because different missing data handling methods were employed by these two machine learning algorithms. When height predictions were made over pixels containing features with missing data, RF tried to make predictions based on regression trees that do not involve the missing features, while Cubist™ replaced the missing values with average values (derived from the entire training data) for each feature, which is a statistical technique known as imputation. The imputation-based method is clearly problematic in this case because the final prediction might be made based on the imputed values. Therefore, the Cubist™ results exhibited more contrast between areas with and without valid AW3D30 data. To further investigate how missing data affected the performance of the height estimation, I examined the histograms of the error for pixels with valid AW3D30 data, invalid AW3D30 data, and all pixels (**Figure 4-4**). When valid AW3D30 data were available, the height estimation error was consistently lower than that of the pixels with invalid AW3D30 data and all pixels. In fact, the error histograms for all pixels fall in the middle of the other two, suggesting that AW3D30 would generate the best results among the three elevation datasets if much less data gaps were present in the study area. Again, Cubist™ appeared to be more affected by missing data.

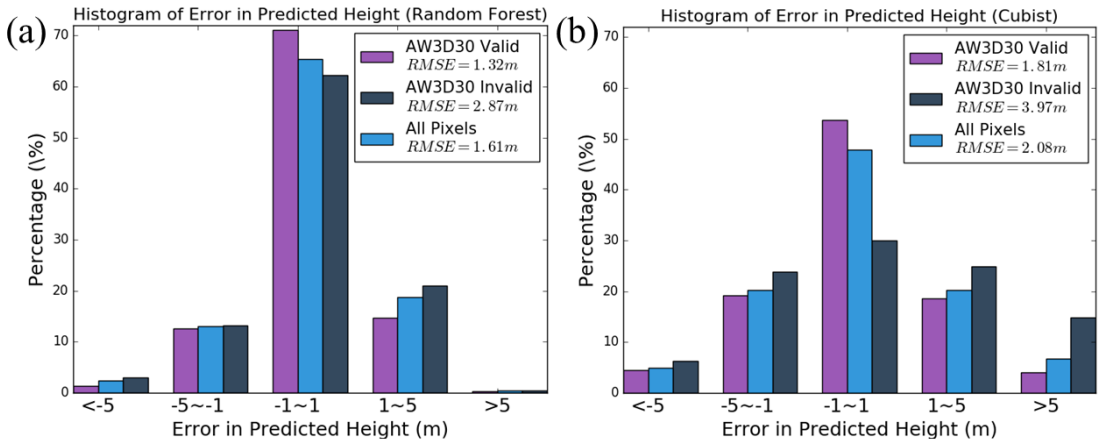

Figure 4-4: The histogram of error in predicted height using (a) random forest and (b) Cubist™ regression tree. The histograms for three groups of pixels where AW3D30 data is valid, invalid, and all pixels are plotted using different colors.

Judging from the results from the cross-validation approach described in Subsection 4.3.5, RF clearly outperformed the Cubist™ regression tree in estimating both the building height and volume (Figure 4-5). Using RF, a RMSE of 1.61 m was achieved for the building height estimation, which is 22% lower than that of the Cubist™ regression tree. And an RMSE of 1142 m^3 was achieved for the building volume estimated by RF, 24% lower than that of the Cubist™ regression tree. Based on these results, RF was chosen to produce the final height and volume maps.

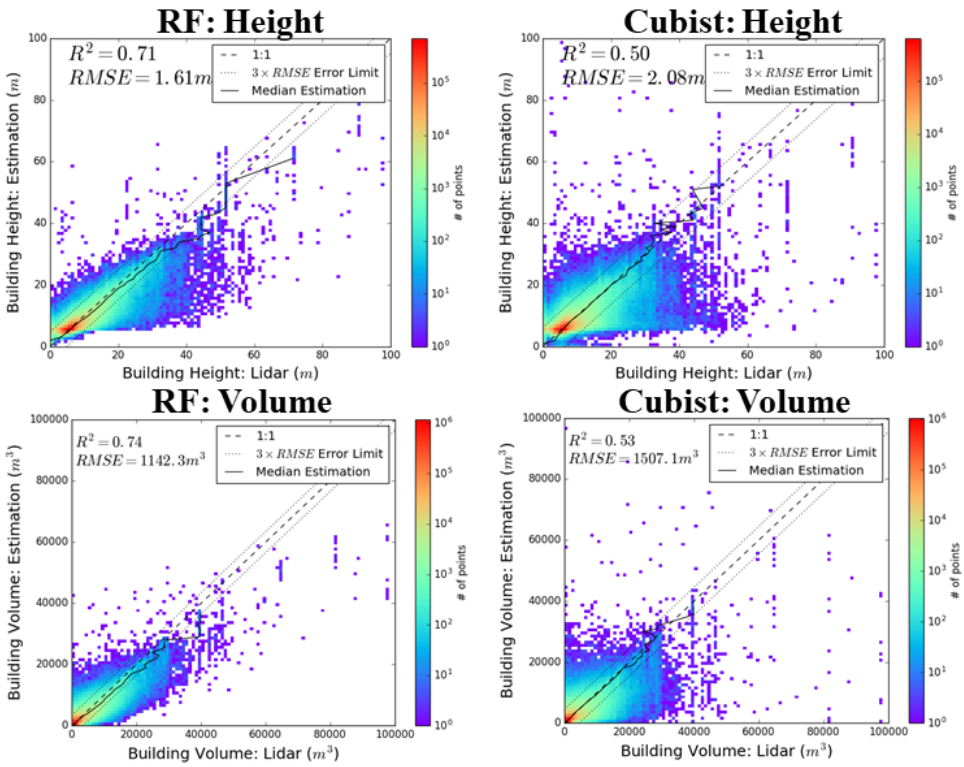

Figure 4-5: Scatterplot-based comparison of the accuracies of height and volume estimation using random forest (RF) and Cubist™ regression tree. The points in the scatterplots were derived from the 10-fold cross-validation.

4.4.3 Characteristics of the Mapped Building Height and Volume

The final building height and volume maps were produced using the combination of features derived from all elevation datasets and the RF regression algorithm. As shown in **Figure 4-6**, the overall distribution of the mapped average building height and volume exhibit a strong pattern of agglomeration. Many of the main urbanized areas in England were mapped with less than 6m of average building height and less than 1,500 m^3 of building volume. For the bulk of greater London and the core areas of several large cities (e.g., Birmingham and Manchester), however, the mapped building height was approximately 6 to 15 m and the building volume was 1500 to 3000 m^3. Finally, average building heights higher than 30 m were found mostly

distributed in the core area of the city of London and a few hub cities including Birmingham and Manchester.

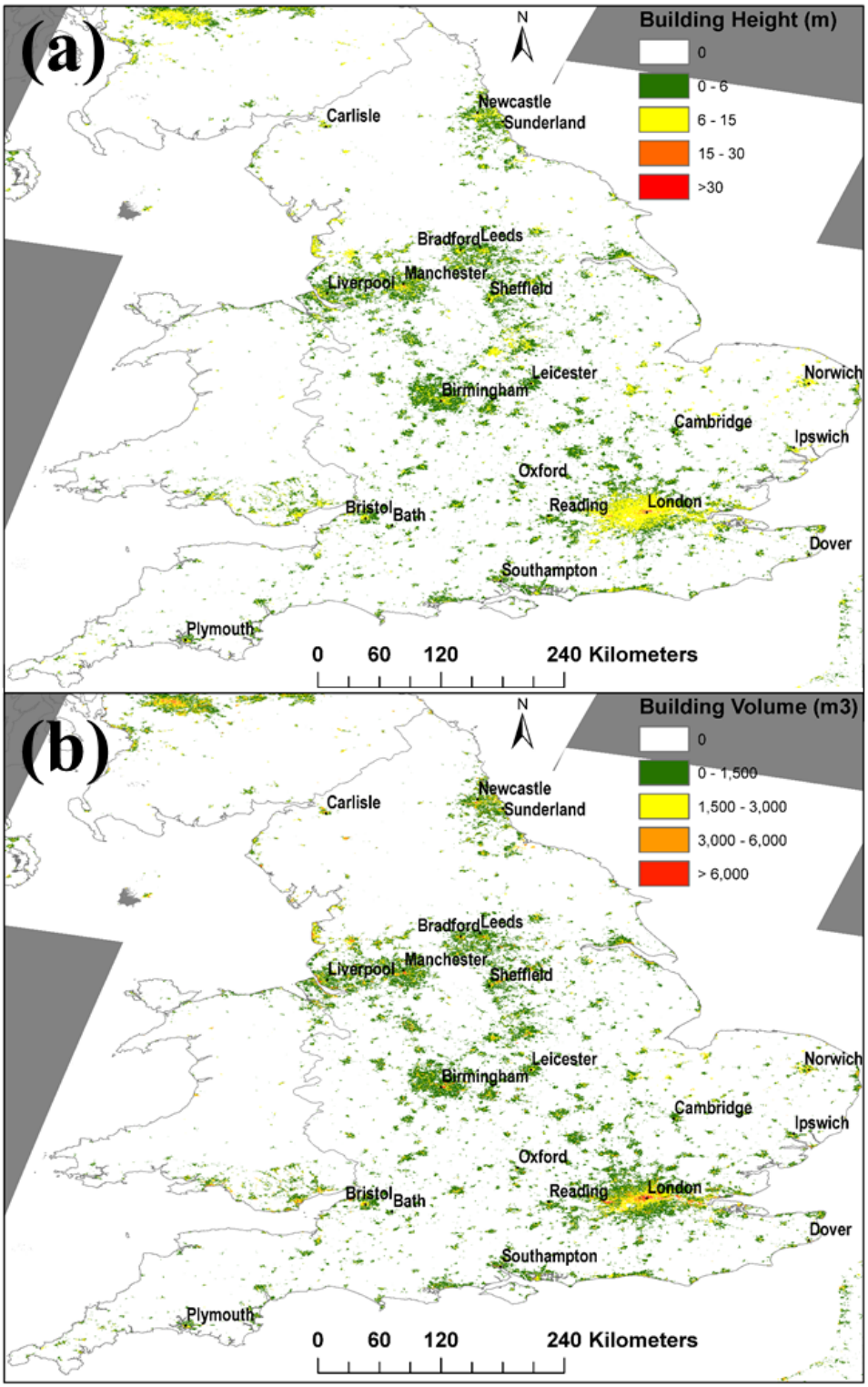

Figure 4-6: Final product of (a) building height and (b) building volume for England.

More detailed maps and side-by-side comparisons with Lidar data for the city of London and Leicester are shown in **Figure 4-7** and **Figure 4-8**. The predicted height and volume match the spatial patterns of Lidar data very well. However, the prediction errors tended to be higher in urban centers because the elevation datasets used do not have a sufficient spatial resolution to effectively map the complex height variations in the urban centers.

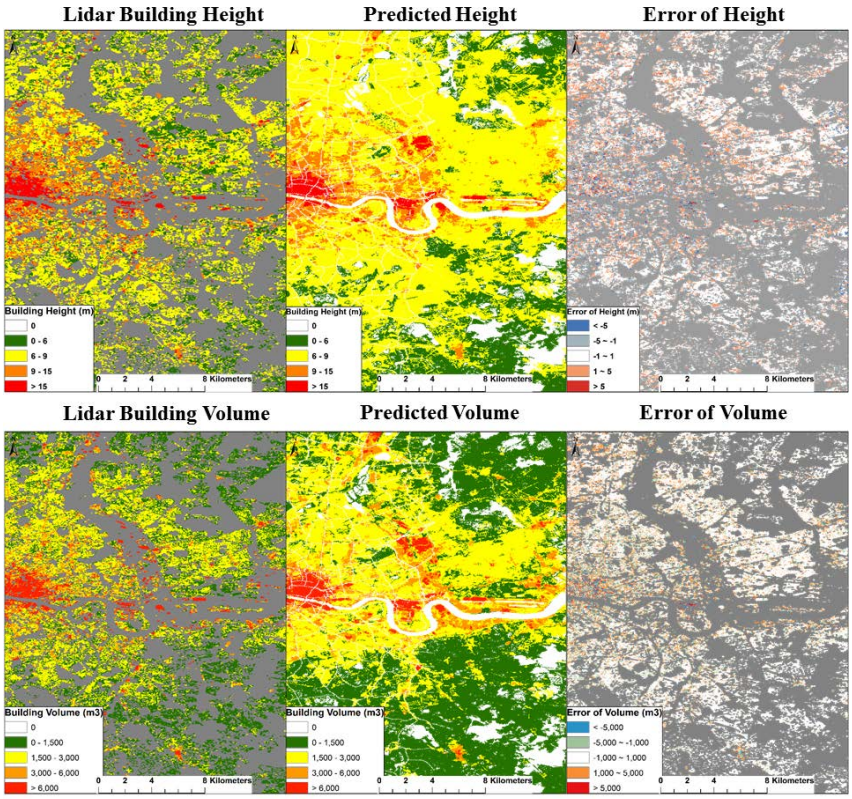

Figure 4-7: Mapped building height and volume for the city of London, in comparison with lidar derived reference data (gray areas do not have lidar coverage). The error of height and volume are derived from the difference between random forest predictions and lidar reference data.

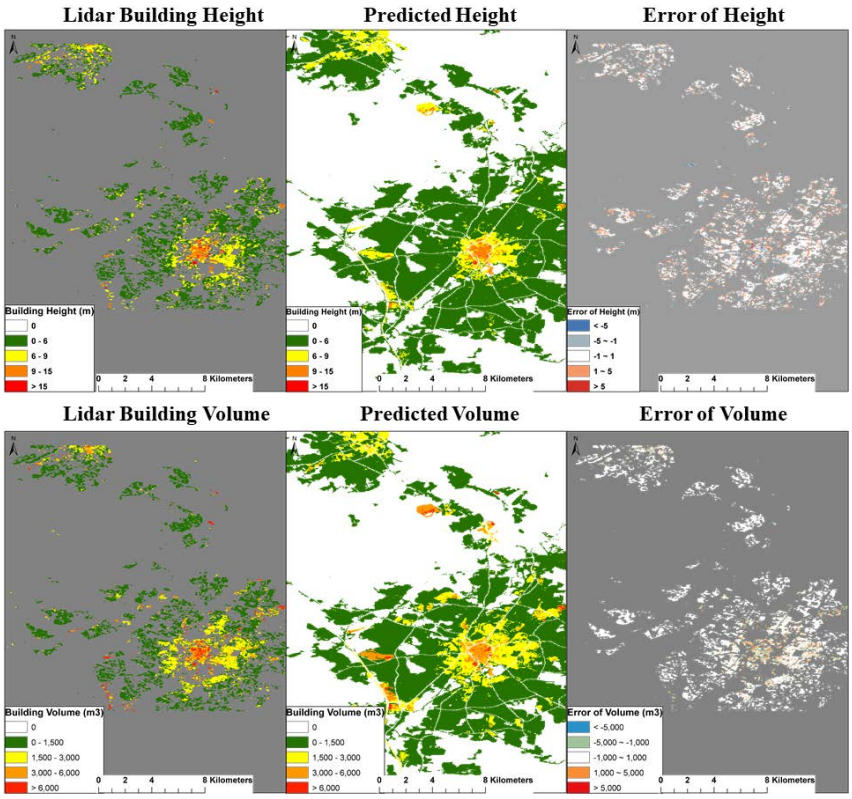

Figure 4-8: Mapped building height and volume for the city of Leicester, in comparison with lidar derived reference data (gray areas do not have lidar coverage). The error of height and volume are derived from the difference between random forest predictions and lidar reference data.

4.4.3 Correlation between Building Volume and Socioeconomic Variables

To assess the overall quality of the mapped building volume in terms of correlation with socioeconomic variables, statistical analyses were performed for 12 metropolitan areas defined by the Organization for Economic Co-operation and Development (OECD; (Brezzi 2012). **Table 4-3** lists the total building volume and IS area of these metropolises, alongside population, gross domestic product (GDP), and transportation CO_2 emission data from the OECD metropolitan database. Population and GDP are two important socioeconomic variables for urban areas that have been associated with built-up area and building volume (Avelar et al. 2009; Council 1998; Lu et al. 2010; Lu et al. 2011). The CO_2 emission data were used here as a proxy of

energy consumption from the transportation sector, assuming a uniform emission efficiency across the whole country. I did not include the emission from other sectors, which might be more impacted by other exogenous factors such as local climate (Baiocchi et al. 2015). As shown in **Figure 4-9**, the correlation coefficients (R^2) between total building volume and population, GDP, and transportation CO_2 emission was 0.88, 0.78, and 0.81, respectively. In addition to the strong correlations building volume and socioeconomic variables, the building volume explained the variance of population, GDP, and CO_2 emission slightly better than IS. Note that all fitted lines and R^2 were derived with greater London excluded, which is an outlier because it is one order of magnitude larger than other cities. These results provide not only evidence for the accuracy of the building volume mapping method but also evidence for the usefulness of the mapping building volume in socioeconomic studies.

Table 4-3: Total building volume and impervious surface area of 12 metropolitan areas in England defined by OECD. Population, GDP, and CO_2 emission data are from the OECD metropolitan database are also listed (Brezzi 2012).

Name	Population	GDP (billion US $)	CO_2 Emission (million tons)	Building Volume (km^3)	Impervious Surface (km^2)
London	11,793,530	616.07	28.89	4.30	986.80
Birmingham	1,884,199	59.46	5.63	0.64	208.78
Manchester	1,841,382	68.67	4.66	0.61	194.49
Leeds	1,166,267	42.64	2.37	0.49	167.63
Newcastle	1,050,561	28.33	2.23	0.51	145.25
Liverpool	929,014	30.43	1.52	0.39	109.64
Sheffield	880,237	24.54	1.51	0.30	100.77
Nottingham	835,625	25.92	1.66	0.31	102.18
Bristol	795,481	34.53	1.12	0.31	80.05
Leicester	660,817	20.45	1.14	0.19	70.27
Portsmouth	577,191	22.66	0.60	0.18	56.17
Bradford	540,172	13.87	0.76	0.15	50.29

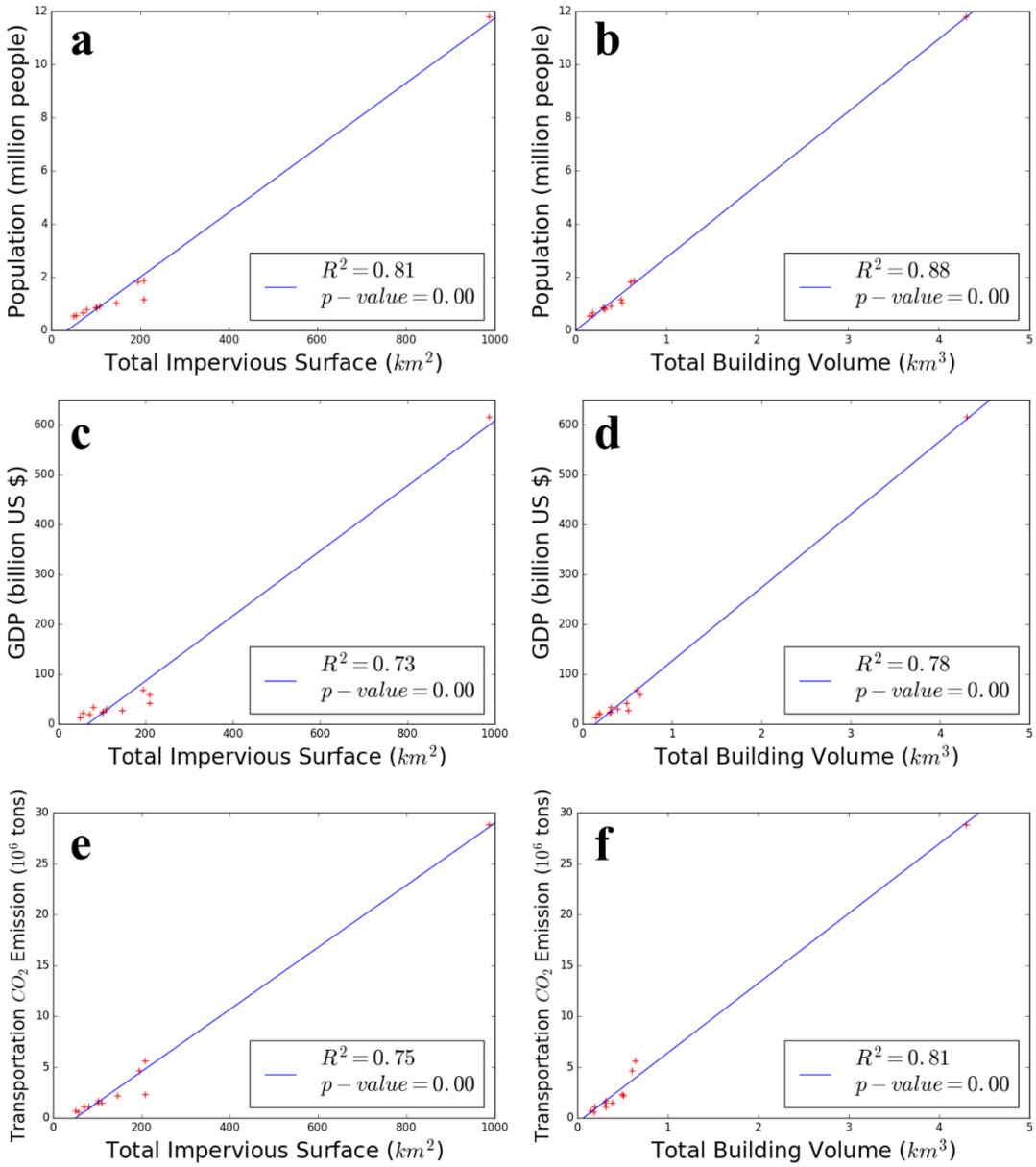

Figure 4-9: The scatterplots between (a) total impervious surface and population, (b) total building volume and population, (c) total impervious surface and GDP, (d) total building volume and GDP, (e) total impervious surface and CO_2 emission, and (f) total building volume and transportation CO_2 emission. Each point represents a metropolitan area defined by the OECD. Note that all fitted lines and correlation coefficients (R^2) were derived with greater London excluded, which is an outlier because it is one order of magnitude larger than other cities.

4.5 Discussion

The machine learning regression experiments clearly demonstrate that global DSM datasets have the potential to characterize large-scale urban structures. However, several limitations exist in this study and should be addressed in future studies.

One of the limitations is the discrepancy between the acquisition periods of the Landsat, DSM, and Lidar data. Major contributing factors that led to this discrepancy include data availability and cloud cover. This has been partially addressed by choosing England as the study area. The relatively slow change in England enabled this study to accurately map the building height and volume using data from a much broader temporal range. However, for other fast-changing regions in the world, temporal discrepancy is a much greater issue, which can only be solved if more recent elevation datasets, such as TanDEM-X DEM, become available.

Another limitation of this study is the relative high error in urban center areas as a result of insufficient spatial resolution to resolve complex height variations in such areas. Again, this is, to a large degree, a data availability issue. Higher resolution DSM data, such as TanDEM-X, are promising for more accurate height measurements in dense urban areas (Geiss et al. 2015; Gruber et al. 2012; Rossi et al. 2011). However, more studies are needed to determine their suitability for large-area applications.

The limitations of the HOTex approach in mapping the urban extent discussed in chapter 2 also apply here because the urban extent map was used as a mask for areas with and without buildings. It is not clear how much the Landsat-derived urban extent map and other Landsat-based inputs (e.g., IS map and segmentation results) affected the mapping accuracy. For example, Landsat-based segmentation was used as spatial

units of height information extraction. Height information from DSM was not considered in the segmentation of building and non-building patches. Inaccurate delineation of building patches may introduce biases and errors in estimated height. More systematic investigations are needed to determine the optimal strategy for synergic use of Landsat and DSM data.

4.6 Conclusion

Urbanization is a 3D phenomenon that needs to be observed through remote sensing in not only the traditional 2D space but also the vertical domain. This chapter presents an innovative methodology combining the strength of Landsat imagery and freely available global elevation datasets to spatially map the building height and volume across all of England. It was demonstrated that the proposed method can achieve a reasonably high accuracy, even with suboptimal data. The method was applied to England and assessed using a cross-validation approach based on Lidar measurements. For all of England, the overall height RMSE was only ±1.61 m for the average building height at 30 m resolution. The building volume RMSE was ±1142.3 m^3 for 30 m pixels. Also, the mapped building volume had strong correlation with population, GDP, and CO_2 emission variables at the metropolis scale, indicating a good overall performance of the building volume mapping method and a potential for integrating the mapped building volume in socioeconomic studies.

Despite great limitations in data availability, the proposed method exhibits great potential for large-area characterization of urban structures. Spatial maps of urban structural information, including building height and volume, are important for many

urban applications including disaster vulnerability assessment, climate change adaptation, and population estimation. With the increasing availability of global elevation datasets, it is possible to generate global products of 3D urban structures, which will greatly enhance our understanding of urbanization, particularly in the fields of urban vulnerability to natural disasters, urban heat island effect and patterns of local weather, environmental sustainability of urbanization.

Chapter 5: Concluding Remarks

5.1 Major Findings and Contributions

Urbanization is a global phenomenon with far-reaching environmental impacts, challenging sustainability and food security and raising important questions about policies on urban growth and governance. Monitoring, understanding, and modeling its trends and impacts require accurate, spatially detailed, and updatable information of the urban extent, change rate, and structure. This dissertation seeks to meet this urgent need through innovative processing of freely available data. In this section, I summarize the major findings of the primary chapters and contributions made.

First, I developed a hierarchical object-based texture (HOTex) approach to address the issues of spectral confusion and inconsistency in global urban mapping (Chapter 2). A preliminary assessment of the method in Europe has yielded an overall accuracy of 97.9%, user's accuracy of 91.4%, producer's accuracy of 92.8%, and kappa statistic of 0.91 when evaluated using scene-level cross-validation (SLCV) designed to minimize potential biases in accuracy estimates due to spatial autocorrelations between training and testing data. Based on assessments for the entire continent of Europe, the proposed method generated products comparable to the GlobeLand30 global land cover product and two recently released global urban datasets in areas in which their definitions agree. These results demonstrate that the proposed method can effectively map the urban extent over large areas and generate consistently accurate results using images with acquisition time, illumination, and phenology

differences. In addition, the proposed method is not only highly accurate, but also demonstrated global applicability from its application on the entire global land survey (GLS) Landsat dataset.

Second, a method was designed to map the sub-pixel impervious surface change (ISC) using bi-temporal Landsat data (Chapter 3). Landsat-based estimation of IS is subject to seasonal and phenological variations, which leads to biases and errors of the ISC when estimated using the simple difference of bi-temporal IS values estimated by the same model. To address this issue, an iteration training and prediction (ITP) approach was adopted to automatically transfer an IS regression tree model for the 2010 epoch to the 2000 epoch on an image-by-image basis. The method was applied to India to produce an ISC map for the period from 2000 to 2010. Assessed using an independent reference dataset developed by this study, the ITP algorithm reduced the bias of ISC from 20.61% to 8.41%. According to the statistical analysis and accuracy assessment of this map, the total ISC for India between 2000 and 2010 is 2274.62 ± 7.84 km^2 at 95% confidence. Furthermore, the accuracy of ISC estimation using the proposed method was demonstrated by the strong correlations between ISC and changes of socioeconomic variables, including population and GDP.

Finally, Chapter 4 attempts to map the vertical structure of urban areas, that is, the building height and volume. Due to the limited availability of elevation data, the characterization of urban areas in the vertical domain has been limited to individual cities. Here, I mapped the building height and volume at 30 m resolution using the synergy of Landsat imagery and freely available global elevation datasets. The HOTex approach used in Chapter 2 was adopted and was proven to be an effective data fusion

approach as well as a useful feature extraction framework for machine learning. Tested over the entire country of England and assessed using Lidar measurements, the height RMSE of the prosed method was estimated to be 1.61 m for the average building height at 30 m resolution, while the building volume RMSE was 1142.3 m^3. The mapped building volume were shown to in good correlation ($R^2 > 0.8$) with socioeconomic variables including population, GDP, and transportation CO_2 emission, which indicated that the mapped building volume is accurate and has great potential for applications in socioeconomic studies.

The unique contributions of this dissertation include:

1. An approach was developed to consistently maps the urban extent using images containing phenological differences. The method was applied to the Global Land Survey 2010 dataset to produce a circa-2010 global HBASE map, which is distributed through the NASA Socioeconomic Data and Applications Center (SEDAC; (Wang et al. 2017). By adopting an urban extent definition that includes all human built-up and settlement extents (HBASE), this product is unique among global urban products because of its balanced definition considering both physical properties and functions of urban areas. Therefore, the HBASE product may provide much-needed consistent definitions of urban population and economic activities in socioeconomic studies.
2. A method was established to map the ISC at national scales. It does not require time series data nor training data for both dates. It has been successfully used to produce a 2000-2010 ISC dataset for India. The

proposed method has a great potential for generating a multi-decadal record of global urbanization from the Landsat archive, which would greatly benefit the study of global urbanization impacts and socioeconomic drivers of urbanization.

3. Building height and volume was mapped at fine spatial resolution (30 m) for the first time at the scale of a country using a method based on the synergy of Landsat and global DSM datasets. The biggest implication of the success of this study is that, with advanced data processing and machine learning techniques, it is possible to generate global products of 3D urban structures using freely available datasets. Such products would be highly valuable in many urban science applications including population distribution mapping and disaster vulnerability assessment. Furthermore, by demonstrating the value of accurate elevation measurements in these applications, this study may provide useful information for planning future Earth observation missions.

5.2 Future Research Directions

In this dissertation, I took concrete steps towards the goal of advancing urban remote sensing to better characterize the urban extent, change, and structure. Following this work, there are several research directions worth pursing in future studies.

First, the methods developed in previous chapters showed great potentials for fully automated global applications. The availability of new datasets provides greater prospects of applying these methods to generate global products. Datasets such as Landsat-8, Sentinel-2, annual stable nightlights from VIIRS (Elvidge et al. 2017), may

be used to better address issues associated with SLC-off gaps or other GLS data issues. Using bistatic InSAR technology, the global DSM from TanDEM-X has superior spatial coverage, spatial resolution (12 m) and vertical accuracy (relative vertical accuracy ~ 2 m for most terrains) over existing products, promising a better mapping accuracy for building height and volume (Gruber et al. 2012; Rizzoli et al. 2017). In addition, space-borne Lidar missions, including the Global Ecosystem Dynamics Investigation (GEDI) and the Ice, Cloud and land Elevation Satellite-2 (ICESAT-2), will generate globally distributed accurate elevation measurements (Abdalati et al. 2010; Dubayah et al. 2014). These measurements would be highly valuable for training building height estimation models and the validation of results. Therefore, it would be interesting to test the combination of new datasets with the methods developed in this dissertation in large-scale applications.

Second, the methods and products developed in this dissertation enable exploration of the science questions related to the challenges of urbanization identified in Chapter 1. For example, one of the limitations of existing assessments of urban vulnerability to natural hazards is that they only consider the exposures of population and GDP to different hazards (Dilley et al. 2005). With the large-scale building volume mapping capability developed in this dissertation, the exposure of building volume to natural hazards cloud be spatially mapped to quantify the vulnerability of global buildings and infrastructures. Another possible research direction is the mapping of long-term impervious surface change for assessing the total climate forcing of urbanization, including both indirect effects, such as carbon loss due to the conversion of productive lands to IS, and direct effects, such as the urban heat island effect.

Bibliography

Abdalati, W., Zwally, H.J., Bindschadler, R., Csatho, B., Farrell, S.L., Fricker, H.A., Harding, D., Kwok, R., Lefsky, M., & Markus, T. (2010). The ICESat-2 laser altimetry mission. *Proceedings of the IEEE, 98*, 735-751

Arino, O., Gross, D., Ranera, F., Leroy, M., Bicheron, P., Brockman, C., Defourny, P., Vancutsem, C., Achard, F., Durieux, L., Bourg, L., Latham, J., Di Gregorio, A., Witt, R., Herold, M., Sambale, J., Plummer, S., & Weber, J.L. (2007). Globcover: Esa Service for Global Land Cover from Meris. *Igarss: 2007 IEEE International Geoscience and Remote Sensing Symposium, Vols 1-12*, 2412-2415

Arnfield, A.J. (2003). Two Decades of Urban Climate Research: A Review of Turbulence, Exchanges of Energy and Water, and the Urban Heat Island. *International Journal of Climatology, 23*, 1-26

Arnold, C.L., & Gibbons, C.J. (1996). Impervious Surface Coverage: The Emergence of a Key Environmental Indicator. *Journal of the American Planning Association, 62*, 243-258

Arvidson, T., Goward, S., Gasch, J., & Williams, D. (2006). Landsat-7 long-term acquisition plan: Development and validation. *Photogrammetric Engineering and Remote Sensing, 72*, 1137-1146

Avelar, S., Zah, R., & Tavares-Corrêa, C. (2009). Linking Socioeconomic Classes and Land Cover Data in Lima, Peru: Assessment through the Application of Remote Sensing and Gis. *International Journal of Applied Earth Observation and Geoinformation, 11*, 27-37

Baiocchi, G., Creutzig, F., Minx, J., & Pichler, P.-P. (2015). A Spatial Typology of Human Settlements and Their Co2 Emissions in England. *Global Environmental Change, 34*, 13-21

Bartholomé, E., & Belward, A.S. (2005). Glc2000: A New Approach to Global Land Cover Mapping from Earth Observation Data. *International Journal of Remote Sensing, 26*, 1959-1977

Baugh, K., Hsu, F.-C., Elvidge, C.D., & Zhizhin, M. (2013). Nighttime lights compositing using the VIIRS day-night band: Preliminary results. *Proceedings of the Asia-Pacific Advanced Network, 35*, 70-86

Bechle, M.J., Millet, D.B., & Marshall, J.D. (2015). National Spatiotemporal Exposure Surface for No2: Monthly Scaling of a Satellite-Derived Land-Use Regression, 2000-2010. *Environ Sci Technol, 49*, 12297-12305

Bogardi, J.J., Dudgeon, D., Lawford, R., Flinkerbusch, E., Meyn, A., Pahl-Wostl, C., Vielhauer, K., & Vörösmarty, C. (2012). Water security for a planet under pressure: interconnected challenges of a changing world call for sustainable solutions. *Current Opinion in Environmental Sustainability, 4*, 35-43

Bounoua, L., Zhang, P., Mostovoy, G., Thome, K., Masek, J., Imhoff, M., Shepherd, M., Quattrochi, D., Santanello, J., Silva, J., Wolfe, & Toure, A.M. (2015). Impact of Urbanization on Us Surface Climate. *Environmental Research Letters, 10*, 084010

Brabec, E., Schulte, S., & Richards, P.L. (2002). Impervious Surfaces and Water Quality: A Review of Current Literature and Its Implications for Watershed Planning. *Journal of Planning Literature, 16*, 499-514

Breiman, L. (2001). Random Forests. *Machine Learning, 45*, 5-32

Brezzi, M. (2012). *Redefining" urban": A New Way to Measure Metropolitan Areas*. OECD

Brockerhoff, M. (1999). Urban Growth in Developing Countries: A Review of Projections and Predictions. Croissance Urbaine Dans Les Pays En Voie De Developpement: Recapitulation Des Previsions Et Predictions. El Crecimiento Urbano En Los Paises En Desarrollo: Examen De Las Proyecciones Y Predicciones. *Population and Development Review, 25*, 757-778

Brown de Colstoun, E.C., Huang, C., Wang, P., Tilton, J.C., Tan, B., Phillips, J., Niemczura, S., Ling, P.-Y., & Wolfe, R. (2017). Global Man-made Impervious Surfaces & Settlement Extents from Landsat. *Available online at:* http://beta.www.ciesin.columbia.edu/mapping/gmis-hbase/

Chen, D., Stow, D.A., & Gong, P. (2004). Examining the Effect of Spatial Resolution and Texture Window Size on Classification Accuracy: An Urban Environment Case. *International Journal of Remote Sensing, 25*, 2177-2192

Chen, J., Chen, J., Liao, A., Cao, X., Chen, L., Chen, X., He, C., Han, G., Peng, S., Lu, M., Zhang, W., Tong, X., & Mills, J. (2015a). Global land cover mapping at 30 m resolution: A POK-based operational approach. *ISPRS Journal of Photogrammetry and Remote Sensing, 103*, 7-27

Chen, J., Chen, J., Liao, A., Cao, X., Chen, L., Chen, X., He, C., Han, G., Peng, S., Lu, M., Zhang, W., Tong, X., & Mills, J. (2015b). Global land cover mapping at 30m resolution: A POK-based operational approach. *ISPRS Journal of Photogrammetry and Remote Sensing, 103*, 7-27

Chen, M., Zhang, H., Liu, W., & Zhang, W. (2014). The Global Pattern of Urbanization and Economic Growth: Evidence from the Last Three Decades. *Plos One, 9*, e103799

Cheng, F., Wang, C., Wang, J., Tang, F., & Xi, X. (2011). Trend Analysis of Building Height and Total Floor Space in Beijing, China Using Icesat/Glas Data. *International Journal of Remote Sensing, 32*, 8823-8835

Cheshmehzangi, A., & Butters, C. (2016). Sustainable Living and Urban Density: The Choices are Wide Open. *Energy Procedia, 88*, 63-70

CIESIN (Center for International Earth Science Information Network) (2011). Global Rural-Urban Mapping Project, Version 1 (GRUMPv1): Urban Extents. *Available online at:* http://sedac.ciesin.columbia.edu/data/collection/grump-v1 *(accessed 5-15-2016).*

Clausi, D.A. (2002). An analysis of co-occurrence texture statistics as a function of grey level quantization. *Canadian Journal of Remote Sensing, 28*, 45-62

Cohen, B. (2004). Urban Growth in Developing Countries: A Review of Current Trends and a Caution Regarding Existing Forecasts. *World Development, 32*, 23-51

Cohen, J.E. (1995). Population Growth and Earth's Human Carrying Capacity. *Science, 269*, 341-346

Cohen, M., & Garrett, J.L. (2009). The Food Price Crisis and Urban Food (in)Security. In, *Urbanization and Emerging Population Issues Working Paper Series*. London: IIED/UNFPA

Congalton, R. (1991). A review of assessing the accuracy of classifications of remotely sensed data. *Remote Sensing of Environment, 37*, 35-46

Copernicus Land Monitoring Services (2015). Validation of the Urban Atlas products: UA2012 and change 2006-2012, summary of preliminary results. In

Cotton, A., & Franceys, R. (1994). Infrastructure for the Urban Poor. *Cities, 11*, 15-24

Council, N.R. (1998). *People and Pixels: Linking Remote Sensing and Social Science*. Washington, DC: The National Academies Press

Creutzig, F., Baiocchi, G., Bierkandt, R., Pichler, P.-P., & Seto, K.C. (2015). Global Typology of Urban Energy Use and Potentials for an Urbanization Mitigation Wedge. *Proceedings of the National Academy of Sciences*

Crist, E.P. (1985). A Tm Tasseled Cap Equivalent Transformation for Reflectance Factor Data. *Remote Sensing of Environment, 17*, 301-306

Cutter, S.L., & Finch, C. (2008). Temporal and Spatial Changes in Social Vulnerability to Natural Hazards. *Proc Natl Acad Sci U S A, 105*, 2301-2306

DeFries, R.S., Rudel, T., Uriarte, M., & Hansen, M. (2010). Deforestation Driven by Urban Population Growth and Agricultural Trade in the Twenty-First Century. *Nature Geoscience, 3*, 178-181

Didan, K. (2015). MOD13C2 MODIS/Terra Vegetation Indices Monthly L3 Global 0.05Deg CMG V006. *NASA EOSDIS Land Processes DAAC. Available online at:* http://doi.org/10.5067/MODIS/MOD13C2.006 *(accessed 2-5-2016).*

Dilley, M., Chen, R.S., Deichmann, U., LernerLam, A.L., & Arnold, M. (2005). Natural Disaster Hotspots: A Global Risk Analysis. In, *Disaster Risk Management Series*: World Bank

Dubayah, R., Goetz, S., Blair, J.B., Fatoyinbo, T., Hansen, M., Healey, S., Hofton, M., Hurtt, G., Kellner, J., & Luthcke, S. (2014). The global ecosystem dynamics investigation. In, *AGU Fall Meeting Abstracts*

Duncan, B.N., Lamsal, L.N., Thompson, A.M., Yoshida, Y., Lu, Z., Streets, D.G., Hurwitz, M.M., & Pickering, K.E. (2016). A Space-Based, High-Resolution View of Notable Changes in Urban Noxpollution around the World (2005-2014). *Journal of Geophysical Research: Atmospheres, 121*, 976-996

Earth Observation Group, NOAA National Geophysical Data Center, (2016). DMSP & VIIRS Data Download. *Available online at:* http://ngdc.noaa.gov/eog/download.html *(accessed 4-6-2016).*

Elvidge, C.D., Baugh, K., Zhizhin, M., Hsu, F.C., & Ghosh, T. (2017). VIIRS night-time lights. *International Journal of Remote Sensing, 38*, 5860-5879

Elvidge, C.D., Tuttle, B.T., Sutton, P.C., Baugh, K.E., Howard, A.T., Milesi, C., Bhaduri, B., & Nemani, R. (2007). Global Distribution and Density of Constructed Impervious Surfaces. *Sensors, 7*, 1962-1979

Emu Analytics (2016). Emu DataPacks: English Urban Areas Building Heights. *Available online at* http://www.emu-analytics.com/products/datapacks.php *(accessed on 30-12-2016).*

Esch, T., Marconcini, M., Felbier, A., Roth, A., Heldens, W., Huber, M., Schwinger, M., Taubenbock, H., Muller, A., & Dech, S. (2013). Urban Footprint Processor-Fully Automated Processing Chain Generating Settlement Masks From Global Data of the TanDEM-X Mission. *IEEE Geoscience and Remote Sensing Letters, 10*, 1617-1621

Esch, T., Taubenböck, H., Roth, A., Heldens, W., Felbier, A., Thiel, M., Schmidt, M., Müller, A., & Dech, S. (2012). Tandem-X Mission—New Perspectives for the Inventory and Monitoring of Global Settlement Patterns. *Journal of Applied Remote Sensing, 6*, 061702-061701

European Environment Agency (EEA) (2016). Urban Atlas 2012 *Available online at:* http://land.copernicus.eu/local/urban-atlas/urban-atlas-2012 *(accessed 4-12-2016).*

Feng, M., Huang, C., Channan, S., Vermote, E.F., Masek, J.G., & Townshend, J.R. (2012). Quality assessment of Landsat surface reflectance products using MODIS data. *Computers & Geosciences, 38*, 9-22

Feng, M., Sexton, J.O., Huang, C., Masek, J.G., Vermote, E.F., Gao, F., Narasimhan, R., Channan, S., Wolfe, R.E., & Townshend, J.R. (2013). A Global Land Survey surface reflectance product: assessment using coincident MODIS observations. *Remote Sensing of Environment, 134*, 276-293

Fichot, C.G., Downing, B.D., Bergamaschi, B.A., Windham-Myers, L., Marvin-DiPasquale, M., Thompson, D.R., & Gierach, M.M. (2016). High-Resolution Remote Sensing of Water Quality in the San Francisco Bay-Delta Estuary. *Environ Sci Technol, 50*, 573-583

Foley, J.A., Defries, R., Asner, G.P., Barford, C., Bonan, G., Carpenter, S.R., Chapin, F.S., Coe, M.T., Daily, G.C., Gibbs, H.K., Helkowski, J.H., Holloway, T., Howard, E.A., Kucharik, C.J., Monfreda, C., Patz, J.A., Prentice, I.C., Ramankutty, N., & Snyder, P.K. (2005). Global Consequences of Land Use. *Science, 309*, 570-574

Friedl, M.A., Brodley, C.E., & Strahler, A.H. (1999). Maximizing land cover classification accuracies produced by decision trees at continental to global scales. *IEEE Transactions on Geoscience and Remote Sensing, 37*, 969-977

Friedl, M.A., Sulla-Menashe, D., Tan, B., Schneider, A., Ramankutty, N., Sibley, A., & Huang, X. (2010). Modis Collection 5 Global Land Cover: Algorithm Refinements and Characterization of New Datasets. *Remote Sensing of Environment, 114*, 168-182

Frolking, S., Milliman, T., Seto, K.C., & Friedl, M.A. (2013). A Global Fingerprint of Macro-Scale Changes in Urban Structure from 1999 to 2009. *Environmental Research Letters, 8*, 024004

Fuller, R.M., Smith, G.M., Sanderson, J.M., Hill, R.A., Thomson, A.G., Cox, R., Brown, N.J., Clarke, R.T., Rothery, P., & Gerard, F.F. (2002). Countryside Survey 2000 Module 7. Land Cover Map 2000. Final Report

GADM (2015). Global Administrative Areas (GADM) Dataset Version 2.8. *Available online at* http://gadm.org *(accessed on 30-10-2016).*

Gamba, P., Houshmand, B., & Saccani, M. (2000). Detection and extraction of buildings from interferometric SAR data. *IEEE Transactions on Geoscience and Remote Sensing, 38*, 611-618

Geiß, C., Jilge, M., Lakes, T., & Taubenböck, H. (2016). Estimation of Seismic Vulnerability Levels of Urban Structures With Multisensor Remote Sensing. *IEEE Journal of Selected Topics in Applied Earth Observations and Remote Sensing, 9*, 1913-1936

Geiss, C., Wurm, M., Breunig, M., Felbier, A., & Taubenbock, H. (2015). Normalization of Tandem-X Dsm Data in Urban Environments with Morphological Filters. *IEEE Transactions on Geoscience and Remote Sensing, 53*, 4348-4362

Gong, P. (1994). Reducing Boundary Effects in a Kernel-Based Classifier. *International Journal of Remote Sensing, 15*, 1131-1139

Gong, P., & Howarth, P.J. (1990). The Use of Structural Information for Improving Land-Cover Classification Accuracies at the Rural-Urban Fringe. *Photogrammetric Engineering and Remote Sensing, 56*, 67-73

Gong, P., Li, Z., Huang, H., Sun, G., & Wang, L. (2011). Icesat Glas Data for Urban Environment Monitoring. *IEEE Transactions on Geoscience and Remote Sensing, 49*, 1158-1172

Gong, P., Marceau, D.J., & Howarth, P.J. (1992). A Comparison of Spatial Feature-Extraction Algorithms for Land-Use Classification with Spot Hrv Data. *Remote Sensing of Environment, 40*, 137-151

Gong, P., Wang, J., Yu, L., Zhao, Y., Zhao, Y., Liang, L., Niu, Z., Huang, X., Fu, H., Liu, S., Li, C., Li, X., Fu, W., Liu, C., Xu, Y., Wang, X., Cheng, Q., Hu, L., Yao, W., Zhang, H., Zhu, P., Zhao, Z., Zhang, H., Zheng, Y., Ji, L., Zhang, Y., Chen, H., Yan, A., Guo, J., Yu, L., Wang, L., Liu, X., Shi, T., Zhu, M., Chen, Y., Yang, G., Tang, P., Xu, B., Giri, C., Clinton, N., Zhu, Z., Chen, J., & Chen, J. (2013). Finer Resolution Observation and Monitoring of Global Land Cover: First Mapping Results with Landsat Tm and Etm+ Data. *International Journal of Remote Sensing, 34*, 2607-2654

Gonzalez-Aguilera, D., Crespo-Matellan, E., Hernandez-Lopez, D., & Rodriguez-Gonzalvez, P. (2013). Automated Urban Analysis Based on LiDAR-Derived Building Models. *IEEE Transactions on Geoscience and Remote Sensing, 51*, 1844-1851

Grossman, G.M., & Krueger, A.B. (1991). Environmental impacts of a North American free trade agreement. In: National Bureau of Economic Research

Gruber, A., Wessel, B., Huber, M., & Roth, A. (2012). Operational Tandem-X Dem Calibration and First Validation Results. *ISPRS Journal of Photogrammetry and Remote Sensing, 73*, 39-49

Guindon, B., & Zhang, Y. (2009). Automated Urban Delineation from Landsat Imagery Based on Spatial Information Processing. *Photogrammetric Engineering and Remote Sensing, 75*, 845-858

Gutman, G., Byrnes, R., Masek, J., Covington, S., Justice, C., Franks, S., & Headley, R. (2008). Towards monitoring land-cover and land-use changes at a global scale: The Global Land Survey 2005. *Photogrammetric Engineering and Remote Sensing, 74*, 6-10

Gutman, G., Huang, C., Chander, G., Noojipady, P., & Masek, J. (2013). Assessment of the NASA-USGS Global Land Survey (GLS) Datasets. *Remote Sensing of Environment, 134*, 249-265

Haack, B.N., Solomon, E.K., Bechdol, M.A., & Herold, N.D. (2002). Radar and Optical Data Comparison/Integration for Urban Delineation: A Case Study. *Photogrammetric Engineering and Remote Sensing, 68*, 1289-1296

Hansen, M.C., Defries, R.S., Townshend, J.R.G., & Sohlberg, R. (2000). Global Land Cover Classification at 1 Km Spatial Resolution Using a Classification Tree Approach. *International Journal of Remote Sensing, 21*, 1331-1364

Hansen, M.C., Potapov, P.V., Moore, R., Hancher, M., Turubanova, S.A., Tyukavina, A., Thau, D., Stehman, S.V., Goetz, S.J., Loveland, T.R., Kommareddy, A., Egorov, A., Chini, L., Justice, C.O., & Townshend, J.R.G. (2013). High-Resolution Global Maps of 21st-Century Forest Cover Change. *Science, 342*, 850-853

Haralick, R.M., Shanmugam, K., & Dinstein, I.H. (1973). Textural Features for Image Classification. *IEEE Transactions on Systems, Man, and Cybernetics, 3*, 610-621

Hermosilla, T., Wulder, M.A., White, J.C., Coops, N.C., & Hobart, G.W. (2015). An integrated Landsat time series protocol for change detection and generation of annual gap-free surface reflectance composites. *Remote Sensing of Environment, 158*, 220-234

Herold, M., Gardner, M.E., & Roberts, D.A. (2003a). Spectral Resolution Requirements for Mapping Urban Areas. *IEEE Transactions on Geoscience and Remote Sensing, 41*, 1907-1919

Herold, M., Liu, X.H., & Clarke, K.C. (2003b). Spatial Metrics and Image Texture for Mapping Urban Land Use. *Photogrammetric Engineering and Remote Sensing, 69*, 991-1001

Herold, M., Roberts, D.A., Gardner, M.E., & Dennison, P.E. (2004). Spectrometry for Urban Area Remote Sensing—Development and Analysis of a Spectral Library from 350 to 2400 Nm. *Remote Sensing of Environment, 91*, 304-319

Hodgson, M.E. (1998). What Size Window for Image Classification? A Cognitive Perspective. *Photogrammetric Engineering and Remote Sensing, 64*, 797-807

Horn, B.K.P. (1981). Hill Shading and the Reflectance Map. *Proceedings of the IEEE, 69*, 14-47

Hsieh, S.-C. (2014). Analyzing Urbanization Data Using Rural–Urban Interaction Model and Logistic Growth Model. *Computers, Environment and Urban Systems, 45*, 89-100

Huang, C., Goward, S.N., Schleeweis, K., Thomas, N., Masek, J.G., & Zhu, Z. (2009). Dynamics of National Forests Assessed Using the Landsat Record: Case Studies in Eastern United States. *Remote Sensing of Environment, 113*, 1430-1442

Huang, C.Q., Peng, Y., Lang, M.G., Yeo, I.Y., & McCarty, G. (2014). Wetland inundation mapping and change monitoring using Landsat and airborne LiDAR data. *Remote Sensing of Environment, 141*, 231-242

Imhoff, M.L., Lawrence, W.T., Stutzer, D.C., & Elvidge, C.D. (1997). A Technique for Using Composite Dmsp/Ols "City Lights" Satellite Data to Map Urban Area. *Remote Sensing of Environment, 61*, 361-370

Imhoff, M.L., Zhang, P., Wolfe, R.E., & Bounoua, L. (2010). Remote Sensing of the Urban Heat Island Effect across Biomes in the Continental USA. *Remote Sensing of Environment, 114*, 504-513

Irons, J.R., Dwyer, J.L., & Barsi, J.A. (2012). The next Landsat satellite: The Landsat Data Continuity Mission. *Remote Sensing of Environment, 122*, 11-21

Jantz, C., Goetz, S., & Shelley, M. (2004). Using the Sleuth Urban Growth Model to Simulate the Impacts of Future Policy Scenarios on Urban Land Use in the Baltimore-Washington Metropolitan Area. *Environment and Planning B-Planning & Design, 31*, 251-271

Jensen, J.R., & Cowen, D.C. (1999). Remote sensing of urban suburban infrastructure and socio-economic attributes. *Photogrammetric Engineering and Remote Sensing, 65*, 611-622

Jiang, L., Deng, X.Z., & Seto, K.C. (2013). The Impact of Urban Expansion on Agricultural Land Use Intensity in China. *Land Use Policy, 35*, 33-39

Kammen, D.M., & Sunter, D.A. (2016). City-Integrated Renewable Energy for Urban Sustainability. *Science, 352*, 922-928

Kaye, J.P., Groffman, P.M., Grimm, N.B., Baker, L.A., & Pouyat, R.V. (2006). A Distinct Urban Biogeochemistry? *Trends Ecol Evol, 21*, 192-199

Klotz, M., Kemper, T., Geiss, C., Esch, T., & Taubenbock, H. (2016). How good is the map? A multi-scale cross-comparison framework for global settlement layers: Evidence from Central Europe. *Remote Sensing of Environment, 178*, 191-212

Krieger, G., Moreira, A., Fiedler, H., Hajnsek, I., Werner, M., Younis, M., & Zink, M. (2007). Tandem-X: A Satellite Formation for High-Resolution Sar Interferometry. *IEEE Transactions on Geoscience and Remote Sensing, 45*, 3317-3341

Kriegler, F.J., Malila, W.A., Nalepka, R.F., & Richardson, W. (1969). Preprocessing Transformations and Their Effects on Multispectral Recognition. In, *Remote Sensing of Environment, VI* (p. 97)

Lambin, E.F., Geist, H.J., & Lepers, E. (2003). Dynamics of land-use and land-cover change in tropical regions. *Annual Review of Environment and Resources, 28*, 205-241

Lambin, E.F., & Meyfroidt, P. (2010). Land Use Transitions: Socio-Ecological Feedback Versus Socio-Economic Change. *Land Use Policy, 27*, 108-118

Lambin, E.F., Turner, B.L., Geist, H.J., Agbola, S.B., Angelsen, A., Bruce, J.W., Coomes, O.T., Dirzo, R., Fischer, G., Folke, C., George, P.S., Homewood, K., Imbernon, J., Leemans, R., Li, X., Moran, E.F., Mortimore, M., Ramakrishnan, P.S., Richards, J.F., Skånes, H., Steffen, W., Stone, G.D., Svedin, U., Veldkamp, T.A., Vogel, C., & Xu, J. (2001). The Causes of Land-Use and Land-Cover Change: Moving Beyond the Myths. *Global Environmental Change, 11*, 261-269

Lamsal, L.N., Martin, R.V., Parrish, D.D., & Krotkov, N.A. (2013). Scaling Relationship for No2 Pollution and Urban Population Size: A Satellite Perspective. *Environ Sci Technol, 47*, 7855-7861

Larsen, T.A., Hoffmann, S., Lüthi, C., Truffer, B., & Maurer, M. (2016). Emerging Solutions to the Water Challenges of an Urbanizing World. *Science, 352*, 928-933

Lederbogen, F., Kirsch, P., Haddad, L., Streit, F., Tost, H., Schuch, P., Wust, S., Pruessner, J.C., Rietschel, M., Deuschle, M., & Meyer-Lindenberg, A. (2011). City living and urban upbringing affect neural social stress processing in humans. *Nature, 474*, 498-501

Li, J., & Roy, D. (2017). A Global Analysis of Sentinel-2A, Sentinel-2B and Landsat-8 Data Revisit Intervals and Implications for Terrestrial Monitoring. *Remote Sensing, 9*, 902

Li, S., & Ma, Y. (2014). Urbanization, Economic Development and Environmental Change. *Sustainability, 6*, 5143-5161

Li, W., & Wu, C. (2014). Phenology-Based Temporal Mixture Analysis for Estimating Large-Scale Impervious Surface Distributions. *International Journal of Remote Sensing, 35*, 779-795

Li, X., Xu, H., Chen, X., & Li, C. (2013). Potential of Npp-Viirs Nighttime Light Imagery for Modeling the Regional Economy of China. *Remote Sensing, 5*, 3057-3081

Liu, W.G., & Seto, K.C. (2008). Using the Art-Mmap Neural Network to Model and Predict Urban Growth: A Spatiotemporal Data Mining Approach. *Environment and Planning B-Planning & Design, 35*, 296-317

Liu, Z., He, C., Zhou, Y., & Wu, J. (2014). How Much of the World's Land Has Been Urbanized, Really? A Hierarchical Framework for Avoiding Confusion. *Landscape Ecology, 29*, 763-771

Loveland, T.R., & Belward, A.S. (1997). The Igbp-Dis Global 1 Km Land Cover Data Set, Discover: First Results. *International Journal of Remote Sensing, 18*, 3291-3295

Lu, D.S., Li, G.Y., Kuang, W.H., & Moran, E. (2014). Methods to Extract Impervious Surface Areas from Satellite Images. *International Journal of Digital Earth, 7*, 93-112

Lu, Z., Im, J., Quackenbush, L., & Halligan, K. (2010). Population Estimation Based on Multi-Sensor Data Fusion. *International Journal of Remote Sensing, 31*, 5587-5604

Lu, Z., Kwoun, O., & Rykhus, R. (2007). Interferometric synthetic aperture radar (InSAR): Its past, present and future. *Photogrammetric Engineering and Remote Sensing, 73*, 217-221

Lu, Z.Y., Im, J., & Quackenbush, L. (2011). A Volumetric Approach to Population Estimation Using Lidar Remote Sensing. *Photogrammetric Engineering and Remote Sensing, 77*, 1145-1156

Mäenpää, T., & Pietikäinen, M. (2004). Classification with Color and Texture: Jointly or Separately? *Pattern Recognition, 37*, 1629-1640

Maguya, A.S., Junttila, V., & Kauranne, T. (2013). Adaptive algorithm for large scale dtm interpolation from lidar data for forestry applications in steep forested terrain. *ISPRS Journal of Photogrammetry and Remote Sensing, 85*, 74-83

Marceau, D.J., Howarth, P.J., Dubois, J.M., & Gratton, D.J. (1990). Evaluation Of The Grey-level Co-occurrence Matrix Method For Land-cover Classification Using Spot Imagery. *IEEE Transactions on Geoscience and Remote Sensing, 28*, 513-519

Masek, J.G., Vermote, E.F., Saleous, N.E., Wolfe, R., Hall, F.G., Huemmrich, K.F., Gao, F., Kutler, J., & Lim, T.K. (2006). A Landsat Surface Reflectance Dataset for North America, 1990–2000. *IEEE Geoscience and Remote Sensing Letters, 3*, 68-72

Masson, V. (2006). Urban surface modeling and the meso-scale impact of cities. *Theoretical and Applied Climatology, 84*, 35-45

McDonald, R.I., Weber, K., Padowski, J., Flörke, M., Schneider, C., Green, P.A., Gleeson, T., Eckman, S., Lehner, B., Balk, D., Boucher, T., Grill, G., & Montgomery, M. (2014). Water on an Urban Planet: Urbanization and the Reach of Urban Water Infrastructure. *Global Environmental Change, 27*, 96-105

McGrane, S.J. (2016). Impacts of urbanisation on hydrological and water quality dynamics, and urban water management: a review. *Hydrological Sciences Journal, 61*, 2295-2311

Meng, X.L., Currit, N., & Zhao, K.G. (2010). Ground Filtering Algorithms for Airborne LiDAR Data: A Review of Critical Issues. *Remote Sensing, 2*, 833-860

Mosquera-Machado, S., & Dilley, M. (2008). A Comparison of Selected Global Disaster Risk Assessment Results. *Natural Hazards, 48*, 439-456

Mukherjee, S., Joshi, P.K., Mukherjee, S., Ghosh, A., Garg, R.D., & Mukhopadhyay, A. (2013). Evaluation of vertical accuracy of open source Digital Elevation Model (DEM). *International Journal of Applied Earth Observation and Geoinformation, 21*, 205-217

Myint, S.W. (2003). Fractal Approaches in Texture Analysis and Classification of Remotely Sensed Data: Comparisons with Spatial Autocorrelation Techniques and Simple Descriptive Statistics. *International Journal of Remote Sensing, 24*, 1925-1947

Myint, S.W., & Lam, N. (2005). Examining Lacunarity Approaches in Comparison with Fractal and Spatial Autocorrelation Techniques for Urban Mapping. *Photogrammetric Engineering and Remote Sensing, 71*, 927-937

Myint, S.W., Lam, N., & Tyler, J.M. (2004). Wavelets for Urban Spatial Feature Discrimination: Comparisons with Fractal, Spatial Autocorrelation, and Spatial Co-Occurrence Approaches. *Photogrammetric Engineering and Remote Sensing, 70*, 803-812

Nagendra, H., Sudhira, H.S., Katti, M., & Schewenius, M. (2013). Sub-regional Assessment of India: Effects of Urbanization on Land Use, Biodiversity and Ecosystem Services. In T. Elmqvist, M. Fragkias, J. Goodness, B. Güneralp, P.J. Marcotullio, R.I. McDonald, S. Parnell, M. Schewenius, M. Sendstad, K.C. Seto, & C. Wilkinson (Eds.), *Urbanization, Biodiversity and Ecosystem Services:*

Challenges and Opportunities: A Global Assessment (pp. 65-74). Dordrecht: Springer Netherlands

Nghiem, S., Balk, D., Small, C., Deichmann, U., Wannebo, A., Blom, R., Sutton, P., Yetman, G.G., Chen, R.S., Rodriguez, E., Houshmand, B., & Neumann, G. (2001). Global Infrastructure: The Potential of Srtm Data to Break New Ground. In: Center for International Earth Science Information Network

Njoh, A.J. (2016). *Urban planning and public health in Africa: Historical, theoretical and practical dimensions of a continent's water and sanitation problematic*. Routledge

Office of the Registrar General & Census Commissioner of Inida (2011). Provisional Population Totals Paper 2 of 2011. *Available online at* http://www.censusindia.gov.in/2011-prov-results/paper2/census2011_paper2.html *(accessed on 20-11-2016).*

OpenStreetMap contributors (2016). OpenStreetMap Planet dump [Data file from 04-22-2016 of database dump]. *Available online at:* http://planet.openstreetmap.org

Palm, C. (2004). Color Texture Classification by Integrative Co-Occurrence Matrices. *Pattern Recognition, 37*, 965-976

Pandey, B., Joshi, P.K., & Seto, K.C. (2013). Monitoring urbanization dynamics in India using DMSP/OLS night time lights and SPOT-VGT data. *International Journal of Applied Earth Observation and Geoinformation, 23*, 49-61

Pandey, B., & Seto, K.C. (2015). Urbanization and Agricultural Land Loss in India: Comparing Satellite Estimates with Census Data. *Journal of Environmental Management, 148*, 53-66

Patino, J.E., & Duque, J.C. (2013). A Review of Regional Science Applications of Satellite Remote Sensing in Urban Settings. *Computers, Environment and Urban Systems, 37*, 1-17

Pesaresi, M., Guo, H.D., Blaes, X., Ehrlich, D., Ferri, S., Gueguen, L., Halkia, M., Kauffmann, M., Kemper, T., Lu, L.L., Marin-Herrera, M.A., Ouzounis, G.K., Scavazzon, M., Soille, P., Syrris, V., & Zanchetta, L. (2013). A Global Human Settlement Layer From Optical HR/VHR RS Data: Concept and First Results. *IEEE Journal of Selected Topics in Applied Earth Observations and Remote Sensing, 6*, 2102-2131

Pierre, J. (1999). Models of Urban Governance. *Urban Affairs Review, 34*, 372-396

Planning Commission of India (2014). Gross State Domestic Product (GSDP) at Current Prices. *Available online at*

http://planningcommission.nic.in/data/datatable/0306/table%20168.pdf *(accessed on 20-11-2016).*

Potere, D., & Schneider, A. (2007). A Critical Look at Representations of Urban Areas in Global Maps. *GeoJournal, 69*, 55-80

Potere, D., Schneider, A., Angel, S., & Civco, D.L. (2009). Mapping urban areas on a global scale: which of the eight maps now available is more accurate? *International Journal of Remote Sensing, 30*, 6531-6558

Qiu, F., Sridharan, H., & Chun, Y. (2010). Spatial Autoregressive Model for Population Estimation at the Census Block Level Using Lidar-Derived Building Volume Information. *Cartography and Geographic Information Science, 37*, 239-257

Ramaswami, A., Russell, A.G., Culligan, P.J., Sharma, K.R., & Kumar, E. (2016). Meta-Principles for Developing Smart, Sustainable, and Healthy Cities. *Science, 352*, 940-943

Rizzoli, P., Martone, M., Gonzalez, C., Wecklich, C., Borla Tridon, D., Bräutigam, B., Bachmann, M., Schulze, D., Fritz, T., Huber, M., Wessel, B., Krieger, G., Zink, M., & Moreira, A. (2017). Generation and performance assessment of the global TanDEM-X digital elevation model. *ISPRS Journal of Photogrammetry and Remote Sensing, 132*, 119-139

Rodriguez-Galiano, V.F., Ghimire, B., Rogan, J., Chica-Olmo, M., & Rigol-Sanchez, J.P. (2012). An Assessment of the Effectiveness of a Random Forest Classifier for Land-Cover Classification. *ISPRS Journal of Photogrammetry and Remote Sensing, 67*, 93-104

Rodriguez, E., S. Morris, C., & J Belz, E. (2006). A global assessment of SRTM performance. *PHOTOGRAMMETRIC ENGINEERING & REMOTE SENSING, 72*, 249–260

Rossi, C., Fritz, T., Breit, H., & Eineder, M. (2011). First Urban Tandem-X Rawdems Analysis. In, *Proceedings of Joint Urban Remote Sensing Event, Jurse* (pp. 65-68)

Rowland, C.S., Morton, R.D., Carrasco, L., McShane, G., O'Neil, A.W., & Wood, C.M. (2017). Land Cover statistics derived from LCM2015

Roy, D.P., Ju, J., Lewis, P., Schaaf, C., Gao, F., Hansen, M., & Lindquist, E. (2008). Multi-temporal MODIS-Landsat data fusion for relative radiometric normalization, gap filling, and prediction of Landsat data. *Remote Sensing of Environment, 112*, 3112-3130

Roy, D.P., Ju, J.C., Kline, K., Scaramuzza, P.L., Kovalskyy, V., Hansen, M., Loveland, T.R., Vermote, E., & Zhang, C.S. (2010). Web-enabled Landsat Data (WELD):

Landsat ETM plus composited mosaics of the conterminous United States. *Remote Sensing of Environment, 114*, 35-49

Rulequest Research (2016). Data Mining with Cubist. In. Available online at https://www.rulequest.com/cubist-info.html (accessed on 16-12-2016)

Samuel, C.Z., Jason, S., Aditya, S., Christopher, J.K., Philip, A.T., & Steven, P.L., II (2016). Urban Heat Island Impacts on Plant Phenology: Intra-Urban Variability and Response to Land Cover. *Environmental Research Letters, 11*, 054023

Satge, F., Denezine, M., Pillco, R., Timouk, F., Pinel, S., Molina, J., Garnier, J., Seyler, F., & Bonnet, M.-P. (2016). Absolute and relative height-pixel accuracy of SRTM-GL1 over the South American Andean Plateau. *ISPRS Journal of Photogrammetry and Remote Sensing, 121*, 157-166

Satterthwaite, D., McGranahan, G., & Tacoli, C. (2010). Urbanization and Its Implications for Food and Farming. *Philos Trans R Soc Lond B Biol Sci, 365*, 2809-2820

Schneider, A. (2012). Monitoring Land Cover Change in Urban and Peri-Urban Areas Using Dense Time Stacks of Landsat Satellite Data and a Data Mining Approach. *Remote Sensing of Environment, 124*, 689-704

Schneider, A., Friedl, M.A., & Potere, D. (2009). A New Map of Global Urban Extent from Modis Satellite Data. *Environmental Research Letters, 4*, 044003

Schneider, A., Friedl, M.A., & Potere, D. (2010). Mapping Global Urban Areas Using Modis 500-M Data: New Methods and Datasets Based on 'Urban Ecoregions'. *Remote Sensing of Environment, 114*, 1733-1746

Seifert, F.M. (2009). Improving Urban Monitoring toward a European Urban Atlas. In P. Gamba, & M. Herold (Eds.), *Global Mapping of Human Settlement: Experiences, Datasets, and Prospects* (p. 231): Taylor & Francis Group

Seto, K.C., & Christensen, P. (2013). Remote Sensing Science to Inform Urban Climate Change Mitigation Strategies. *Urban Climate, 3*, 1-6

Seto, K.C., Dhakal, S., Bigio, A., Blanco, H., Delgado, G.C., Dewar, D., Huang, L., Inaba, A., Kansal, A., Lwasa, S., McMahon, J.E., Müller, D.B., Murakami, J., Nagendra, H., & Ramaswami, A. (2014). Human Settlements, Infrastructure and Spatial Planning. In, *Climate Change 2014: Mitigation of Climate Change. Contribution of Working Group Iii to the Fifth Assessment Report of the Intergovernmental Panel on Climate Change*

Seto, K.C., Fragkias, M., Guneralp, B., & Reilly, M.K. (2011). A Meta-Analysis of Global Urban Land Expansion. *Plos One, 6*, e23777

Seto, K.C., Guneralp, B., & Hutyra, L.R. (2012). Global Forecasts of Urban Expansion to 2030 and Direct Impacts on Biodiversity and Carbon Pools. *Proc Natl Acad Sci U S A, 109*, 16083-16088

Seto, K.C., & Ramankutty, N. (2016). Hidden linkages between urbanization and food systems. *Science, 352*, 943-945

Seto, K.C., & Shepherd, J.M. (2009). Global Urban Land-Use Trends and Climate Impacts. *Current Opinion in Environmental Sustainability, 1*, 89-95

Sexton, J.O., Noojipady, P., Anand, A., Song, X.-P., McMahon, S., Huang, C., Feng, M., Channan, S., & Townshend, J.R. (2015). A Model for the Propagation of Uncertainty from Continuous Estimates of Tree Cover to Categorical Forest Cover and Change. *Remote Sensing of Environment, 156*, 418-425

Sexton, J.O., Song, X.-P., Feng, M., Noojipady, P., Anand, A., Huang, C., Kim, D.-H., Collins, K.M., Channan, S., DiMiceli, C., & Townshend, J.R. (2013a). Global, 30-m resolution continuous fields of tree cover: Landsat-based rescaling of MODIS vegetation continuous fields with lidar-based estimates of error. *International Journal of Digital Earth, 6*, 427-448

Sexton, J.O., Song, X.-P., Huang, C., Channan, S., Baker, M.E., & Townshend, J.R. (2013b). Urban growth of the Washington, D.C.-Baltimore, MD metropolitan region from 1984 to 2010 by annual, Landsat-based estimates of impervious cover. *Remote Sensing of Environment, 129*, 42-53

Shaban, M.A., & Dikshit, O. (2001). Improvement of Classification in Urban Areas by the Use of Textural Features: The Case Study of Lucknow City, Uttar Pradesh. *International Journal of Remote Sensing, 22*, 565-593

Sirmacek, B., Taubenbock, H., Reinartz, P., & Ehlers, M. (2012). Performance Evaluation for 3-D City Model Generation of Six Different DSMs From Air- and Spaceborne Sensors. *IEEE Journal of Selected Topics in Applied Earth Observations and Remote Sensing, 5*, 59-70

Small, C. (2003). High spatial resolution spectral mixture analysis of urban reflectance. *Remote Sensing of Environment, 88*, 170-186

Small, C. (2004). Global Population Distribution and Urban Land Use in Geophysical Parameter Space. *Earth Interactions, 8*

Small, C., & Sohn, R. (2015). Correlation Scales of Digital Elevation Models in Developed Coastal Environments. *Remote Sensing of Environment, 159*, 80-85

Small, C., & Sousa, D. (2016). Humans on Earth: Global extents of anthropogenic land cover from remote sensing. *Anthropocene, 14*, 1-33

Song, X.-P., Sexton, J.O., Huang, C., Channan, S., & Townshend, J.R. (2016). Characterizing the magnitude, timing and duration of urban growth from time series of Landsat-based estimates of impervious cover. *Remote Sensing of Environment, 175*, 1-13

Souch, C., & Grimmond, S. (2006). Applied climatology: urban climate. *Progress in Physical Geography, 30*, 270-279

Stehman, S.V., & Czaplewski, R.L. (1998). Design and analysis for thematic map accuracy assessment: fundamental principles. *Remote Sensing of Environment, 64*, 331-344

Stren, R. (2009). Globalisation and urban Issues in the Non-Western World. *Theories of Urban Politics*, 153-168

Swerts, E., Pumain, D., & Denis, E. (2014). The future of India's urbanization. *Futures, 56*, 43-52

Tachikawa, T., Kaku, M., Iwasaki, A., Gesch, D.B., Oimoen, M.J., Zhang, Z., Danielson, J.J., Krieger, T., Curtis, B., Haase, J., Abrams, M., & Carabajal, C. (2011). ASTER Global Digital Elevation Model Version 2 - summary of validation results. In (p. 27)

Tadono, T., Nagai, H., Ishida, H., Oda, F., Naito, S., Minakawa, K., & Iwamoto, H. (2016). Generation of the 30 M-Mesh Global Digital Surface Model by Alos Prism. *ISPRS - International Archives of the Photogrammetry, Remote Sensing and Spatial Information Sciences, 41B4*, 157-162

Tatem, A.J., & Hay, S.I. (2004). Measuring Urbanization Pattern and Extent for Malaria Research: A Review of Remote Sensing Approaches. *J Urban Health, 81*, 363-376

Tessler, Z.D., Vorosmarty, C.J., Grossberg, M., Gladkova, I., Aizenman, H., Syvitski, J.P.M., & Foufoula-Georgiou, E. (2015). Profiling risk and sustainability in coastal deltas of the world. *Science, 349*, 638-643

Thiele, A., Hinz, S., & Cadario, E. (2010). Combining Gis and Insar Data for 3d Building Reconstruction. *2010 IEEE International Geoscience and Remote Sensing Symposium*, 2418-2421

Tian, H.Q., Banger, K., Bo, T., & Dadhwal, V.K. (2014). History of land use in India during 1880-2010: Large-scale land transformations reconstructed from satellite data and historical archives. *Global and Planetary Change, 121*, 78-88

Tilton, J.C. (2007). Parallel Implementation of the Recursive Approximation of an Unsupervised Hierarchical Segmentation Algorithm. In C.-I. Chang, & A.J. Plaza

(Eds.), *High Performance Computing in Remote Sensing*. New York: Chapman and Hall/CRC Press

Tilton, J.C., Brown de Colstoun, E., Wolfe, R.E., Tan, C., & Huang, C. (2012a). Generating Ground Reference Data for a Global Impervious Surface Survey. In, *Geoscience and Remote Sensing Symposium (Igarss), 2012 Ieee International* (pp. 5993-5996)

Tilton, J.C., Tarabalka, Y., Montesano, P.M., & Gofman, E. (2012b). Best Merge Region-Growing Segmentation with Integrated Nonadjacent Region Object Aggregation. *IEEE Transactions on Geoscience and Remote Sensing, 50*, 4454-4467

Townshend, J.R., Masek, J.G., Huang, C., Vermote, E.F., Gao, F., Channan, S., Sexton, J.O., Feng, M., Narasimhan, R., Kim, D., Song, K., Song, D., Song, X.-P., Noojipady, P., Tan, B., Hansen, M.C., Li, M., & Wolfe, R.E. (2012). Global characterization and monitoring of forest cover using Landsat data: opportunities and challenges. *International Journal of Digital Earth, 5*, 373-397

Tucker, C.J., Grant, D.M., & Dykstra, J.D. (2004). NASA's Global Orthorectified Landsat Data Set. *Photogrammetric Engineering & Remote Sensing, 70*, 313-322

U.S. Energy Infromation Administration (2016). Commercial Buildings Energy Consumption Survey (CBECS). *Available online at* https://www.eia.gov/consumption/commercial *(accessed on 20-09-2017).*

UK Environment Agency (2016). Environment Agency LIDAR data Technical Note

Unger, A., & Riley, L.W. (2007). Slum Health: From Understanding to Action. *PLOS Medicine, 4*, e295

United Nations (2011). Urban Planning and Governance. In, *Population Distribution, Urbanization, Internal Migration and Development: An International Perspective*: United Nations, Department of Economic and Social Affairs, Population Division

United Nations (2015). Urban and Rural Population Growth and World Urbanization Prospects. In, *World Urbanization Prospects: The 2014 Revision (St/Esa/Ser.A/366)*: United Nations, Department of Economic and Social Affairs, Population Division

Valuation Office Agency (2012). Business Floorspace (Experimental Statistics). *Available online at* https://www.gov.uk/government/statistics/business-floorspace-experimental-statistics *(accessed on 20-09-2017).*

Van Zyl, J.J. (2001). The Shuttle Radar Topography Mission (SRTM): a breakthrough in remote sensing of topography. *Acta Astronautica, 48*, 559-565

Walton, J.T. (2008). Subpixel Urban Land Cover Estimation: Comparing Cubist, Random Forests, and Support Vector Regression. *Photogrammetric Engineering and Remote Sensing, 74*, 1213-1222

Wang, H., He, Q., Liu, X., Zhuang, Y., & Hong, S. (2012). Global Urbanization Research from 1991 to 2009: A Systematic Research Review. *Landscape and Urban Planning, 104*, 299-309

Wang, P., Huang, C., Brown de Colstoun, E.C., Tilton, J.C., & Tan, B. (2017). Human Built-up And Settlement Extent (HBASE) Dataset From Landsat. In. Palisades, NY: NASA Socioeconomic Data and Applications Center (SEDAC)

Wegner, J.D., Ziehn, J.R., & Soergel, U. (2014). Combining High-Resolution Optical and Insar Features for Height Estimation of Buildings with Flat Roofs. *IEEE Transactions on Geoscience and Remote Sensing, 52*, 5840-5854

Weng, Q. (2012). Remote Sensing of Impervious Surfaces in the Urban Areas: Requirements, Methods, and Trends. *Remote Sensing of Environment, 117*, 34-49

Weng, Q., Hu, X., & Lu, D. (2008). Extracting Impervious Surfaces from Medium Spatial Resolution Multispectral and Hyperspectral Imagery: A Comparison. *International Journal of Remote Sensing, 29*, 3209-3232

Wentz, E., Anderson, S., Fragkias, M., Netzband, M., Mesev, V., Myint, S., Quattrochi, D., Rahman, A., & Seto, K. (2014). Supporting Global Environmental Change Research: A Review of Trends and Knowledge Gaps in Urban Remote Sensing. *Remote Sensing, 6*, 3879-3905

White, J.C., Wulder, M.A., Hobart, G.W., Luther, J.E., Hermosilla, T., Griffiths, P., Coops, N.C., Hall, R.J., Hostert, P., Dyk, A., & Guindon, L. (2014). Pixel-Based Image Compositing for Large-Area Dense Time Series Applications and Science. *Canadian Journal of Remote Sensing, 40*, 192-212

Wigginton, N.S., Fahrenkamp-Uppenbrink, J., Wible, B., & Malakoff, D. (2016). Cities are the Future. *Science, 352*, 904-905

Williams, K., Burton, E., & Jenks, M. (1996). Achieving the compact city through intensification: an acceptable option. *The compact city: A sustainable urban form*, 83-96

Wu, C.S., & Yuan, F. (2007). Seasonal Sensitivity Analysis of Impervious Surface Estimation with Satellite Imagery. *Photogrammetric Engineering and Remote Sensing, 73*, 1393-1401

Wulder, M.A., Masek, J.G., Cohen, W.B., Loveland, T.R., & Woodcock, C.E. (2012). Opening the archive: How free data has enabled the science and monitoring promise of Landsat. *Remote Sensing of Environment, 122*, 2-10

Wurm, M., d'Angelo, P., Reinartz, P., & Taubenbock, H. (2014). Investigating the Applicability of Cartosat-1 DEMs and Topographic Maps to Localize Large-Area Urban Mass Concentrations. *IEEE Journal of Selected Topics in Applied Earth Observations and Remote Sensing, 7*, 4138-4152

Xian, G., & Homer, C. (2010). Updating the 2001 National Land Cover Database Impervious Surface Products to 2006 using Landsat Imagery Change Detection Methods. *Remote Sensing of Environment, 114*, 1676-1686

Xian, G., Homer, C., Demitz, J., Fry, J., Hossain, N., & Wickham, J. (2011). Change of Impervious Surface Area between 2001 and 2006 in the Conterminous United States. *Photogrammetric Engineering and Remote Sensing, 77*, 758-762

Xu, M., He, C., Liu, Z., & Dou, Y. (2016). How Did Urban Land Expand in China between 1992 and 2015? A Multi-Scale Landscape Analysis. *Plos One, 11*, e0154839

Yang, L.M., Huang, C., Homer, C.G., Wylie, B.K., & Coan, M.J. (2003). An Approach for Mapping Large-Area Impervious Surfaces: Synergistic Use of Landsat-7 Etm+ and High Spatial Resolution Imagery. *Canadian Journal of Remote Sensing, 29*, 230-240

Yin, H., Pflugmacher, D., Kennedy, R.E., Sulla-Menashe, D., & Hostert, P. (2014). Mapping Annual Land Use and Land Cover Changes Using MODIS Time Series. *IEEE Journal of Selected Topics in Applied Earth Observations and Remote Sensing, 7*, 3421-3427

Yuan, F., Wu, C.S., & Bauer, M.E. (2008). Comparison of Spectral Analysis Techniques for Impervious Surface Estimation Using Landsat Imagery. *Photogrammetric Engineering and Remote Sensing, 74*, 1045-1055

Zeug, G., & Eckert, S. (2010). Population Growth and Its Expression in Spatial Built-up Patterns: The Sana'a, Yemen Case Study. *Remote Sensing, 2*, 1014-1034

Zhang, K.Q., Chen, S.C., Whitman, D., Shyu, M.L., Yan, J.H., & Zhang, C.C. (2003). A progressive morphological filter for removing nonground measurements from airborne LIDAR data. *IEEE Transactions on Geoscience and Remote Sensing, 41*, 872-882

Zheng, Y.F., & Weng, Q.H. (2015). Model-Driven Reconstruction of 3-D Buildings Using LiDAR Data. *IEEE Geoscience and Remote Sensing Letters, 12*, 1541-1545

Zhou, Y., Smith, S.J., Zhao, K., Imhoff, M., Thomson, A., Bond-Lamberty, B., Asrar, G.R., Zhang, X., He, C., & Elvidge, C.D. (2015). A Global Map of Urban Extent from Nightlights. *Environmental Research Letters, 10*, 054011

Zhu, Z., Woodcock, C.E., Holden, C., & Yang, Z. (2015). Generating synthetic Landsat images based on all available Landsat data: Predicting Landsat surface reflectance at any given time. *Remote Sensing of Environment, 162*, 67-83